Mechanical properties of Metal Based Flexible Transparent Conductive Electrode: From Fracture Mechanics perspective

by

Sangeon Lee

A dissertation submitted in partial fulfillment
of the requirements for the degree of
Doctor of Philosophy
(Mechanical Engineering)
in The University of Michigan
2019

Doctoral Committee:

Professor L. Jay Guo, Chair
Assistant Professor Yue Fan
Professor Jinsang Kim
Professor Wei Lu

Sangeon Lee

sangeon@umich.edu

ORCID iD: 0000-0002-7076-9638

© Sangeon Lee 2019

All Rights Reserved

DEDICATION

To my wife, Christine

ACKNOWLEDGEMENTS

It has been a great pleasure to tirelessly work with people at the University of Michigan. I'm more than happy to have reached to this point and be given this opportunity to express my gratitude to those who made this milestone possible.

First and foremost, I would like to show appreciation to my advisor, Professor L. Jay Guo. I cannot thank him enough for his guidance and encouragement, which have been wonderful nutrients for my research and intellectual growth. His insightful questions have trained me to be diligent because they deserved good answers.

Besides my advisor, I would like to thank my committee members, Professor Jinsang Kim, Professor Wei Lu, and Professor Yue Fan for their invaluable suggestions and discussion, support, and time throughout this study.

Special thanks goes to six persons: Dr. Taehee Jang, Dr. Hyunsoo Kim, Dr. Jaeyong Lee, Dr. Jinhwan Lee, Dr. Taehwa Lee and Professor Yiquan Li. Not only did they help me shape my research, but also motivated me with their knowledge and wisdom.

I am also grateful for my past and present nanogroup members for their help and kindness during my studies at the university. Especially, I would like to thank my co-workers, Chengang, Yongbum and Sunghyun.

Last but not least, I would like to express my deepest gratitude to my wife, parents, brother, parents-in-law, and all of my family and friends. This dissertation would not have been possible without their warm love, continued patience, and endless support.

TABLE OF CONTENTS

DEDICATION	ii
ACKNOWLEDGEMENTS	iii
LIST OF FIGURES	vii
LIST OF TABLES	xv
ABSTRACT	xvi

CHAPTER

I. Introduction	1
Background and Motivation	1
Goal and Thesis Outline	4
II. Fracture Behavior of DMD Multilayer	6
Introduction	6
Various Bending Test Setup Methods	9
Our Setup	12
DMD Electrode Fabrication	13
Bending Performance Evaluation of a DMD Structure	14
Crack Geometry Inspection: Crack Varies Depending on the Bending Radius	18
Griffith's Strain Energy Release Rate	19
Energy Principles	21

Atomic Bonds and Surface Energy 22
Strain Energy Release Rate 23
Griffith's Failure Criterion 24
Nonlinear Fracture Mechanic Analysis: J-integral 25
Stress Analysis in the Vicinity of the Crack Tip 26
Bio-inspired Toughening Mechanisms in a Hierarchical Structure 30
Crack Deflection in DMD Multilayer When Subjected to Bending Operation 32
The Linear Elastic Crack Deflection Mechanics Solution of He and Hutchinson 33
Derivation for Energy Release Rate 34
Identify Young's Modulus of Each Layer 40
Crack Propagation Simulation by Cohesive Zone Model (CZM) 42
Stress Distributions Throughout the Cross Section During Bending 47
Interfacial Failure between DMD and PET Structures 49
Conclusion 51

III. Fatigue of Flexible Electrode 57
Introduction 57
Bending Test Set Up and Strain Rate Calculation 58
Comparison of Cyclic Performance Results 63
Effects of Strain Rate 67
Ductile To Brittle Transitions 71
Crack Deflection and Penetration Competition Due to the Strain Rate 73
Conclusion 77

IV. Multiple Neutral Plane to Mitigate Bending Stress 79
Introduction 79
Sample Fabrication for Multiple Neutral Plane 81
Bending Tests 84
FEA Simulations 86
Analytical Modelling Accounting for Multiple Neutral Axes 88
Conclusion 92

V. Concluding Remarks and Suggestions for Future Work 94

Concluding Remarks 94

Suggestions for Future Work 95

Ductile Brittle Hybrid Structure 95

Atomistic Simulation 96

REFERENCES 97

LIST OF FIGURES

Figure.2.1. Various forms of flexible electronics technology. There are various forms of flexible electronics technology, from rigid to foldable form. The bending radius have been reduced for future foldable electronics. 7

Figure.2.2. Key challenges for flexible electronic applications: It should have high transmittance, low sheet resistance, robust and flexible for future flexible electronics. 9

Figure.2.3. Illustration of the schematic diagram and corresponding folding simulation results of the bending system, respectively. (a) free-arc bending system (b) Guiding plate enhanced bending system (c) Folding system (d) Bending radius is carefully measured to the inside curvature. 12

Figure.2.4. Strain analysis of our bending tester by finite element analysis: It demonstrates stress is localized on a bending region. It demonstrates stress variance depending on the position and sample deformation. 13

Figure.2.5. Sequential images of our bending tester operation: From (a) flatten to (b) fold state. It is possible to control strain rate (0.01%/s to 1.5%/s) and travel distance (1mm to 20cm). 14

Figure.2.6. Stress distribution results between (a) free arc bending and (b) folding system. Stress level is higher in folding system compared to free arc system. (c) Bending test results of DMD films on PET. Electrical resistance of both samples measured in situ during bending. Folding system provide an accurate bending radius and severe bending stress. 14

Figure 2.7. Bending test results of ITO and DMD films on PET. (a) and (b) Electrical resistance of both samples measured in situ during bending. (c) and (d) SEM images of the same surface area taken at bending radius R=3mm. 17

Figure 2.8. (a) and (b) Simulation results of bent substrate. The strain is proportional to the sample thickness and inversely proportional to the bending radius. Apparently, bending induced localized strain and (c) Bending induces localized strain near the folded region, and crack will initiate mainly in this area. 18

Figure 2.9. Representative SEM snapshots of propagation of the initial crack. (a) As bending radius is getting smaller, small crack (500nm long) merged together and channeling crack was created. (b) Crack dimension was also increased depending on the bending strain. Blunt crack tip was detected due to the ductile layer. 21

Figure 2.10. (a) In order to break a bond, applying force should be higher than cohesive force between each atom. (b) Schematic illustration of intermolecular potential energy diagram. 24

Figure 2.11. Schematic illustration of (a) atomic bond energy and (b) strain energy. Griffith proposed conditions for crack propagation: the amount of strain energy released must be greater than or equal to the surface energy of the crack faces created. 26

Figure 2.12. This change in energy (dU) should be negative with an increase in crack length (or at worst equal to zero). i.e. $(dU/da) \leq 0$. And at a* the slope of U is zero $[(dU/da)_{a^*} = 0]$. This is a point of unstable equilibrium 27

Figure 2.13. J-integral around a notch in two dimensions. We can use the following variables: S represents a curve linking the lower and upper crack surfaces. ds means an element of arc on this curve. T is traction vector on this curve defined in relation to an outward normal unit vector, i.e. $T = n \times \sigma$. u is the corresponding displacement vector. 29

Figure 2.14. Crack dimension difference between ITO and DMD sample, simulation

results of crack tip stress analysis of both electrodes. (a) Finite element analysis of stress contour in the vicinity of crack tip for both sample (b) SEM image of a cracked ITO and DMD sample. (C) Stress as a function of distance from the crack tip. A nonlinear zone from the crack tip is approximately 5.6 nm. 31

Figure 2.15. It illustrates bio-inspired hierarchical structure of human teeth and nacre layers from nature. 34

Figure 2.16. It shows SEM (cross-sectional fractured surfaces) images of crack propagation at bending radius (R=5mm). (a) The path of the cracks meanders alternately along with CuAg interfaces, and then cutting through bottom ITO layer (b) In ITO sample, there is only penetrated crack when subjected to bending. 35

Figure 2.17. He and Hutchinson provide a quantitative analysis tool to predict whether an impinging crack will penetrate through whole layers or deflect along with a linear elastic bi-material interface. 37

Figure 2.18. Assuming λ as a function of α for $\beta = 0$. 38

Figure 2.19. The linear-elastic crack-deflection mechanics solution of He and Hutchinson for a crack normally impinging an interface between two elastically dissimilar materials. (A) The curve marks the boundary between systems in which cracks are likely to penetrate the interface (above the curve, red square dot) (B) or deflect along the CuAg interface (below the curve, blue square dot). 43

Figure 2.20. Schematic illustration of elastic modulus calculation for multilayer structure. Voigt proposed the effective elastic modulus of the multilayer. 44

Figure 2.21. Based on DMA tensile test, it provides elastic modulus of each material. After extracting stress strain curve of each sample, by using Voigt's approach, we can calculate E_{DMD}=107.27GPa and E_{CuAg}=82.18GPa, respectively. 45

Figure 2.22. Comparison of simulation results of crack propagation direction of DMD and ITO layer at bending radius R=4mm. Yellow arrow indicate crack propagation direction. 49

Figure 2.23. Simulation results of crack propagation direction of DMD layer. 49

Figure 2.24. FEA results compare between the multilayer structure with specific metallic layers, and pure ITO structures when subjected to bending. (a) Pure ITO structure under bending radius R=6mm, (b) Pure ITO structure under bending radius, R=5mm. Strain level was increased due to the conventional beam bending theory (0.53% to 1%). (c) However, if we insert metal layer in between, strain level is decreased in comparison to pure ITO case. At bending radius, R=5mm, strain level of outer layer is 0.82%. 51

Figure 2.25. Debonding failure occurs between PET and ITO interlayer. (a) FEA simulation results of interfacial failure between ITO and PET layer. When crack impinging on a bi-material interface, and it will penetrate through the interface as well as the bottom ITO layer or deflect along with metal layer. Due to the low adhesion energy 0.1 $J \cdot m^{-2}$ between ITO and PET layer, then delamination failure will be happened along with ITO/PET interface under severe bending stress. 54

Figure 3.1. (a) Schematic illustration of multilayer. Linear elastic deformation is governed by Euler and Bernoulli equation, which states inner layer has compressive stress whereas outer layer has tensile stress when subjected to bending. In the middle layer, there is a neutral plane. (b) Bending radius is carefully measured to the inside curvature. 58

Figure 3.2. It shows the dynamic outer bending fatigue test results of the optimized DMD multilayer with increasing bending cycles at a fixed outer bending radius of 5 mm. (a) Comparison of flexible electrode cyclic performance results (b) DMD multilayered structure resistance versus repeated oscillating bending events (at R=5 mm radius). Inset: a zoomed-in fragment of the main curve showing perfectly repeatable and stable sheet resistance oscillations, DMD exhibits very stable resistance value even after over

ten thousand bending cycle number. (c, d) Fatigue comparison results between tensile and compressive at bending radius 4mm. Compression shows better cyclic performance compared to that of tensile stress case. This is because the effective cross section increases in compression, alternatively it decreases in tension stress. 61

Figure 3.3. Schematic illustration of failure mechanisms of the DMD film subjected to (a) outward bending and (b) inward bending. (a) Cracks induced by tensile stress causing rupture of the DMD film. Figure (b) illustrates the formation of buckles due to mitigation of in-plane compressive stress when subjected to inward bending 62

Figure 3.4. Based on our bending test results, (a) metal grid and (b) AgNW sample failed rapidly comparing to DMD sample. These promising electrode exhibits brittle fracture due to the localized necking, and leading to the abrupt increase of electrical resistance in flexible electrodes. 66

Figure 3.5. Comparison between (a) elastic (higher than R = 5mm) and (b) plastic deformation (less than R= 4mm). In elastic deformation, resistance is fully dependent on strain, however, in plastic deformation, resistance varies each other despite of applying same strain. 68

Figure 3.6. Several electrode's electrical performance parameters can be plotted against mechanical strain and strain rate. Interestingly, all electrodes exhibit hysteresis and begin to diverge after elastic deformation. The higher strain rate provide stiff increase of resistance. These materials are sensitive to the strain rate. 69

Figure 3.7. In plastic region, DMD electrode fails earlier in case of higher strain rate. 70

Figure 3.8. Dislocation is located on the bottom of its potential energy valley until thermal fluctuation enables it to climb over the activation barrier to glide to the next valley. 71

Figure 3.9. Depending on the strain rate, elastic modulus is changed accordingly. At the

high strain rate (1.0%/s), Young's modulus shows 120.14 GPa, whereas at the low strain rate (0.01%/s), it shows moderate elastic modulus 82.28 GPa. 73

Figure 3.10. SEM images of (a) deflected crack at low strain rate (0.01%/s) (b) penetrated crack at high strain rate (1%/s). 74

Figure 3.11. Mechanics solution by He and Hutchinson's approach. The curve marks the boundary between systems in which cracks arelikely to penetrate the interface (above the curve, red square dot, at high speed) or deflect along the CuAg interface (below the curve, blue square dot) at low strain rate. 75

Figure 3.12. Statistical analysis of crack deflection and penetration in DMD multilayer structure. 76

Figure 3.13. Top view of SEM image of DMD sample after 100 cycles at R = 4mm. It can be clearly seen that outer bending for 100 cycles in plastic region lead to the formation of cracks normal to the bending direction. In low strain rate, deflected crack was still observed, while in high strain rate, penetrated crack was detected. 76

Figure 3.14. Uneven surface was created due to the fatigue loading. 77

Figure 4.1. Schematic illustration of multiple neutral plane concepts. The middle layer is much softer than the other layers, both PET layers will bend independently. The soft adhesive largely deformed transferring the shear stress. Maximum bending strain of outer layer will be reduced with increased compliance of the structure compared to the structure with the hard adhesive. So if we increase the shear strain, it benefits the transfer of strain energy to the middle layer such that the strains in the outer layers diminish. 80

Figure. 4.2. Sample preparation process. In order to solidify each soft material, we used both UV and thermal curing process. In addition, for better adhesion, oxygen plasma treatment

was applied to bare PET substrate. According to the contact angle measurement, surface wettability was enhanced and become hydrophilic surface after oxygen plasma treatment. 81

Figure. 4.3. It shows the elastic modulus of middle layer with different mechanical property. Various mixing ratios of the base polymer and curing agent was evaluated. There are two different types of middle layer on the table. (a) For hard middle layer: NOA73 (1.8 GPa), PUA (1.5 GPa), PVA (1.2 GPa), (b) For soft middle layer: PDMS 6:1 (0.8 MPa), PDMS 10:1 (0.6 MPa), PDMS 30:1 (0.4 MPa), and elastic PVA (0.1 MPa). 83

Figure. 4.4. Electrical resistance results of multiple samples during bending (a) Based on conventional beam theory, DMD on 13μm PET sample shows superior flexibility compared to DMD on 50μm PET sample. (b) Depending on the middle layer mechanical property, it exhibits different $\Delta R/R_0$ value. Even though these multilayer structures have identically same thick structures, they provide significantly different electromechanical results. (c) Cyclic bending results of DMD multilayer combined with elastic PVA middle layer. 85

Figure 4.5. It presents the FEA results of bending two different multilayer structures with specific adhesive layers when multiple neutral planes appear in the structure. Even though these structures have identically same thick structures with PET 13μm/adhesive 24μm/ PET 13μm, it possesses significantly different strain level: one was a hard adhesive (E_{NOA73}=1.8GPa, (a) and the other was a soft adhesive ($E_{elastic\ PVA}$=0.1MPa, (b). 87

Figure 4.6. Notations used in the analytical modelling. Top and bottom layer has same elastic modulus and middle layer possesses very compliant layer in comparison to PET layer. The outer layer bending stress and middle layer shear stress should be equivalent. In addition, continuity equation at each layer interfaces is still valid. 89

Figure 4.7. Through-stack strain distribution in the flexible conductor with a PET layer thickness of 50 μm bent to a radius of 1 mm. The blue line represents results calculated using the conventional theory, the red line is derived by using the multiple neutral-axes theory. Adding a soft adhesive create additional neutral plane, and minimizes their strains

during bending. The neutral mechanical plane is split into multiple ones. (a) Figure demonstrates when DMD structure is subjected to tensile stress (Outward bending) and (b) is under compressive stress (Inward bending). 92

Figure 4.8. Maximize decoupling of each layer: Increase shear stress is key component to relieve outer layer bending stress. 93

LIST OF TABLES

Table 2.1. Summary of different criteria found in literature 22

Table 2.2. Summary of crack dimension analysis 33

Table 2.3. The variables *λ, c, h,* d_R, d_I G_p, G_d (singly deflected crack) as a function of *α* 41

Table 4.1. Notations used in the mechanical modelling for multiple neutral plane 89

ABSTRACT

With increasing interests for transparent conductive electrode for flexible electronic devices, many researchers have developed flexible electrodes from curved devices to wearable and foldable devices. But they are faced with new challenges because these devices not only require high optical transmittance and low sheet resistance value, but also must be able to change its shape to flexible, bendable, and even stretchable form. Studies in the past focused heavily on the process and material development to improve functionality and flexibility without a thorough mechanical investigation and a deep understanding failure mechanisms.

Dielectric/Metal/Dielectric (DMD) layer consists of few tens of nanometer thick structure, and despite its outstanding optoelectronic performance, research on the mechanical and electrical relationship has not yet been investigated thoroughly. One of the reasons is that studies on nanoscale mechanics and flexible electronics have been conducted independently by researchers in different fields. Moreover, fracture mechanics confront new challenges at the nanoscale. It is known that the fracture mechanics of nanoscale materials are significantly different from those on the macroscopic scale. As the structural dimensions of materials are scaled down to nanoscale, only an extremely limited number of atoms exist in the vicinity of the crack tip, which challenges the conventional fracture mechanics theory. It brings up fundamental questions about what scale fracture mechanics effectively govern and what the basic principles and theories are in a nanometer scale. Due to experimental difficulties at the nanometer scale, very few attempts have tried to solve this important issue.

In this study, we investigate the fracture characteristics of multilayer DMD structure and its unique cracking behavior. Abnormal crack propagation and toughening of multilayer DMD structures are analyzed and its underlying mechanism are explained. Various experiments and theoretical analyses are carried out to uncover the details of multilayered hierarchical structures and their underlying crack deflections.

We analyze the fracture behavior of thin film structures during bending process and proposed a theoretical framework to identify the underlying principles of robustness for DMD multilayered structures. Bio-inspired ductile brittle combination strategy and experiments on crack deflection behavior of DMD layers are carried out to find the fracture toughness in thin materials. We also investigate fatigue failure for various conductive materials through cyclic experiments. Various bending speed experiments are performed to study the effect of strain rates, and we present that they control mobility of atoms, which changes its mechanical and electrical property. Most notably, we introduce a unique crack deflection propagating phenomenon where a crack can deflect along with the metallic layer and create a step-like fracture. Lastly, we generate multiple neutral plane and insert stretchable layer in the middle to minimize the strain exerted on the electrode during bending and also to achieve better flexibility in DMD samples. We provide a concise and accurate analytical model for this multilayer structure with dissimilar elastic properties and make it conclusive with numerical simulation and experimental results.

CHAPTER I

Introduction

Background and Motivation

With increasing attention and interests for transparent conductive electrode for flexible electronic devices, many researchers have developed flexible electrodes curved devices to wearable and foldable devices [1,2]. Samsung also plans to release new foldable smartphones in the near future, because it offers smarter, flexible, and bendable designs to optoelectronic devices, such as flexible displays and touch sensor [3,4]. However, transparent conducting films are facing new challenges, because they not only require high optical transmittance and low sheet resistance value, but also must be able to change their shape to flexible, bendable, and even stretchable form [5-7]. Flexibility is difficult to be realized in conventional electronic components, which are generally fabricated on a rigid substrate. According to the conventional Euler–Bernoulli beam theory, it is possible to reduce the mechanical stress and strain by making substrates thin [9].

Traditionally, transparent electrodes are made of deposited ITO thin films, which exhibit excellent electrical conductivity and high optical transmittance (10−20 Ω /sq at a transmittance of 90%). However, ITO films undergo the degradation process by cracking or channeling defects by bending stress, resulting in a sudden increase in their electrical resistivity that leads to

catastrophic failure. This is because ITO is brittle and largely limits its application in flexible devices at bending radius less than 10mm. This degradation behavior of electrodes below the threshold bending radius makes future flexible electronic applications more difficult to develop. Therefore, non-ITO transparent conductive electrode materials are highly desired [11-13].

Current research trend focuses on reducing bending radius in future flexible transparent conductive electrodes, however, we are faced with challenges due to electrical and mechanical degradation of flexible electrodes under strain-dependent deformations and crack initiation and propagation of electrodes. In addition, there needs to be more studies on the reliability of these flexible electronics for commercialization. For instance, with the development of modern technologies, such as the IoT applications, the failure of single electronic component may cause a substantial failure of a whole system since these devices are closely interconnected. Moreover, one of the characteristics of flexible electronics is their intimacy to user's body. Epidermal and wearable electronics are designed to contact the human skin directly. And failure of flexible electronics can cause significant safety problems as well as operational malfunctions. In order to design a highly reliable flexible device, comprehensive studies must be carried out to understand the effects of various mechanical deformations. Among them, fatigue failure, which occurs when small deformations are repeatedly applied below the fracture strain, is the biggest issue.

Until now, conventional electronics have been designed and produced mostly with the assumption of mechanically static operations, e.g., no repeated movements or impacts. Studies in the past focused mainly on the process and material development to improve their functionality and flexibility. Rudimentary and typical bending tests were performed without a thorough mechanical investigation and a good understanding of failure mechanisms.

A huge amount of effort was devoted to developing new electronic materials in order to achieve more flexibility in a long-term cycle, one of which was dielectric/thin-metal/dielectric (DMD) [15,16]. DMD is thin multilayer structure and can be considered the ultimate thin material. Its structure has been studied extensively to achieve highly transparent and conductive electrodes. It is certainly a fascinating non-ITO transparent conductive electrode material. The thin metal layer in the middle provides the electrical conductance while the two dielectric layers improve the overall transparency of the entire structure. Furthermore, DMD multilayer electrodes show excellent mechanical flexibility in comparison to ITO electrodes. The good ductility of metal layers enable their application in flexible optoelectronic devices [17-19].

However, a deep understanding of failure mechanisms in nanoscale structure is crucial in developing stable flexible electronics. DMD consists of few tens of nanometer thick structure, and despite its outstanding optoelectronic performance, research on the mechanical and electrical relationships have not yet been thoroughly reviewed. One of the reasons for this is because the studies on nanoscale mechanics and flexible electronics have been conducted independently by researchers in different fields. But moreover, fracture mechanics confront new challenges at the nanoscale [20,21]. It is known that the fracture mechanics of nanoscale materials are significantly different from those on the macroscopic scale. As the structural dimensions of materials are scaled down to nanoscale, only an extremely limited number of atoms exist in the vicinity of the crack tip, which challenges the conventional fracture mechanics theory [24,25]. Continuum theory surmises the presence of sufficiently large number of atoms when considering the surrounding crack-tip area as continuum media [23]. This discrepancy brings up fundamental questions to what scale fracture mechanics effectively govern and what the basic principle and theory is in a nanometer scale. Due to experimental difficulties at the nanometer scale, very few

attempts have been tried to solve this problem. Interpretations from the perspective of continuum mechanics and finding its limits still remain a challenge and a work in progress [23,26].

In this study, we investigated the fracture characteristics of multilayer DMD structure and its unique cracking behavior. Abnormal crack propagation and toughening of multilayer DMD structure were analyzed and its underlying mechanism was explained. Various experiments and theoretical analyses were carried out to uncover the details of multilayered hierarchical structures and their underlying crack deflections.

Goal and Thesis Outline

This work aims to predict and analyze the mechanical failure of structural components of DMD structures to develop a highly flexible transparent conductive electrodes since the root cause of the electrode degradation and its failure mechanisms were not clear. Through our research, we discovered the fundamental fracture mechanisms of transparent conductive electrodes through extended fracture and fatigue tests, by controlling bending radius and strain rate, visual inspection, electromechanical characterization, fracture mechanics, and finite element analyses and theoretical analyses. Detailed frameworks, methodologies, and results are described in the following chapters. This thesis is organized as follows: Chapter 2 demonstrates the fracture behavior of thin film multilayered structures and proposes a theoretical method to evaluate robustness of transparent conductive electrodes. Chapter 3 analyzes fatigue behavior of thin film multilayered structures with various non-ITO transparent conductive electrode materials and demonstrates strain rate dependent effects in a DMD multilayered structure. We show how thin metallic layer can prevent electrode cracks and offer ways to enhance the fracture

resistance in future flexible electronics. Chapter 4 describes potential future direction by controlling the neutral plane to mitigate the bending stress, which will help make more robust and stable electrodes at small bending radii. Chapter 5 summarizes the findings and offers new perspectives.

CHAPTER II

Fracture Behavior of DMD Multilayer

Introduction

Flexible devices are of high interest due to potential expansion of the smart devices into various fields, such as energy harvesting, biological applications and consumer electronics [1-3]. These flexible transparent conductive electrodes are evaluated under various types of stress, including tensile, compression, twinning and bending [27].

We should clearly define "flexibility" before going into further analysis. Flexibility refers to the capability of bending without any breaking of atomic bonds in electrode. Stiffness is the extent to which a sample resists deformation in response to an applied load. The complementary terminology is flexibility: the more flexible an object is, the less stiff it is. The flexibility of a structure is of principal importance in many engineering applications, so the elastic modulus is often one of the primary properties considered when selecting a material. A high modulus of elasticity is sought when deflection is undesirable, while a low modulus of elasticity is required when flexibility is needed. In addition, physical dimension factors, e.g., thickness, length, and the moment of inertia can also affect the electrode's ability to resist bending. If the thickness of sample increases, the stiffness will increase exponentially. It is important to reduce the mechanical stress and strain by making substrates thin to improve flexibility. In our study,

because substrate is much thicker than electrode, substrate thickness heavily impacts the total strain under bending deformation.

The developers of flexible transparent conductive electrodes have used the threshold radius of curvature of transparent conductive electrodes as an electrical failure criterion [29]. This threshold radius of curvature, at which the electrical resistance is unable to go back to its initial value, have been reduced from 10mm for bendable displays to less than 5mm for rollable and foldable displays [28].

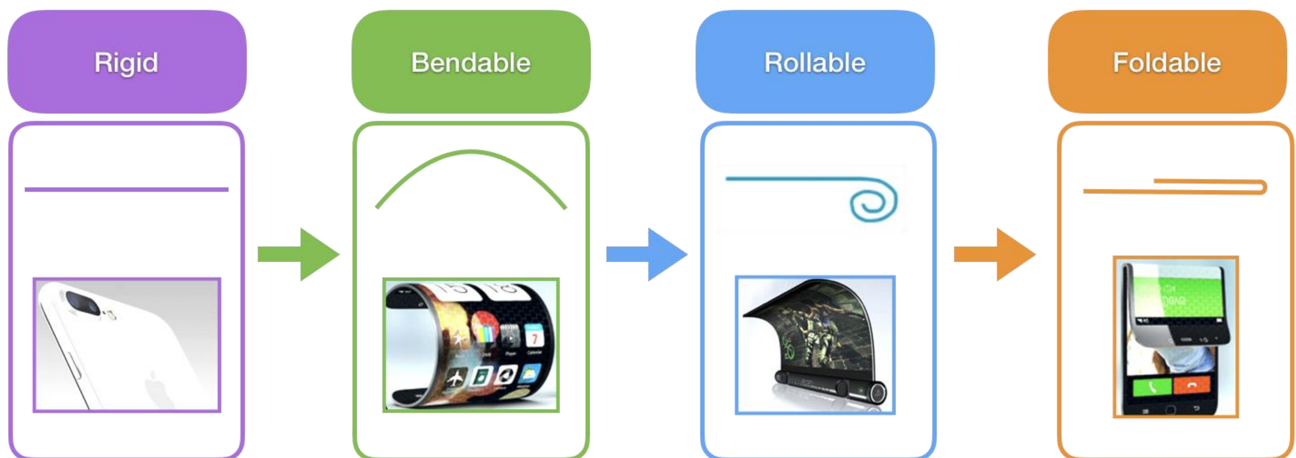

Figure.2.1. Various forms of flexible electronics technology. There are various forms of flexible electronics technology, from rigid to foldable form. The bending radius have been reduced for future foldable electronics.

A huge amount of effort has been devoted to develop new electronic materials with better bendability and flexibility to open a new era of flexible devices. Among these candidates is the use of dielectric–thin metal–dielectric (DMD) multilayers, an alternative to using simple ITO film for transparent conductors [17,19]. Since the first report by Fan *et al.* in 1974 [56], DMD multilayer structures have been studied extensively to achieve highly transparent and conductive

electrodes [57]. These structures are typically composed of a thin silver layer (10 nm) sandwiched between two dielectric layers (40 nm). When ideally designed, the high index of refraction contrast between Ag and the dielectric layers result in visible transparency greater than 90% can be achieved.

Furthermore, DMD multilayer electrodes show excellent mechanical flexibility in comparison to ITO electrodes mainly due to the excellent ductility of metal layers. It enables their application in flexible optoelectronic devices and helps with better flexibility. These advantages make the multiple layer electrodes potential non-ITO transparent conductive electrode materials. Thus far, sputter and thermal evaporation are the two major deposition methods for metal and dielectric layers in DMD electrodes.

DMD structure provides unique optoelectronic property because it exhibits higher transmittance and low sheet resistance. While these structures have been investigated in detail for improved conductivity electrodes for displays, their utility as mechanically robust transparent conductive electrode has not been thoroughly studied. The DMD films deposited on plastic substrates showed dramatically improved mechanical properties when subjected to bending, both as a function of radius of curvature as well as number of cycles to a fixed radius [19]. In this chapter, we demonstrate the improved performance of DMD over ITO in regards to conductivity and flexibility. We also show how the addition of the ductile silver layer provides improved robustness under mechanical strain. The combined techniques provide valuable correlated electrical and mechanical data needed to understand the failure mechanisms in flexible devices.

DMD layer on top of PET specimens was tested by bending test setup along with a scanning electron microscope (SEM) inspection. The elastic modulus and fracture toughness of

DMD specimens were determined by measuring stress-strain curves and through finite element analysis (FEA).

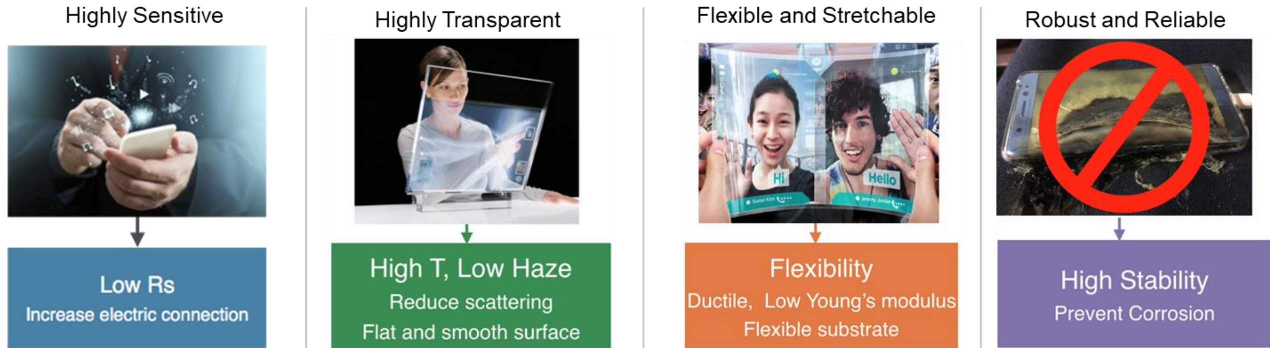

Figure.2.2. Key challenges for flexible electronic applications: It should have high transmittance, low sheet resistance, robust and flexible for future flexible electronics.

Various Bending Test Setup Methods

There are two different types of bending operations. First, there is fracture, which is a one-time static bending. When materials are subjected to a large strain, they fail by fracture. Another type is fatigue. Fatigue is weakening of a material caused by repeatedly applied loads. In this chapter, we will discuss fracture behavior of DMD electrodes.

Bending-mode tests are widely used in both the academic and industry fields to evaluate the strain tolerance of flexible electronics. When discussing the stability of transparent conductors, common but important themes include tracking the electro-mechanical degradation of brittle transparent conductors and developing more strain-resistance of non-ITO conductive materials. Bending operation is an extremely important deformation mode that must be studied in depth to develop flexible electronic devices that are also reliable. Both the characteristics of individual components and integrated systems must be considered, and electrical properties

should be measured during or after the bending operation of the sample through electrical connection at the grips.

To characterize the bending-mode strain tolerance of flexible electronics, several variables can be used to describe the deformation magnitude. The most common type is the radius of curvature, where the sample is bent to find out how the smaller bending radius corresponds to a larger deformation. Because substrate thickness strongly influences the strain during the bending process, many researchers perform geometry-based calculations to find the relationship between the bending radius and the actual strain that is imparted on electronic materials. With these calculations, the electrode's performance parameters can be plotted against mechanical strain, which helps with the assessment of the strain tolerance.

Many researchers and industries have been developing different bending test setups to evaluate the durability of flexible electronics, the measured results vary due to different designs [30, 31]. Figure 2.3 shows three representative methods that are widely used for testing flexible devices today: (a) rudimentary linear back and forth motion setup without a guiding plate, (b) the variable radius bending test with guiding plates, (c) the folding plate test. The linear back and forth motion test setup is most commonly used. Two grips hold each sides of the sample and linear back and forth motion is repeated to induce a bending deformation in the electrode. For this method, the grip used to hold the sample on each side is especially important. It should be designed to minimize any additional stress on the electrode near the grip so that the maximum stress will be focused at the bending point of the target sample. The electrical properties can be measured during or after the bending motion through electrical contacts at the grip. This setup is the simplest one of the three, but has some drawbacks. First of all, it will be difficult to induce severe bending deformation at extremely small bending radius. Secondly, the bending radius

differs depending on the viewpoint. Without guiding plate, it will be challenging to control an accurate bending radius. This method will not fully satisfy an accurate bending operation [30,36].

The second method is the variable radius bending test with guiding plates. The concept is very similar to that of the rudimentary back and forth setup, but the sample is subjected to bending between two guiding plates. These plates play an important role because they create a homogeneous bending shape into the target bending radius. They provide simple, yet fast and precise control of the various bending strains. However, there is a fluctuation issue. The stress level on the sample will fluctuate since the contact area between the plate and the sample will change according to the bending radius.

The third method is the folding plate test setup. This one is very similar to the future foldable phone operation concept. The electrical resistance can be measured in real time using conductive grips. The sample is in the center and it repeatedly folds and flattens. The electrical properties are measured before and after mechanical folding deformation. Bent section of the sample will have accurate bending radius unlike the second method.

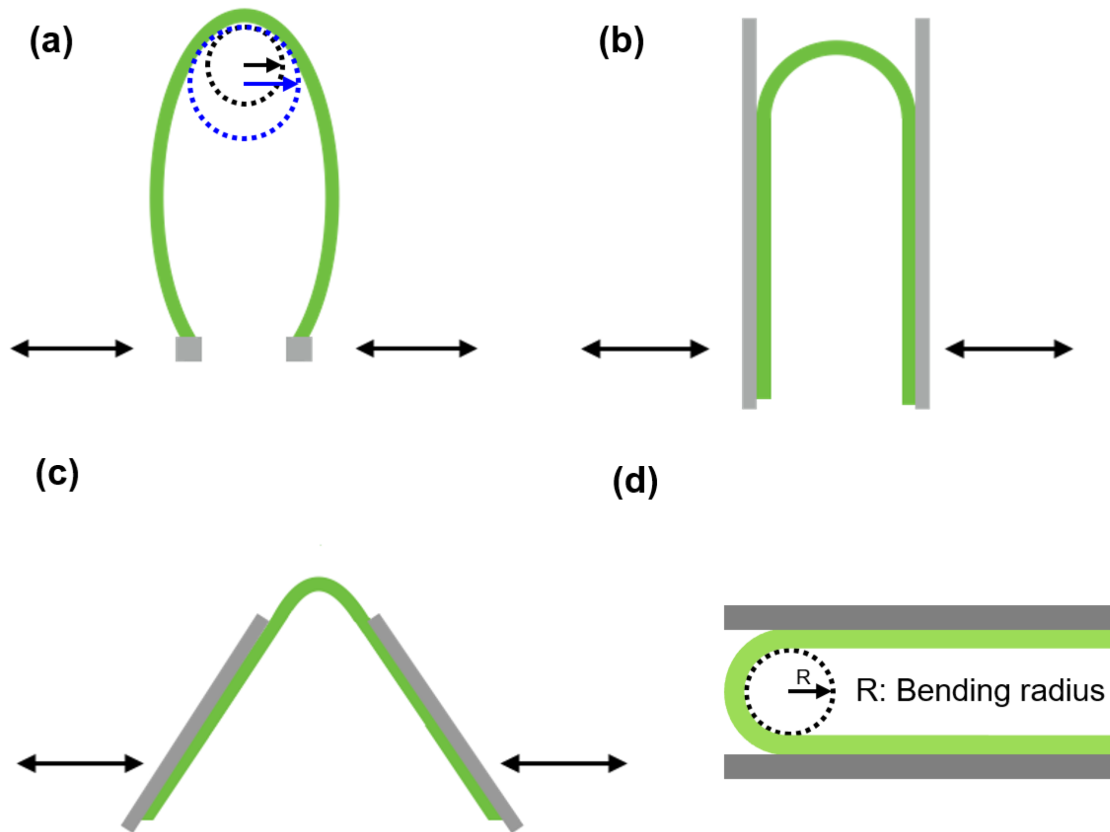

Figure.2.3. Illustration of the schematic diagram and corresponding folding simulation results of the bending system, respectively. (a) free-arc bending system (b) Guiding plate enhanced bending system (c) Folding system. (d) Bending radius is carefully measured to the inside curvature.

As one can see, all of the bending tests described above show limitations. After many test and trials, we concluded that the best design will be an automated procedure, excluding human interaction entirely, and that the ideal setup would be: (i) imposing uniform bending strain, (ii) applying accurate bending strains, control strain rates and forces, (iii) minimizing contact with the sample, and (iv) automatically measuring and calculating all relevant device performance parameters in real time. It will be a challenge to design an equipment with all of these requirements but it will certainly yield incomparably more reliable data.

Our Setup

It is important to choose an appropriate bending test setup that can imitate a real-life situation. In order to create such an equipment, the mechanical flexibility of DMD multilayer structure was evaluated first by using a setup made in our lab. Our tool allowed us to perform both the cyclic fatigue test and one-time fracture test. We tested multiple electrode samples based on strain rate, bending radius, and number of cycles.

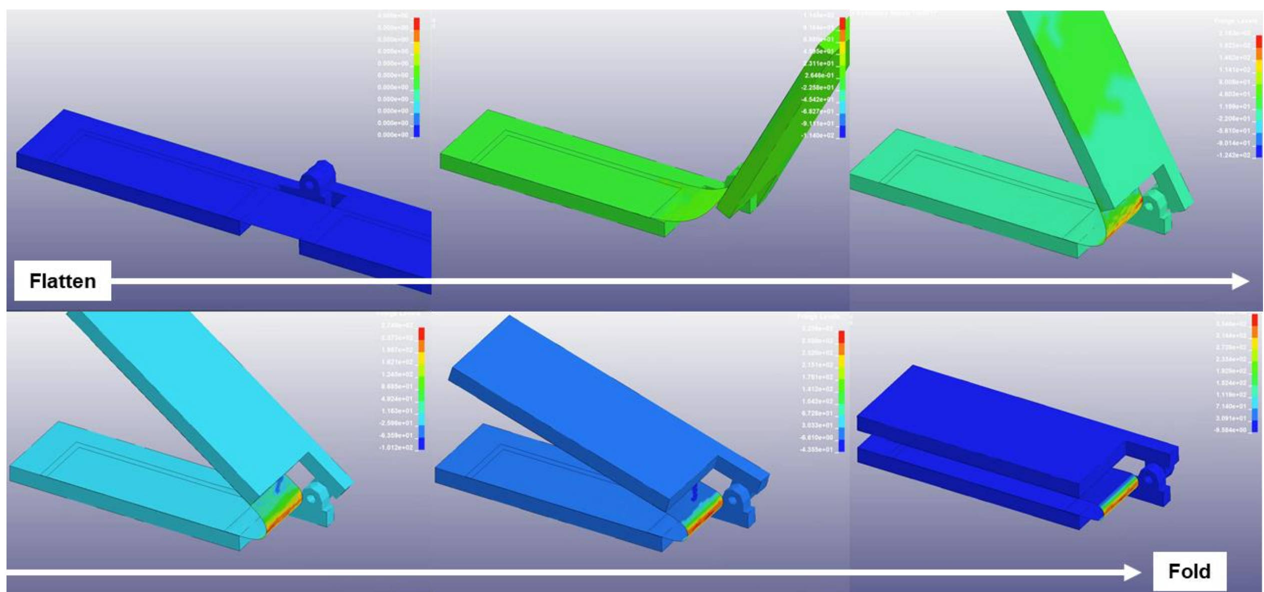

Figure.2.4. Strain analysis of our bending tester by finite element analysis: It demonstrates stress is localized on a bending region. It demonstrates stress variance depending on the position and sample deformation.

By conducting finite element analysis, we found that this bending operation induces localized stress at the folded region and a crack will initiate in this area. Based on this simulation result, we carefully designed our own bending test setup with two particular specifications of a design in mind: one that will provide an accurate bending radius and minimize any unintended stress. We successfully created a triple hinge system, which transformed linear back and forth motion to foldable motion while maintaining the full contact between the electrode sample and

the bending stage. In addition, 5mm-thick rubber components were attached to the guiding plate to prevent any buckling failure of the test sample.

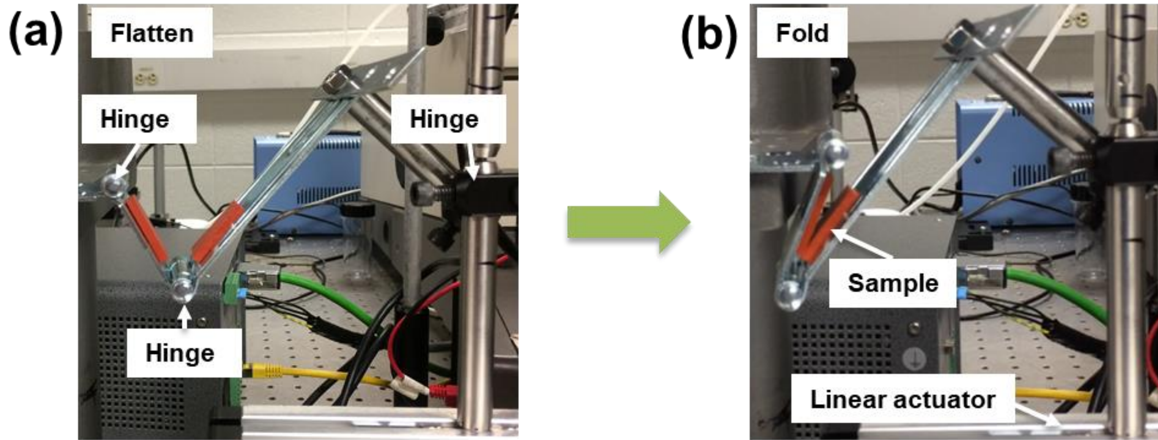

Figure.2.5. Sequential images of our bending tester operation: From (a) flatten to (b) fold state. It is possible to control strain rate (0.01%/s to 1.5%/s) and travel distance (1mm to 20cm).

Based on simulation results as plotted in Figure 2.6, we can verify that stress level is higher in the folding test setup. In addition, electrical resistance of both samples measured in situ during bending. Rapid resistance increase was detected in folding system. In contrast, it shows gentle increase in free arc bending system.

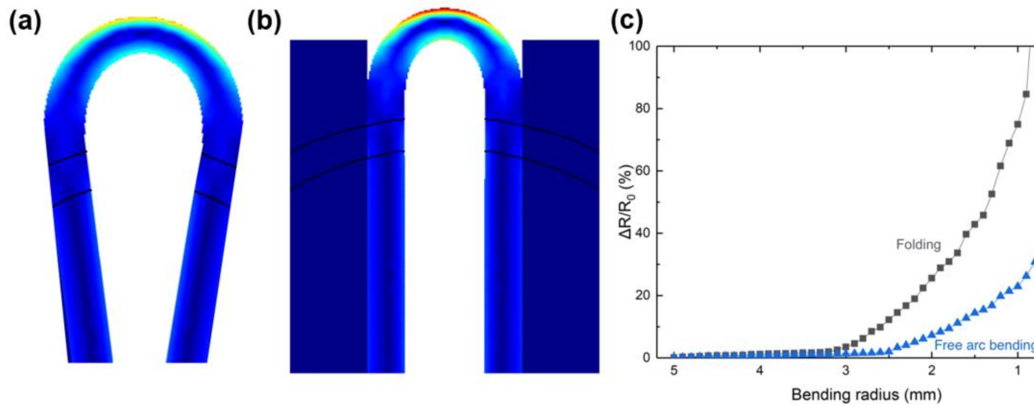

Figure.2.6. Stress distribution results between (a) free arc bending and (b) folding system. Stress level is higher in folding system compared to free arc system. (c) Bending test results of DMD films on PET. Electrical resistance of both samples measured in situ during bending. Folding system provide an accurate bending radius and severe bending stress

DMD Electrode Fabrication

The Cu-doped Ag films were co-sputtered on 50μm-thick polyethylene terephthalate (PET) substrates by a DC magnetron sputter tool (Lab18, Kurt J. Lesker Co.) with Argon (Ar) gas at room temperature. The chamber base pressure was pumped down to about 1×10^{-6} Torr before the film deposition. During deposition process, the Ar gas pressure was 4.5 mTorr and the substrate holder was rotated at a rate of 10 rpm. All films were deposited sequentially without breaking vacuum. DMD samples were fabricated using 40 nm ITO for each layer with the 10 nm CuAg layer sandwiched in between. Silver has long been known as the highest quality conductive material, however its usage has been limited due to practical issues of continuous thin film formation, stability, adhesion, and surface roughness. In order to solve the above mentioned issues, doping a proper amount of copper during silver deposition was proposed. Two pure Cu and Ag targets were co-sputtered to create Cu-doped Ag films. By varying the source powers for Cu and Ag targets, the composition of sputtered films was adjusted.

Bending Performance Evaluation of a DMD Structure

Mechanical failure is a major concern in many of these applications, particularly when materials are under bending stress. The failure is typically governed by local bond breakage at preexisting defects [25, 36]. The capability of a material with energy absorption before fracture is defined as fracture toughness, and this is a critical mechanical property of interest because it determines the structural integrity and reliability of flexible electronics. It is important to characterize the mechanical behavior of flexible transparent conductive electrodes to ensure mechanical reliability. Mechanical properties of interest typically include elastic modulus, yield

strain, crack onset strain (COS), and fracture energy. Among these, the crucial and simple reliability parameter when characterizing brittle thin films on polymeric substrates is the COS [34, 35]. COS is the strain at which cracks are first detected. Since mechanical strains may occur during manufacturing process (in a deposition process or roll-to-roll setup) or in various operations (twining, stretching, or bending), it is important to make sure that the electronic device tolerate well below COS. Any cracking will result in immediate and substantial failure of the device as a whole.

To evaluate the difference between ductile and brittle behavior, indium tin oxide (ITO) and DMD films on polyethylene terephthalate (PET) were tested. The most common method to determine the electromechanical behavior of conductive thin films used in flexible electronics is to perform a bending test by changing the bending radius. We mounted samples with 30mm-long and 10mm-wide between the two plates with the conductor on the outside at an initial radius of 20mm. In this configuration, the conductive films were assessed under different bending stresses. Electrical contact was made through the clamps and the resistance was monitored with Keithley 196 multimeter to see the dynamic measurement of electrical resistance variance (two-point method) during bending. Figure 2.7 (a) shows the results of measuring two-point resistance as a function of bending radius. And the corresponding bending radius are given as a function of crack density. When the sample fails, the resistance R rapidly increases.

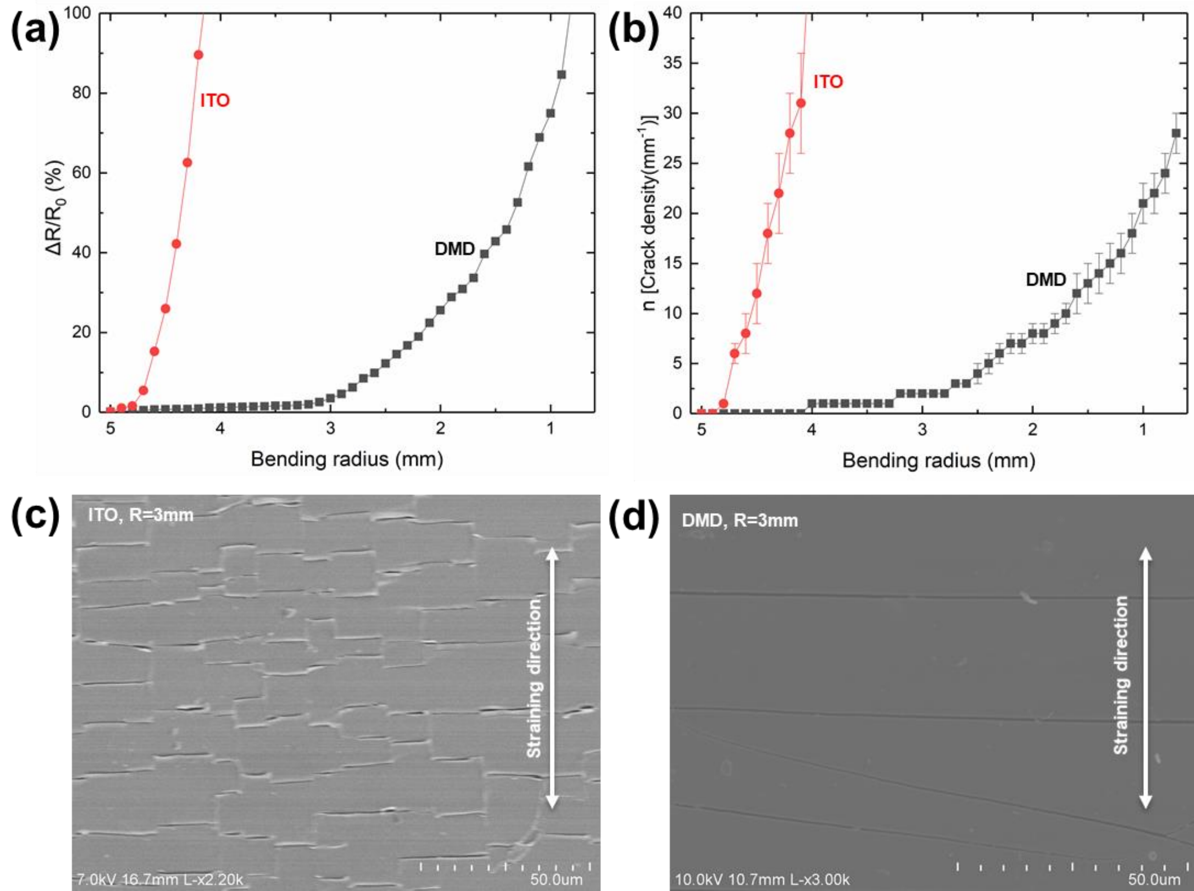

Figure 2.7. Bending test results of ITO and DMD films on PET. (a) and (b) Electrical resistance of both samples measured in situ during bending. (c) and (d) SEM images of the same surface area taken at bending radius R=3mm.

The flexible electrode that is bent at a specific bending radius undergoes two kinds of stress states: tensile stress on an outer bending and compressive stress on an inner bending. In case of DMD, which stays well attached to the substrate surface, it will endure the same stress state as the bent substrate surface. Therefore, the failure of the electrode depends on the amount of deformation in the bent substrate, which is generally determined by the radius of curvature and thickness of the substrate. The strain (ε) is proportional to the sample thickness (t) and is inversely proportional to the bending radius (R), as in equation below (2.1):

$$\varepsilon\ (Strain) = \frac{t\ (thickness)}{R\ (Bending\ radius)} \quad (2.1)$$

Sheet resistance increases in both DMD and ITO electrodes when bending radius is decreased. The number of cracks prove that the fracture of both electrodes depend on the radius of curvature.

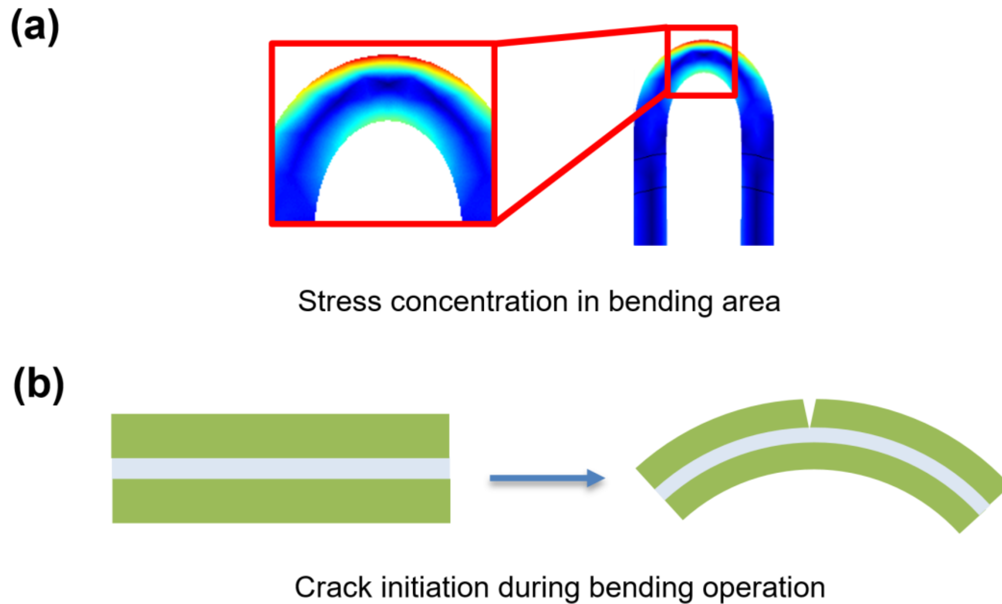

Figure 2.8. (a) Simulation results of bent substrate. The strain is proportional to the sample thickness and inversely proportional to the bending radius. Apparently, bending induced localized strain and (b) Bending induces localized strain near the folded region, and crack will initiate mainly in this area.

The DMD and ITO films exhibit a large difference in $\Delta R/R_0$ with a decrease bending radius. The resistance level of ITO films abruptly increased at the bending radius of 5mm and a further decrease rapidly increased the resistance value due to crack formation and propagation in the top surface of ITO layer. The DMD samples also showed increasing resistance under decreasing bending radius, but it was more gradual, due to the nature of their flexibility.

A rapid increase in relative resistance indicates a critical crack density that affects the measured resistance. This could also be related to the propagation of first cracks across the whole width of the sample. An SEM image showing the same area of ITO film and DMD on PET substrate at bending radius 3mm is given in Figure 2.7. It can be clearly seen that at this bending radius, only few cracks are observed in DMD structure within the viewing area whereas in the ITO sample, a dense network of channel cracks are visible and buckle delamination has formed. The response of DMD structure suggests that the ductility of the CuAg layer provided enhanced electrical conductivity when the ITO film clearly failed. Even more, the electromechanical properties and flexibility were significantly improved in the DMD structure as opposed to those of ITO structure. This improvement of mechanical properties is attributed to the existence of metal layer between the ITO structures.

In addition, in case of DMD structure, the strain level of the top ITO layer decreased because of shear deformation of the metal layer. The top and bottom ITO layers during bending are not coupled rigidly because the transverse sectional plane of the metal layer largely deformed transferring the shear stress. The bending stress was reduced with increased compliance of the structure compared to the bare ITO structure. In a metal layer, Ag bond rupture plays a critical role in resisting crack growth since a big part of the fracture energy is associated with plastic deformation near the crack tip. It helps with the prevention of rapid crack propagation and transfers efficient stress between two components. At bending radius of 3mm, the electrical resistance of DMD structure exhibits very stable optoelectronic performance, making them far more robust for easy handling and operation.

Crack Geometry Inspection: Crack Varies Depending on the Bending Radius

SEM images of various stages of the DMD layer during the bending tests are presented in Figure 2.9. Under continuous bending, the first crack, which was almost perpendicular to the bending direction, propagated at the tip but it did not continue all the way to the end. Instead, the crack stopped halfway, and another crack began to initiate from the other crack tip, which also stopped halfway and subsequently propagated to the edge of the DMD layer. This behavior indicates an improved crack resistance compared to that of the ITO structure. Furthermore, another crack in the front began near the freshly formed crack tip on the left side and propagated in a direction not orthogonal to the bending direction toward the edge, resulting in complete fracture. As can be seen, a blunted crack can be observed, which suggests that the plastic deformation within the DMD layer occurred during the bending test. Fracture occurred soon after the voids-like cracks merged, and the void cracks grew together to form a macroscopic flaw and created channeling cracks.

Crack extensions are developed by the coalescence of micro-void cracks. This void crack nucleation is frequently observed in a ductile materials. When void nucleation occurs, the fracture properties are controlled by the growth and coalescence of voids. The electrode results in failure when the growing voids reach a critical size (approximately 1μm in the case of DMD) and when a local plastic instability develops between voids.

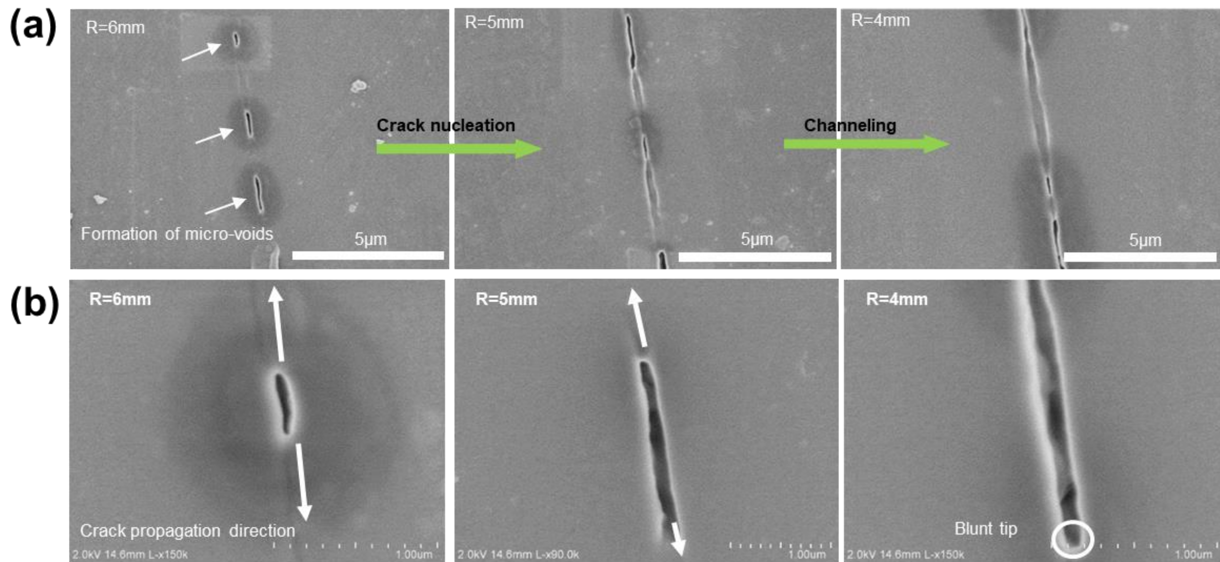

Figure 2.9. Representative SEM snapshots of propagation of the initial crack. (a) As bending radius is getting smaller, small crack (500nm long) merged together and channeling crack was created. (b) Crack dimension was also increased depending on the bending strain. Blunt crack tip was detected due to the ductile layer.

Griffith's Strain Energy Release Rate

Alan Griffith's energy-based analysis of cracks in 1920 is considered to be the birth of the field of fracture mechanics [21, 25]. He was motivated by Inglis's linear elastic solution for stresses around an elliptical hole, which predicted that the stress level approached infinity as the ellipse flattened to form a crack. Griffith compared the work to break atomic bonds to the strain energy released as a crack grows.

Griffith’s pioneering studies on the brittle fracture of materials triggered additional research on fracture mechanics. The stress intensity factor, K, introduced by Irwin, characterizes the stress condition in the vicinity of crack tip and explains the crack driving force based on linear elastic fracture mechanics (LEFM). The field of fracture mechanics has been extended to nonlinear materials, such as J-integral or cohesive zone model, allowing fracture phenomena in

nonlinear elastic materials (plastic or ductile materials). Thus, the field of fracture mechanics has shaped a theoretical framework for the design and engineering of materials for researchers and industries that demand high reliability. However, at the nanoscale, fracture mechanics encounter new challenges. It is well known that the fracture mechanics of nano-scale materials is significantly different from those on the macroscopic scale. Specifically, DMD layer is consisted of few nanometer thin films and the thin films have unique fracture characteristics. Thus, there are extensive research efforts underway to explain the fracture mechanics of nanoscale materials. However, the nanoscale experiments involved in such studies remain a challenge due to its difficulty in predicting crack propagation direction in a multilayered structure.

Table 2.1 Summary of different criteria found in literature

Criterion	Comments	Fracture occurs if	Relevant formulae
Griffith (σ_f)	Involves crack length	$\sigma \geq \sigma_f$	$\sigma_f = \sqrt{\frac{2E\gamma_s}{\pi c}}$
Irwin [K]	Concept of stress intensity factor	$K_I \geq K_{IC}$	$K_I = Y\left(\sigma_0\sqrt{\pi c}\right)$
Irvin [G]	Energy release rate based. Same as K based criterion for elastic bodies. Plastic deformation	$G \geq G_C$	$\sigma_f = \sqrt{\frac{2E(\gamma_s + \gamma_P)}{\pi c}}$

Energy Principles

In order to understand Griffith's fracture work, we must understand the basic principles of work and energy, and especially strain energy density. Work (W) is the mechanical form of energy and is given by:

$$W = \int F\, dx \tag{2.2}$$

For mechanics calculations, it is often convenient to calculate work in terms of stress and strain rather than force and displacement:

$$W = \int (\frac{F}{A}) \times (\frac{dx}{L}) V \tag{2.3}$$

We can convert this into the energy form:

$$U = \int \sigma \times d\varepsilon\, V \tag{2.4}$$

The integral is strain energy density. It is strain energy per unit volume (U′). We can insert Hooke's Law, σ = E × ε, into the integral for strain energy density:

$$U' = \int E\varepsilon d\varepsilon = \frac{1}{2} E\varepsilon^2 = \frac{\sigma^2}{2E} \tag{2.5}$$

Atomic Bonds and Surface Energy

Solids have an equilibrium spacing distance between pairs of atoms that make up a material. If they are too close, the atoms repel each other. If their distance is too far, the atoms attract each other. And at an intermediate distance, there is no net force between each other and they reach an equilibrium state. Imagine an atom being pulled away from its neighbor. The conceptual cartoon shows that the force required to move the atom initially increases as the atoms are separated. (The more the atoms separate, the more they attract each other.) But as the distance increases, the atoms eventually become separated very far that they no longer attract each other. By this point, the force will have leveled out, begin to decrease before eventually returning to zero. As shown in Figure 2.10 (b), the x-axis represents the displacement of an atom from its equilibrium position. Griffith proposed following conditions for crack propagation: (i) bonds at the crack tip must be stressed to the point of failure, and (ii) the amount of strain energy released must be greater than or equal to the surface energy of the crack faces created [25].

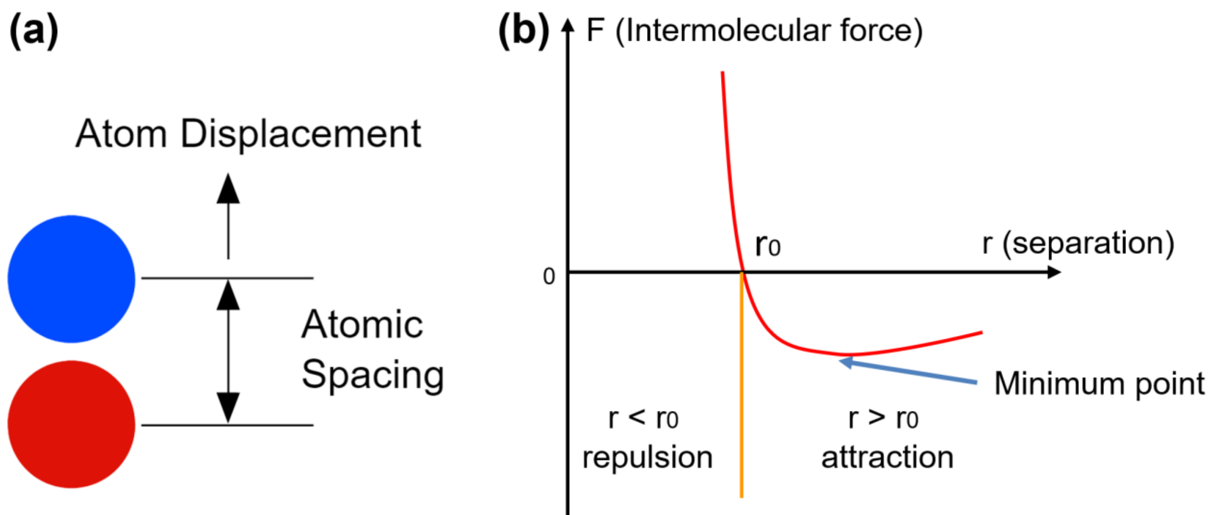

Figure 2.10. (a) In order to break a bond, applying force should be higher than cohesive force between each atom. (b) Schematic illustration of intermolecular potential energy diagram.

The above discussion presents the concept of atomic bond energy. In order to break a bond, an amount of work equal to the bond energy must be performed on the system. When a crack grows to a specific length, *a*, and has broken several atomic bonds along the way, there must be certain amount of work to overcome the atomic bond energy. The total energy is expressed as:

$$E_{bond} = 2\gamma_s aB \quad (2.6)$$

Here, γ_s represents the energy required to break atomic bonds per unit surface area created by the crack. The surface area is $a \times B$ where a is the crack length and B is the thickness. It is important to measure γ_s in relation to free surface area, and since there are two free surfaces (top and bottom) created by a crack, 2 is necessary in this equation.

Strain Energy Release Rate

According to the energy principles discussed above, we can assume that a crack propagates all the way across the bar, causing it to separate in two halves. Both halves will be unloaded following the break, so they no longer have strain energy. The original strain energy, *U*, has been released as a result of the propagation of the crack across the part:

$$U = \frac{\sigma^2}{2E} V - \frac{\sigma^2}{2E} B\pi a^2 \quad (2.7)$$

The result is surprisingly simple. According to a^2, the second term is subtracted from the strain energy as the crack length increases. If the crack length is zero, then the strain energy becomes zero, too. The quadratic dependence on crack length shows that the change in strain

energy with crack length at short lengths is very small, but then at longer lengths, it becomes very sensitive to the crack length.

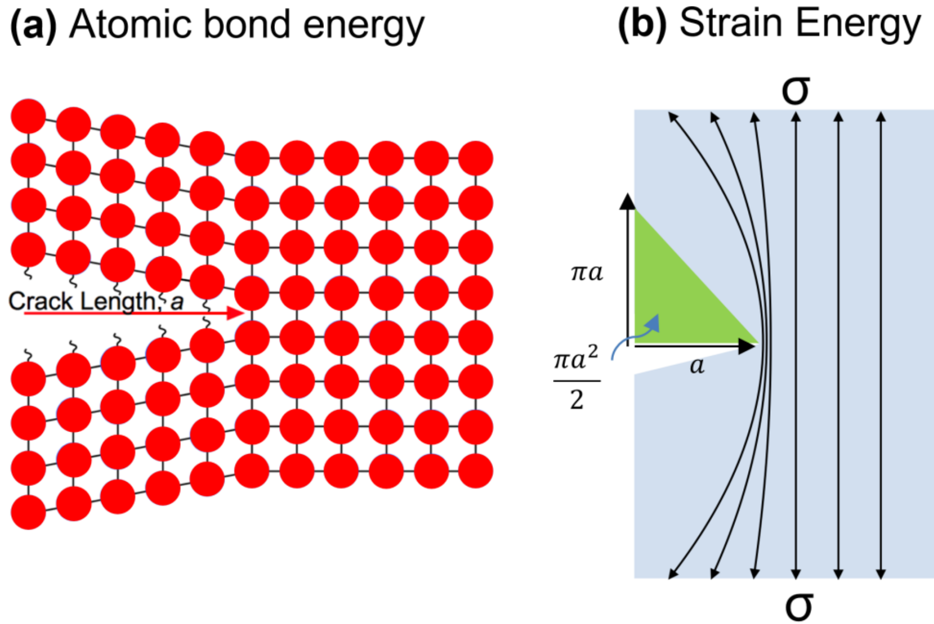

Figure 2.11. Schematic illustration of (a) atomic bond energy and (b) strain energy. Griffith proposed conditions for crack propagation: the amount of strain energy released must be greater than or equal to the surface energy of the crack faces created.

Griffith's Failure Criterion

The total energy in the system is simply the sum of the two expressions, as seen below:

$$E_{total} = 2\gamma_s aB + \frac{\sigma^2}{2E}V - \frac{\sigma^2}{2E}B\pi a^2 \tag{2.8}$$

In order to find the length at which the unstable crack growth can occur, we differentiate the total energy curve in respect to crack length, *a*, and then set the derivative to zero:

$$\frac{dE_{total}}{da} = 2\gamma_s B - \frac{\sigma^2}{2E}B\pi a = 0 \tag{2.9}$$

The following equation (2.10) shows that the failure stress increases with the square root of bond energy, γ_s, but decreases with the square root of crack length, a. Finally, the quantity $2\gamma_s$ is combined into the Griffith Critical Energy Release Rate, G_c.

$$\sigma_f = \sqrt{2\gamma_s E/\pi a} = \sqrt{G_c E/\pi a} \tag{2.10}$$

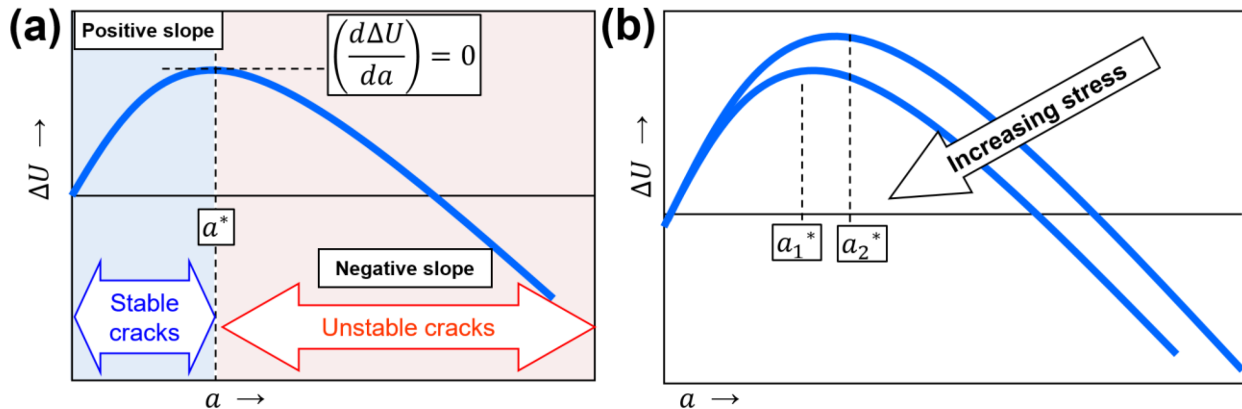

Figure 2.12. This change in energy (ΔU) should be negative with an increase in crack length (or at worst equal to zero). i.e. (dΔU/da) ≤ 0. And at a* the slope of ΔU is zero [$(d\Delta U/da)_{a*} = 0$]. This is a point of unstable equilibrium.

In Figure 2.12(a), it is important to recognize that for short crack lengths, the total energy of the object increases with increasing crack length. Therefore, additional energy must be input into the material in order to cause the crack to grow. It is stable region. However, at longer crack lengths an increase in crack length leads to a decrease in total energy. This means the crack can grow without any additional external load. This is an unstable situation that can lead to catastrophic failure as a crack abruptly propagates completely through a material. In the unstable zone, the crack can advance spontaneously. As expected, if applied load increases, the value of critical crack length (a*) decreases. This is because more elastic strain energy stored in the material. Therefore, this theory predicts that a crack will propagate to lower the total energy of the system, by dissipating the strain energy and creating a new surface.

Nonlinear Fracture Mechanic Analysis: J-integral

When getting closer to crack tip, we are entering the elastic-plastic deformation process zone especially in a ductile material, and the linear elastic fracture mechanics (LEFM) asymptotic solution is no longer valid [31]. Techniques for analyzing situations where there can be a large scale yielding will be presented and how to determine expressions for the stress components inside a plastic zone will be discussed, but first, it is important to review the J-integral. The J-integral represents ways to calculate the strain energy release rate, or work (energy) per unit fracture surface area, in a material. The theoretical concept of the J-integral was introduced in 1967 by Cherepanov and in 1968 by Rice, independently. Both explained that an energetic contour path integral was independent of the path around a crack tip. Next, experimental methods were developed, which allowed the measurement of critical fracture properties using lab-scale specimens for materials of sizes too small, and for which the assumptions of linear elastic fracture mechanics (LEFM) do not hold, and to infer a critical value of fracture energy J_{IC}. The J-integral is equal to the strain energy release rate for a crack in a body subjected to bending.

$$J = -\frac{d\Pi}{da} \tag{2.11}$$

J is defined as the total potential energy (Π) decrease during unit crack extension (*da*). This is still reasonable assumption, under quasi-static conditions, both for the linear elastic materials and for materials that experience small-scale yielding at the crack tip. Rice also showed that the value of the J-integral represents the energy release rate for the planar crack growth. The J-integral was developed because of the difficulties involved in computing the stress close to a crack in a nonlinear elastic or elastic-plastic materials. Rice demonstrated that if monotonic

loading was assumed (without any plastic unloading) then the J-integral could be also used to compute the energy release rate of plastic materials. This shows that it's a path-independent line integral, and consequently, it can be directly related to fracture toughness. The J-integral represents the rate of change in net potential energy in respect to crack advance (per unit thickness of crack front) for nonlinear elastic solids. It can also be thought of as the energy flow into the crack tip and a measure of the singularity strength at the crack tip for elastic-plastic material response.

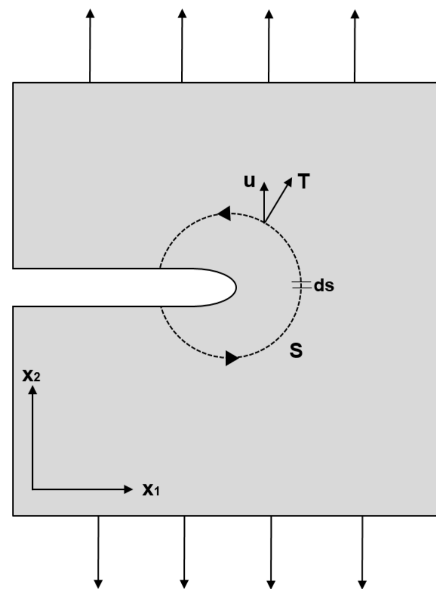

Figure 2.13 J-integral around a notch in two dimensions. We can use the following variables: S represents a curve linking the lower and upper crack surfaces. ds means an element of arc on this curve. T is traction vector on this curve defined in relation to an outward normal unit vector, i.e. $T = n \times \sigma$. u is the corresponding displacement vector.

Stress Analysis in the Vicinity of the Crack Tip

As shown in Figure 2.14 (a), we performed FEA based fracture analysis by using ABAQUS 2017 version to characterize critical stresses in the vicinity of the crack tips during fracture propagation and to investigate crack tip blunting effects. By using MATLAB, an image

processing algorithm was utilized to create 2D cracked models of both electrodes that were identically same in shape and size to both samples (Figure 2.14 (b) and (c)). The simulated stress results under bending test loading showed two distinct contours of stress level. Although this simulation result is not directly evident from the experimental stress data, the crack blunting behavior clearly demonstrated the occurrence of plastic deformation.

To calculate fracture toughness, we first simulated the stress contour by assuming nonlinear material behavior for DMD structure. A Young's modulus of 107 GPa and a Poisson's ratio of 0.33 was put into the FEA model and the sample was loaded uni-axially perpendicular to the crack face in a quasistatic strain-controlled manner. The contours of the principal stress of ITO and DMD samples were parallel to the bending direction as shown in Figure 2.14. In the DMD sample, the component in front of the crack tip reached a stress just above 0.6 GPa at the computational fracture stress (Figure 2.14 (c)). These results indicate that a nonlinear stress analysis, the J-integral approach, is appropriate in studying the fracture of DMD materials with nonlinear (nonlinear elastic, elastic-plastic) mechanical properties since CuAg layer has ductile characteristics. Figure 2.14(c) shows variation in stress as a function of distance away from the crack tip—perpendicular to the crack face—obtained using linear and nonlinear mechanical analyses. The stress contours for ITO at fracture stress is also shown in Figure 2.14(a). In ITO structure, the stress in front of the crack tip almost reached a stress of 1 GPa, which is 40% higher than that of DMD surface.

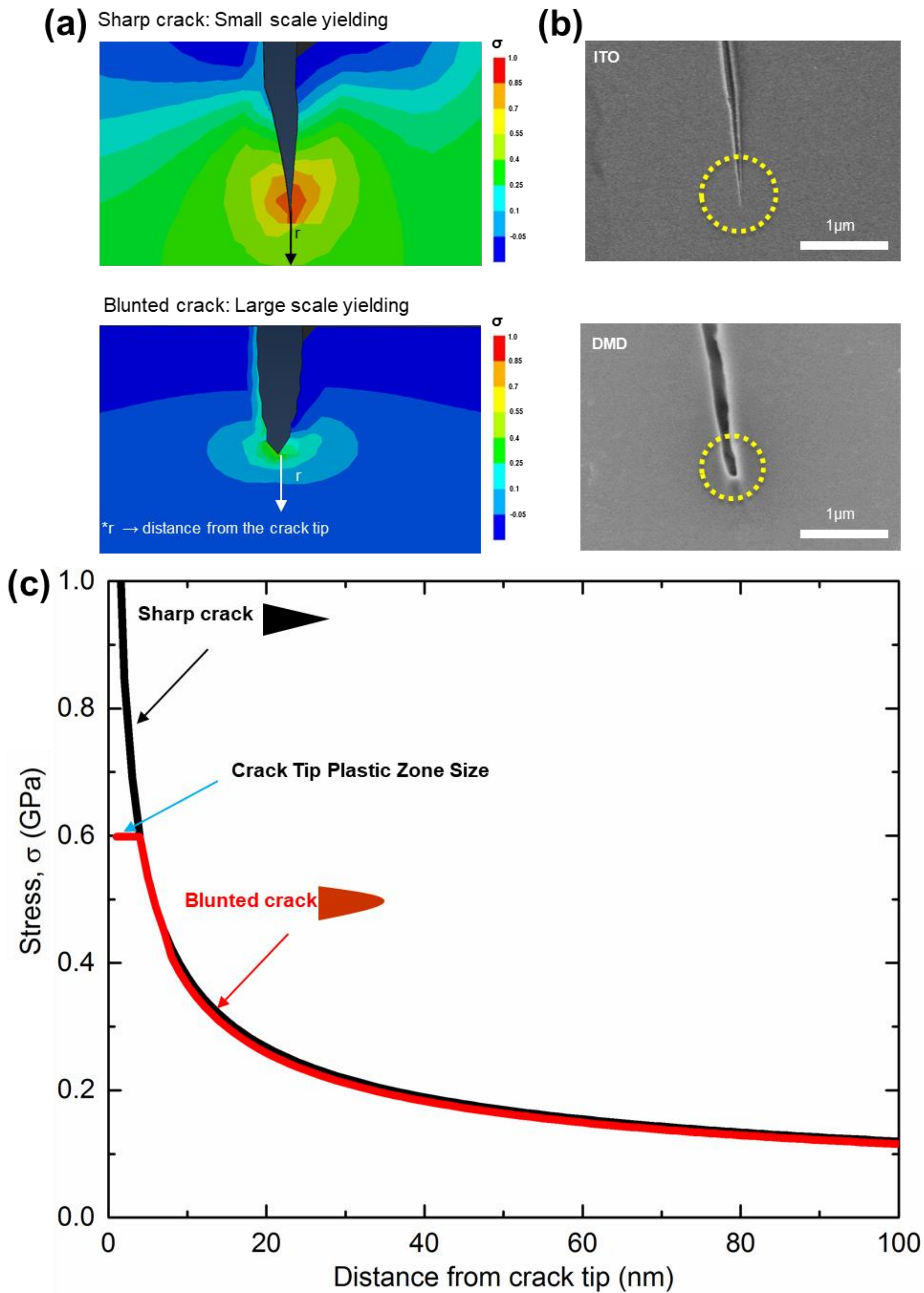

Figure 2.14. Crack dimension difference between ITO and DMD sample, simulation results of crack tip stress analysis of both electrodes. (a) Finite element analysis of stress contour in the vicinity of crack tip for both sample (b) SEM image of a cracked ITO and DMD sample. (C) Stress as a function of distance from the crack tip. A nonlinear zone from the crack tip is approximately 5.6 nm.

As depicted in Figure 2.13 (b), the crack in ITO sample showed sharp and narrow tip. In contrast, the crack tip of DMD sample was blunted by plastic deformation in the vicinity, suggesting that energy was spent in plastic deformation at the crack tip. From our simulation results, we can further add that high magnitude of crack tip stresses can cause a large-scale yielding at the crack tip due to the plastic deformation and subsequently lead to crack tip blunting. Energy is consumed due to plastic deformation at the crack tip, which comes from elastic strain energy. When comparing to the sharp crack case, this implies that less energy is used for crack growth and creating new surfaces.

According to the simulation in Figure 2.13, blunted crack tip leads to a reduced stress amplification. Blunting will avoid stress singularity at the crack tip and may lead to a maximum stress at a certain distance from the original point.

The capability of a material with absorbing energy before fracturing is defined as fracture toughness, and this is a critical mechanical property of interest because it determines the structural stability and reliability of the flexible electronic devices. The critical stress intensity factor, toughness and critical strain energy release rate of CuAg layer were calculated based on linear and nonlinear fracture mechanics by using experimentally measured crack lengths, width, stress intensity factor and fracture toughness, and this is summarized in Table 2.2 in the following page.

Table 2.2. Summary of crack dimension analysis of CuAg layer

Bending radius (mm)	5	4	3	2	1	0.8
Strain (%)	0.83	1.25	1.67	2.08	2.5	3.12
Crack zone span (μm)	10	20	55	250	375	900
Crack length (μm)	0.23	0.4	1.8	12.1	20.1	Fully channeling
Crack width (μm)	0.1	0.15	0.2	1.2	1.8	2.1
Crack density (n/mm)	1	3	12	16	21	28
Stress intensity factor, K_{Ic} (MPa√m)	11.38	14.49	19.09	25.47	33.77	n/a
Energy release rate, Toughness, G_{Ic} (J/m²)	1.62	2.62	4.56	8.11	14.26	n/a

Bio-Inspired Toughening Mechanisms in a Hierarchical Structure

Biological materials are omnipresent in the world around us [35 - 37]. They are the main constituents in plant and animal bodies, and they have many functions. A fundamental one is to provide protection and support for their bodies. A multilayered biologically natural materials, such as tooth enamel, glass sponge skeletons, or nacreous part in mollusk shells exhibit both superior strength and toughness through hierarchical multilayer structure. The nature nacre has a micro-structure where aragonite platelet layers are bound by an organic matrix. Their mechanical performance is attributed to structural features at multiscale levels. While high mineral contents provide stiffness and hardness, these materials also contain weaker and ductile interfaces with elaborate architectures. The secret to key success is their hierarchically ordered multilayer structure at multiscale levels. The structure of these materials is organized over several distinct

hierarchical length scales, from the nanoscale to the macroscale [35,37]. Tooth enamel is made of long rods perpendicular to the bottom surface and are held together by proteins. In tooth enamel, cracks typically emanate from the surface because of repeated contact or impact stresses. Initially, the cracks are channeled away from the surface, preventing chipping of the enamel surface. The rods bend deeper within the enamel and forms a complex decussation, which impedes further crack growth. Similarly, nacre is made of microscopic tablets of calcium carbonate, where proteins and polysaccharides hold the structure together [36].

Crack deflection is a unique behavior in multilayered structure, with a soft and ductile layer providing additional energy dissipation at the interface [38, 39]. Ductile layer controls slip and nonlinear deformations at interfaces, so a brittle ductile hybrid structure is effective when absorbing impact energy and preventing rapid crack propagation. This bio-inspired approach provides a new pathway to toughening ITO or other brittle materials. The DMD structure, in contrast, yields enhanced electromechanical performances when subjected to severe bending situations since it is consisted of both brittle and ductile hierarchical structures.

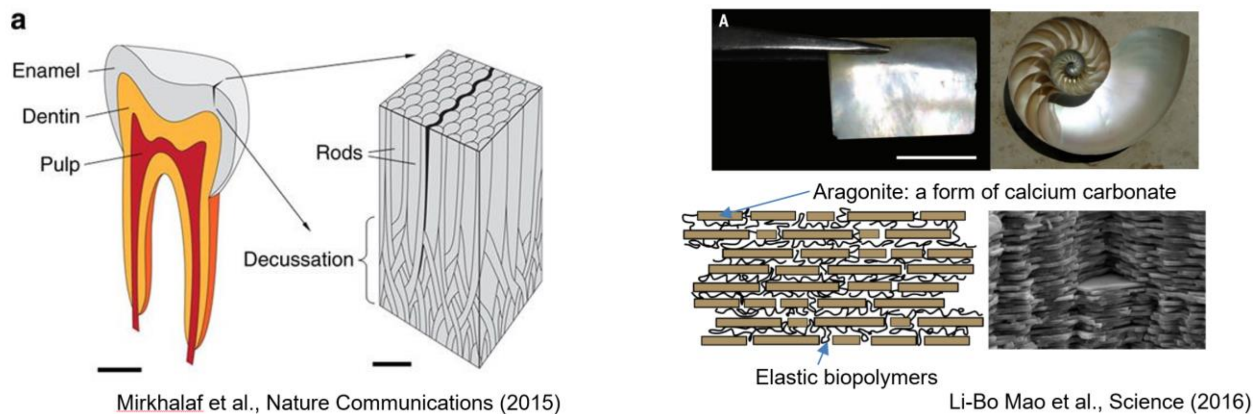

Figure 2.15. It illustrates bio-inspired hierarchical structure of human teeth and nacre layers from nature.

Crack Deflection in DMD Multilayer When Subjected to Bending Operation

At bending radius R=5mm in DMD multilayer, we found that when the crack tip approaches the CuAg layer, the crack is abruptly deflected to the lateral direction and continues to propagate along the metallic layer (Figure 2.16), creating a very unusual step-like crack. Such a marked deflection in crack trajectory can be interpreted as the competition between the direction of maximum mechanical driving force and the weakest structural pathway. It is assumed that the ductile layer of the thin film metal can greatly improve the mechanical properties of the whole DMD structure due to internal interfaces. A DMD multilayered material can dissipate crack energy more effectively than an ITO structure. Specifically, from a mechanical perspective, cracks in nominally brittle materials follow the path of maximum strain energy release rate.

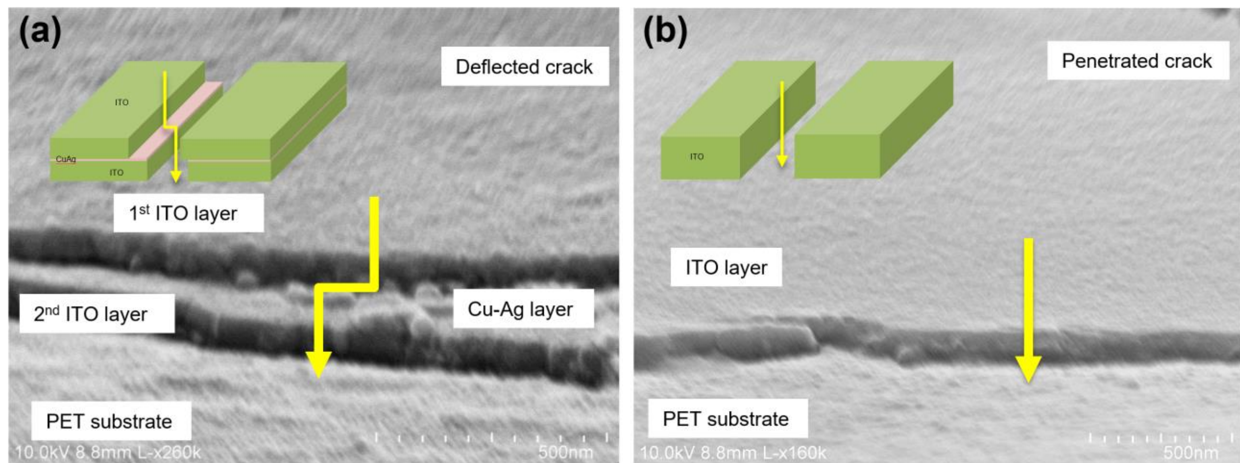

Figure 2.16. It shows SEM (cross-sectional fractured surfaces) images of crack propagation at bending radius (R=5mm). (a) The path of the cracks meanders alternately along with CuAg interfaces, and then cutting through bottom ITO layer (b) In ITO sample, there is only penetrated crack when subjected to bending.

In the crack propagation process, CuAg layer plays an important role in preventing rapid crack propagation as it absorbs energy through large shear deformations and strain energy

transfers to plastic deformation. Again, this can be seen in the step-like fracture in the DMD multilayered structure. Both He and Hutchinson's crack-deflection mechanics solution and FEA simulation results further explains this phenomenon [39].

The Linear Elastic Crack Deflection Mechanics Solution by He and Hutchinson

To better understand the development of crack deflection behavior in a DMD structure, Dundurs' elastic mismatch parameter model is proposed. This derivation can be obtained from He and Hutchinson's linear elastic crack deflection mechanics solution, which considers the possible situation of a crack impinging on a bi-material interface as seen in Figure 2.17 [38, 39]. Based on their conclusion, the impinging crack from normal direction will either penetrate through the interface and propagate into the bottom ITO layer or deflect along with the metal layer. The outcome fully depends on the elastic mismatch across the interface (which is a function of the relative elastic moduli) and the ratio of fracture toughness of the interface and the material on the far side of the interface towards where the crack is propagating. Deflected crack is the more robust mechanism to prevent rapid electrical failure compared to penetrated crack. Electrically, penetrated crack represents the worst-case scenario as it damages the metallic layer. He and Hutchinson analysis provides a simple and quantitative criterion to predict whether a singular crack from normal direction will deflect along or penetrate through a linear-elastic bi-material interface.

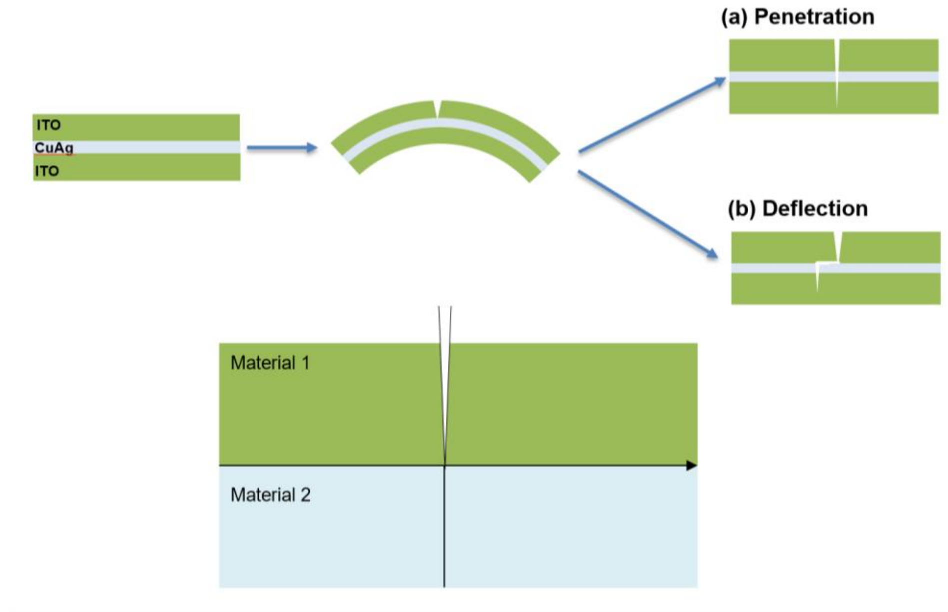

Figure 2.17. He and Hutchinson provide a quantitative analysis tool to predict whether an impinging crack will penetrate through whole layer or deflect along with a linear elastic bi-material interface.

Derivation for Energy Release Rate

The toughening mechanism is primarily associated with two-dimensional deflection of cracks that bypass the thin metallic layer. In a multilayered structure, a crack may be trapped and grow along an interface between two different materials under mixed mode. Crack tip stress field depends on the elastic mismatch and may have different singularity [38, 39].

He and Hutchinson successfully explained this unique crack deflection theory based on elastic mismatch parameters [37,39]

$$\alpha = \frac{E_1 - E_2}{E_1 + E_2} \qquad \beta = \frac{[\mu_1(1-2\nu_2) - \mu_2(1-2\nu_1)]}{[\mu_1(1-\nu_2) + \mu_2(1-\nu_1)]} \tag{2.12}$$

It is necessary to examine a single case (e.g., $\alpha > 0$) to fully understand the elastic properties of the bi-material in this work. Irwin showed fracture in a solid in the form of crack growth is

governed by the stress field around the crack and the stress field in the vicinity of an infinitely sharp crack tip could be described mathematically [63, 64]. We assume that the approach of calculating only the asymptotic stress fields will be taken, following the analysis of Williams [65]. In problems where the semi-infinite reference crack of $a = 0$ is perpendicular to the interface with its tip at the interface, a symmetric loading with respect to the crack plane is applied, and the stress σ_{xx} in the material ahead of the crack in material is characterized by [58, 59, 62,63]:

$$\sigma_{xx}(0, y) = K_I(2\pi y)^{-\lambda} \tag{2.13}$$

where the three parameters K_I is named stress intensity factors corresponding to the opening mode (Mode I) of fracture. This expressions show that the stresses have an inverse square root singularity at the crack tip and the stress intensity factors measure the intensities of the singular stress fields of opening mode. Stress intensity factor, K_I quantifies the magnitude of the effect of stress singularity at the crack tip. In addition, λ is real, and it depends on α and β according to [61]:

$$\cos\lambda\pi = \frac{2(\beta - \alpha)}{1 + \beta}(1 - \lambda)^2 + \frac{2(\alpha + \beta^2)}{1 - \beta^2} \tag{2.14}$$

When we assume λ as a function of α for $\beta = 0$, the amplitude factor K_I is proportional to the applied loading, as shown in the Figure 2.18 below.

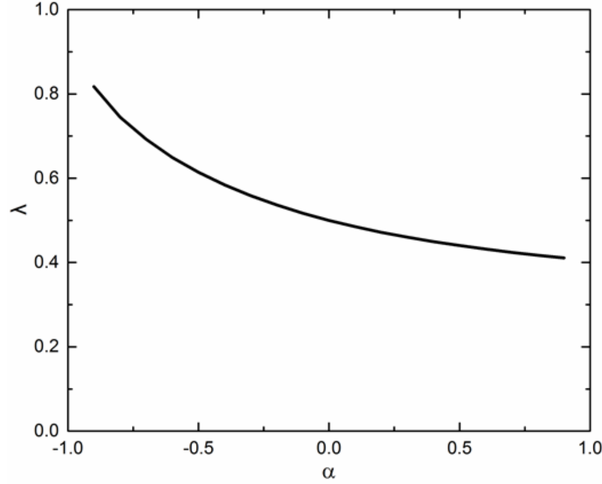

Figure 2.18. Assuming λ as a function of α for $\beta = 0$

In the case of penetration, the stress state at the advancing tip is pure mode I where *c* is a dimensionless number. Pure mode I is an opening mode when we apply any bending stress.

$$K_I = c(\alpha, \beta) k_I a^{1/2-\lambda} \tag{2.15}$$

The energy release rate for penetration is:

$$G_p = \frac{1-\nu_1}{2\mu_1} {K_I}^2 = \frac{1-\nu_1}{2\mu_1} c^2 {k_I}^2 a^{1/2-\lambda} \tag{2.16}$$

For identical elastic properties, $\lambda = 1/2$, but when material 1 is stiffer than material 2, $\lambda < 1/2$. When material 2 is stiffer than material 1, then $\lambda > 1/2$.

The traction on the interface directly ahead of the right-hand tip of the deflected cracks is characterized by [60, 61]:

$$\sigma_{yy}(x,0) + i\sigma_{xy}(x,0) = (K_I + iK_2)(2\pi r)^{-1/2} r^{i\varepsilon}$$

$$r = x - a,\ i = \sqrt{-1},\ and$$

$$\varepsilon = \frac{1}{2\pi}\ln(\frac{1-\beta}{1+\beta}) \tag{2.17}$$

In these cases, dimensional considerations require the following equation (2.18) where *d* and *e* are dimensionless complex valued functions of α and β:

$$K_I + iK_2 = k_I a^{1/2-\lambda}[d(\alpha,\beta)a^{i\varepsilon}+e(\alpha,\beta)a^{-i\varepsilon}] \tag{2.18}$$

Based on this, we can derive the energy release rate of the deflected crack, which is expressed as:

$$G_d = [\frac{(1-\nu_1)}{\mu_1} + \frac{(1-\nu_2)}{\mu_2}]\frac{\left(K_1{}^2 + K_2{}^2\right)}{4\cosh^2\pi\varepsilon} \tag{2.19}$$

Here, *c, d* and *e* are complex valued functions of α and β. Integral equation methods have been used to solve the function of *c* for the penetrating cracks, *d* and *e* for the deflected cracks.

Subsequently, we can plot an elastic mismatch parameter over the toughness graph by using this integral equation, and the relative tendency of a crack to be deflected by the interface or to pass through it can be assessed using the ratio below:

$$K_1{}^2 + K_2{}^2 = k_I{}^2 a^{1-2\lambda}[|d|^2 + |e|^2 + 2R_e(de)]$$

$$\frac{G_d}{G_p} = [\frac{(1-\beta^2)}{(1-\alpha)}]\frac{[|d|^2 + |e|^2 + 2R_e(de)]}{c^2} \tag{2.20}$$

And Table 2.3 in the following page summarizes the outcomes when calculating the variables using the equations above.

Table 2.3 The variables λ, c, h, d_R, d_I G_p, G_d (singly deflected crack) as a function of α

α	λ	c	d_R	d_I	d^2	c^2	$1-\alpha$	G_d/G_p
-0.9	0.8175	0.6104	0.0272	-0.6212	0.386629	0.372588	1.9	0.54615
-0.8	0.745	0.6877	0.0613	-0.6281	0.398267	0.472931	1.8	0.467847
-0.7	0.692	0.7493	0.1023	-0.5805	0.347446	0.56145	1.7	0.364021
-0.6	0.6495	0.783	0.1464	-0.5389	0.311846	0.613089	1.6	0.317905
-0.5	0.6142	0.8224	0.1877	-0.5005	0.285732	0.676342	1.5	0.281644
-0.4	0.5843	0.8595	0.2283	-0.463	0.26649	0.73874	1.4	0.257668
-0.3	0.5586	0.8953	0.2669	-0.4313	0.257255	0.801562	1.3	0.246879
-0.2	0.5364	0.9301	0.3043	-0.4017	0.253961	0.865086	1.2	0.24464
-0.1	0.517	0.9617	0.3381	-0.3741	0.254262	0.924867	1.1	0.249925
0	0.5	0.999	0.3707	-0.349	0.259219	0.998001	1	0.259739
0.1	0.485	1.034	0.4011	-0.3259	0.267092	1.069156	0.9	0.277573
0.2	0.4718	1.069	0.4292	-0.3044	0.276872	1.142761	0.8	0.302854
0.3	0.4601	1.104	0.4553	-0.2842	0.288068	1.218816	0.7	0.337644
0.4	0.4496	1.142	0.4823	-0.2662	0.303476	1.304164	0.6	0.387829
0.5	0.4402	1.181	0.5019	-0.2492	0.314004	1.394761	0.5	0.450262
0.6	0.4318	1.222	0.5226	-0.2327	0.32726	1.493284	0.4	0.547886
0.7	0.4242	1.267	0.5419	-0.2177	0.341049	1.605289	0.3	0.708178
0.8	0.4173	1.315	0.5601	-0.2041	0.355369	1.729225	0.2	1.027538
0.9	0.4111	1.368	0.5761	-0.1903	0.368105	1.871424	0.1	1.96698

The crack path depends on two principal factors. The first one is the elastic modulus mismatch of each material, described by the Dundurs' elastic mismatch parameter $\alpha = (E_{ITO}-E_{CuAg})/(E_{ITO}+E_{CuAg})$, where E_{ITO} and E_{CuAg} are the respective elastic moduli of ITO and CuAg layers. The second factor is the ratio of interface toughness (critical strain energy release rate) to that of material beyond the interface $G_{interface}/G_{CuAg}$, and we can derive this value through crack

dimension analysis. By substituting the material and interfacial properties of the current system into this analysis, we can calculate the elastic modulus mismatch for the ITO/CuAg equivalent to 0.365 with a toughness ratio $G_{interface}/G_{CuAg}$ of 0.27 (blue square dot). This solution is plotted in Figure 2.19 for the ITO/CuAg interface with a normally incident crack. It shows whether or not the crack will be deflected at the interface or penetrate through it based on the relationship between interfacial toughness and elastic modulus. When looking at it from a mechanical driving force perspective, the graph clearly shows that the crack will surely deflect along the ITO/CuAg interface.

A direct measurement of toughness of the ITO/CuAg interface is almost impossible, because it requires an accurate probing technique of the material interface with atomic resolution. Therefore, we utilized values from the literature, which state that G_c varies in the range of 0.2 – 0.35 $J \cdot m^{-2}$. For the toughness of ITO/CuAg interfacial layer, the absence of interface delamination leads to a competition between penetration and deflection at the ITO/CuAg interface. This result can be used to estimate that the interface toughness must be 30% of the toughness of the ITO for the latter phase to be effective in impeding the initial crack propagation.

A normal crack penetration (red square dot) represents the geometrically and electrically worst scenario; electrodes are damaged immediately before strain energy converts into plastic deformation. Using the values of elastic modulus for both the ITO and the CuAg layer, we can estimate that CuAg metallic layer is an effective barrier to the crack propagation. At bending radius R=5mm, the direction of the crack propagation is significantly different in comparison to that of ITO structure. The thin metal layer serves to dissipate strain energy from the occurrence of plastic deformation, greatly decelerating crack growth.

We believe that these findings will trigger future research to enhance the electrode fracture resistance by formulating an additional metallic layer, and these findings will enable us to develop more robust and stable electrode even at small bending radius.

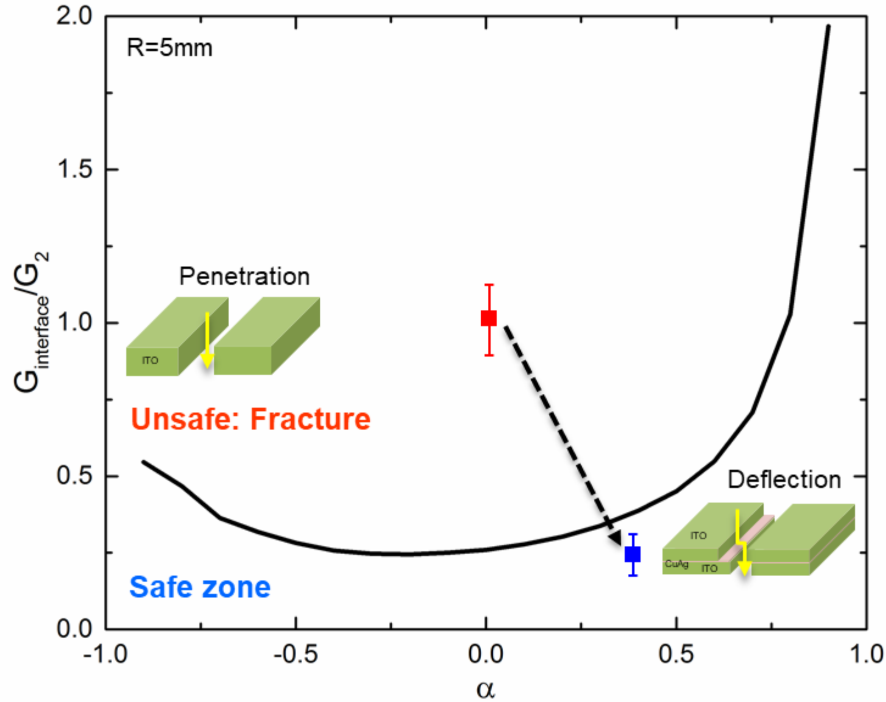

Figure 2.19. The linear-elastic crack-deflection mechanics solution of He and Hutchinson for a crack normally impinging an interface between two elastically dissimilar materials. (A) The curve marks the boundary between systems in which cracks are likely to penetrate the interface (above the curve, red square dot) (B) or deflect along the CuAg interface (below the curve, blue square dot).

Inspired from the nature, this hierarchical multilayer structure can affect the direction of crack propagation and delay electrode degradation. In result, the fracture toughness is increased and further catastrophic crack propagation is prevented. This mechanical analysis approach by He and Hutchinson provide a quantitative analysis tool to predict whether an impinging crack will penetrate through all layers or deflect along with a linear elastic bi-material interface.

Identify Young's Modulus of Each Layer

In order to design FEA simulation model properly, the basic material properties must first be identified. To understand the mechanic deformation during bending, it is very important to define some basic mechanical parameters. Strain is a dimensionless quantity describing the physical deformation of a shape. For example, tensile strain describes a shape elongated in respect to reference dimensions, compressive strain describes a compacted shape, and shear strain describes a deformation in which parallel planes within the sample are translated in-plane in respect to one another. These elastic modulus properties are commonly measured using techniques such as tensile testing, where samples are stretched in tension while recording the stress and strain, or with nano-indentation which is used to probe the properties of a thin film.

Characterizing thin materials on a substrate mechanically is challenging since the overall mechanical behavior is derived from a combination of the properties of all the materials present. This technique involves tracking the stress and strain curve. Young's modulus can be calculated after loading and unloading curves are collected. Among these, tensile test technique, inspired by Voigt, has been explored to measure the elastic moduli of small-scale, sub-micron thin films. Voigt proposed the effective elastic modulus of the multilayer as [25]:

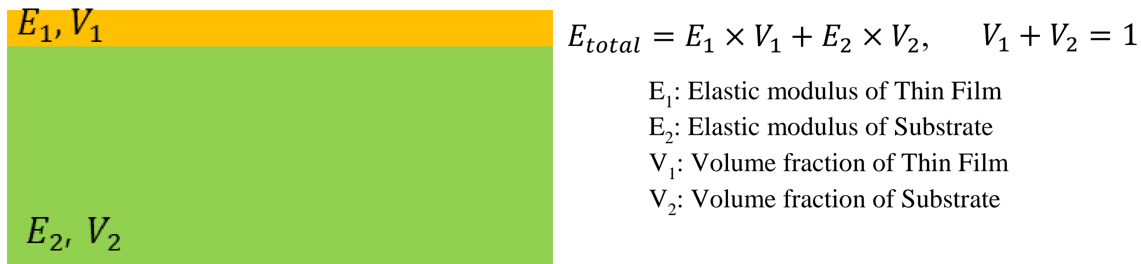

Figure 2.20. Schematic illustration of elastic modulus calculation for multilayer structure. Voigt proposed the effective elastic modulus of the multilayer.

This mixing rule is for the iso-strain state. This model assumes the constituents of a composite to be in parallel arrangement when subjected to the same strain. Because our structure is consisted of few nanometer scale, we can assume that the strain is identically same to each layer. Q800 dynamic mechanical analyzer (DMA) was used to identify and characterize elastic modulus of each layer. A controlled stress DMA is composed of a motor, which applies force (stress) to the sample and a displacement sensor that measures the amplitude (strain).

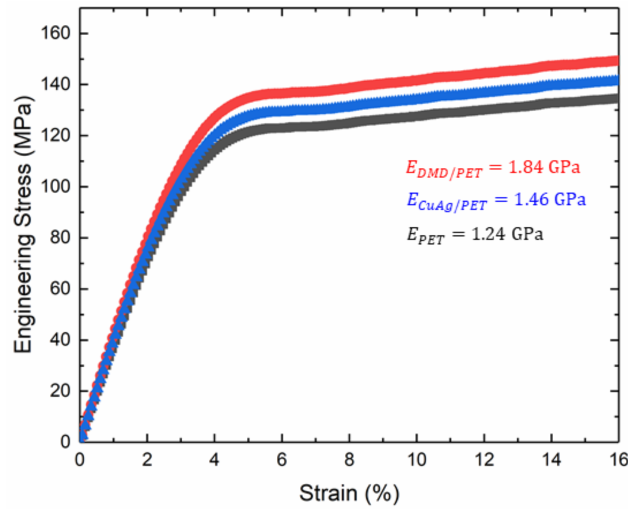

Figure 2.21. Based on DMA tensile test, it provides elastic modulus of each material. After extracting stress strain curve of each sample, by using Voigt's approach, we can calculate E_{DMD}=107.27GPa and E_{CuAg}=82.18GPa, respectively.

Crack Propagation Simulation by Cohesive Zone Model (CZM)

Deriving analytical formulae that describe mechanical behaviors is challenging as our flexible electrode is consisted of different dimensions and properties. In order to predict the behavior of more complex architectures, a numerical modelling technique known as FEA can often be employed. FEA is a valuable tool for mapping field variables such as stress, strain and displacement that result when simulated forces or deformations (compression, bending, stretching) are applied to virtual models. In FEA of a mechanical system, a body is discretized

into a collection of pieces called elements, and analysis is performed at nodes which lie at the intersections between the elements. Solutions generally involve maps of parameters of interest over the discretized body. The technique is extremely valuable for both exploring the influence of design parameters over device behavior (such as geometry and material selections) and for understanding the mechanisms of failure [31].

Several software packages can be utilized to implement FEA, including many different commercial programs like ANSYS, ABAQUS, and COMSOL Multiphysics®. In every simulation tool, the basic procedural steps are similar. There is pre-processing, which includes geometry construction and input of materials properties like elastic modulus and poisson ratio and discretization of the model. There is also analysis, which includes solution of relevant equations. And finally, there is post-processing that displays a solution. To perform an analysis, a physical system is first approximated as a model with geometry defined either within the FEA software or by importing from a separate computer-aided design program. In most FEA of solid mechanics, the solution is found by minimizing the strain energy of the system. A set of equations describe the strain energy density at each node and the optimum solution is the set of displacements that minimizes the overall elastic energy. From this solution, field variables, such as stresses and strains, can be calculated at the nodes or throughout the elements with appropriate interpolation. Results can be exported in tables or they could be visualized in a variety of form like graphs, photos and videos. While it is relatively straightforward to generate a model and evaluate a solution, demonstrating the validity is very challenging. The model should evaluate various scenarios with predictable outcomes and assess the logic of the generated solution. Moreover, it should be verified through a comparison with experimental data.

To predict the failure of DMD multilayer, delamination and adhesion at the interface must be shown within the model. One approach targets utilizing cohesive zone element model (CZM), treating delamination as a gradual separation of elements, and finally employing a traction separation law to relate the separation between nodes to a traction stress vector acting on those nodes. Within such a model, the traction separation vector increases to a critical value as the separation is increased. Beyond this critical value, the traction decreases, describing a softening or degradation of the interface. This CZM concept is used to illustrate that the crack tip process zone assumes bonds stretching orthogonal to the crack surfaces until they break at a characteristic stress level.

According to CZM, the fracture process is lumped into the crack line and is characterized by a cohesive law that relates tractions and displacements jump across cohesive surfaces (T-Δ). This nonlinear analysis technique is integrated in the FEA approach and the separation mechanism of two surfaces can be simulated. Generally, two implementation methods are used. Interface elements are designed specifically to represent the cohesive zone between the components and to account for the separation across the interface. And the cohesive zone between components are modeled with bonded contact. In our simulation, ABAQUS 2017 version was used to determine the in-plane stress and strain fields during bending. It was also used to study crack initiation, propagation, deflection, and delamination on a flexible electrode subjected to multiple bending radius. The ITO layer was modeled as an isotropic elastic material with an elastic modulus of 150 GPa and a Poisson's ratio of 0.33. The CuAg layer was modeled as an isotropic elastic material. Depending on the strain rate, the elastic modulus and yield strength of CuAg layer vaied in the range of 80 - 85 GPa and 60-65 GPa, respectively.

The crack propagation paths were plotted to study the crack direction of the electrode

depending on the structure. Since surface defects such as voids are preferential sites for crack initiation, a pre-defined crack (5nm long) was assumed in the model. As shown in Figure 2.22, when subjected to bending (R=5mm), the crack initiated in ITO layer and deflected along with ITO and CuAg interfacial layer in the DMD structure. In the pure ITO structure, however, the crack was penetrated all the way to the bottom of ITO layer. These simulation results are consistent with the experimental observations. The yellow arrows in the figure indicate the general direction of crack propagation. The crack predictably is deflected along the ITO/CuAg interface, because this is the weakest structural path and more energetically favorable.

The present work provides a mechanical explanation of the root cause of premature transparent conductive electrode failure in DMD structures during bending. And on the basis of our findings, we demonstrate how the thin metallic layer change the mechanical robustness, tune the mechanical properties of the cohesive layer, and improve the electrode fracture resistance. In addition, our proposed failure analyses may also guide the optimization of other strategies, including surface modification, electrode material development, and tuning of the charge profile to increase the material ductility and suppress the high surface stress. We consider the knowledge of the failure mechanisms of transparent conductive electrodes gained from the present study as a foundation for future design improvements, and we use the aforementioned strategies as our main path towards the development of more robust and durable conductive electrodes for next-generation wearable electronics.

To simulate the cracking-induced interfacial delamination, the ITO/metal/substrate interface was modeled as an array of nonlinear springs with these parameters: interfacial strength and shear strength, critical opening displacement and sliding displacement, and the areas under the traction-displacement curves (i.e., the normal and shear adhesion energy of the

ITO/metal/polymer interface, respectively). The ITO/metal/polymer interface was meshed with four-node cohesive elements sharing nodes with the neighboring elements in the film and the substrate. Supported by a polymer substrate, the bending fracture of the DMD and ITO thin film involved the initiation and propagation of multiple channel cracks. It can be easily observed that there was a subsequent increase and saturation of the crack density as the applied tension increases.

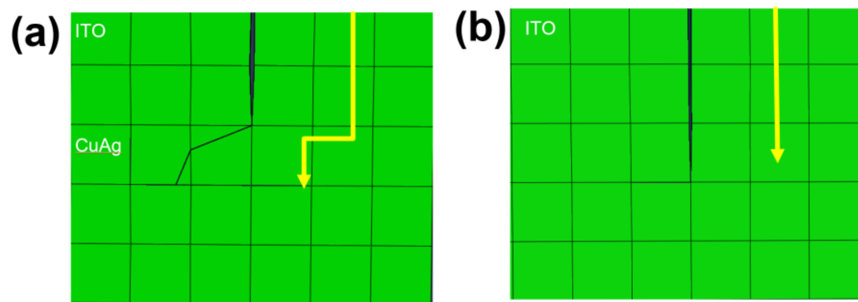

Figure 2.22. Comparison of simulation results of crack propagation direction of DMD and ITO layer at bending radius R=4mm. Yellow arrow indicate crack propagation direction.

We created an artificial 5nm-long crack in the top of the ITO layer. According to the simulation results, crack is propagated due to the brittleness of ITO structure and is arrested at CuAg layer at bending raidus 6mm ($\varepsilon = 0.83\%$). When we decreased the bending radius and increased the bending strain close to 5mm ($\varepsilon = 1\%$), the crack deflected along with CuAg layer. Furthermore, at bending raidus 4mm ($\varepsilon = 1.25\%$), the deflected crack propagated into the bottom ITO layer and developed into the PET layer. As expected, when the critical crack length decreased, the required applied strain (ε) or stress (σ) increased, and vice versa.

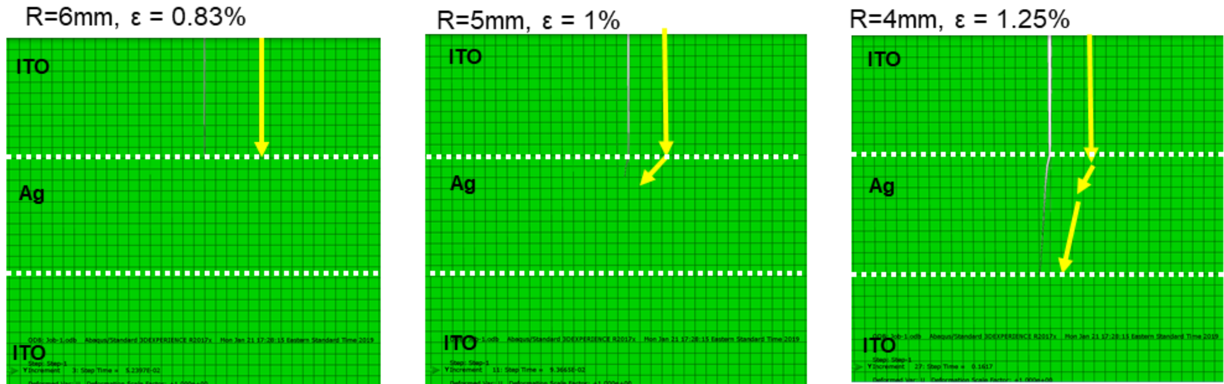

Figure 2.23. Simulation results of crack propagation direction of DMD layer.

The highly enhanced mechanical stability of a DMD film, in comparison to the pure ITO film, is a result of the sandwiched 10nm-thick metallic layer. It exhibits high resistance to cracking. The improved crack resistance can be explained by the effective elastic mismatch between ITO and CuAg layer, which successfully alleviate bending stress. FEA simulation can be conducted in order to clarify the effect of CuAg buffer layer and the mechanical stability of an ITO film will be improved.

Stress Distributions Throughout the Cross Section During Bending

In addition to the crack deflection and penetration competition described above, the shear deformation of metallic layer introduced in this study can also further improve the electrode robustness and durability. Strain level is decreased because of shear deformation of thin metal layer.

In metal layer, bond rupture plays an important role in resisting crack growth, because fracture energy is highly associated with plastic deformation near the crack tip. In addition, the transverse sectional plane of the metal layer largely deformed which resulted in transferring of

the bending stress to the shear stress. As demonstrated in Figure 2.24, even though these structures—the DMD and the pure ITO—have identical thickness, the properties of the strain levels differed significantly. When the structure with pure ITO structure was subject to bending, a single neutral plane was generated. The plane cross section for the entire stack remained planar and it had a single neutral plane after deformation. In contrast, as depicted in Figure 2.24 (c), the multiple neutral planes approach was applied by inserting a ductile metallic layer in between the stiff ITO layers, and the ITO layers bent independently during bending are not coupled rigidly because the transverse sectional plane of the metallic layer largely deformed. As a result, the ITO layers bent with their own neutral plane and multiple neutral planes appeared in the multilayer stackup. This indicates that the multiple neutral planes could be controlled by inserting the metallic layer. It benefits the transfer of strain energy to the middle layer such that the bending strains in the outer layers diminish. In another words, the maximum bending strain could be reduced with increased compliance of the structure. Again, inserting the metallic layer will be beneficial when mitigating the outer layer strain, and creating multiple neutral planes will enable mechanically flexible structures even under at small bending radius (R=5mm).

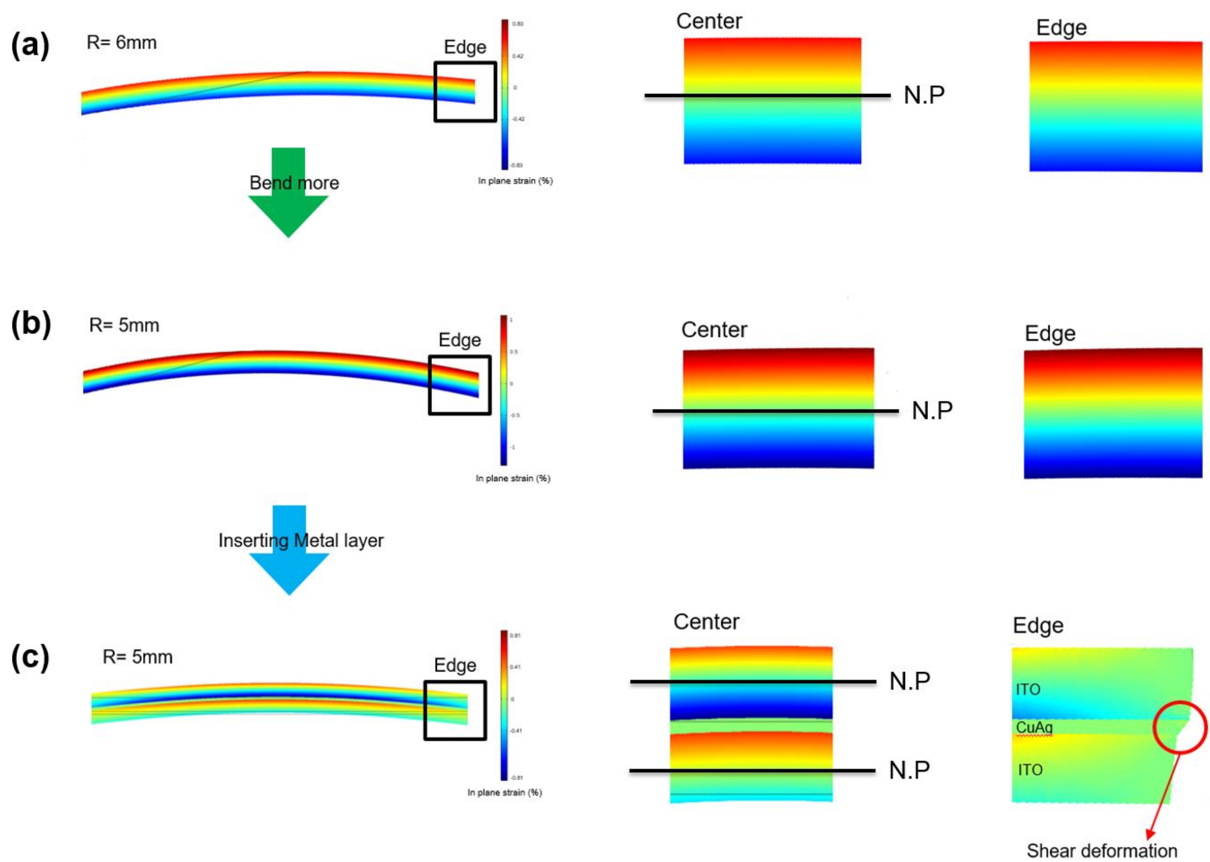

Figure 2.24. FEA results compare between the multilayer structure with specific metallic layers, and pure ITO structures when subjected to bending. (a) Pure ITO structure under bending radius R=6mm, (b) Pure ITO structure under bending radius, R=5mm. Strain level was increased due to the conventional beam bending theory (0.53% to 1%). (c) However, if we insert metal layer in between, strain level is decreased compared to pure ITO case. At bending radius, R=5mm, strain level of outer layer is 0.82%.

Interfacial Failure Between DMD and PET Structures

Recently, flexible electronics with delicate integration of stiff electronic films on soft substrate have attracted much attention, but it is vital to understand the interfacial failure in a multilayer stackup first. Because of a large mismatch of mechanical properties between the PET substrate and stiff DMD films, interfacial failures have always been a dangerous factor and a concern [32, 33].

When the bending strain is large enough to break thin film layers on the electrode, dislocations in the metal film can come out. On further straining, the film does not harden as much as its bulk counterpart. Consequently, once the film thickness decreases at a particular local spot by forming a neck, further deformation is localized in the neck and this leads to rapid rupture. While the local elongation is accommodated for the freestanding thin film by the ruptured halves moving apart, it cannot be well accommodated for a metal film bonded to a substrate. This constraint of the substrate retards strain localization, so that the metal film can deform uniformly to a large strain. The ductility of a thin film depends on its adhesion to the substrate. A well bonded thin film structure carries the film to large tensile strains without rupture by delocalizing deformation in the film. A poorly bonded substrate allows the film to form channel cracks at relatively small macroscopic strains by facilitating the coevolution of strain localization and delamination. Therefore, strongly bonded multilayered structure is necessary to produce highly robust flexible electrode.

The interfacial fracture toughness—the mechanical energy per unit interfacial area at which fracture occurs—was measured by the adhesion strength between each layer interface. In the case of DMD multilayer, cracks propagated rapidly through the top ITO layer and quickly extended to large distances in a direction perpendicular to the applied strain as soon as they

formed in the outer ITO layer. At PET layer, the crack also propagated along the ITO/PET interface (i.e. delamination), aggravating the failure process. With additional strain, new cracks formed and its spacing decreased until a saturation spacing was reached. And with continued strain, transverse cracking and delamination of the fragments also occurred. In Figure 2.25 (c), a strained DMD film on PET illustrates the microscopic appearance of several of these cracking and delamination phenomena at bending radius R=1mm. The mismatching mechanical properties of ITO and substrate also create considerably high potential device failure by delamination. Under certain bending strain, mismatching properties lead to stresses that act directly on the interface. And under weak adhesion, delamination will easily occur. Delamination or interfacial slip may occur at any interface in the electrode where the adhesion is poor and when cohesive failure has been observed. Cohesive failure means that the internal cracks on the plane of the film are responsible for delamination. When a thin film on a substrate is stretched, the film may rupture at a few percent to a few tens of percent strain. This huge variation in the ductility of the thin film is modulated by the adhesion of the thin film and polymer substrate interfacial strength.

Based on our experimental results, the delamination is of particular significance in the ITO on polymer system when subjected to severe bending (R=1mm). The ITO and polymer interface mainly consists of physical bonds, such as van der Waals bonds. Under special treatment during film deposition, chemical bonds can form at the ITO and polymer interface. However, under a severe bending stress, the ITO and the polymer system cannot endure the elongation solely by increasing atomic or molecular space. Consequently, certain amount of thin film atoms and polymer molecules form new bonds and generate extra interface. These new bonds between ITO and polymer system are likely to be mostly physical bonds.

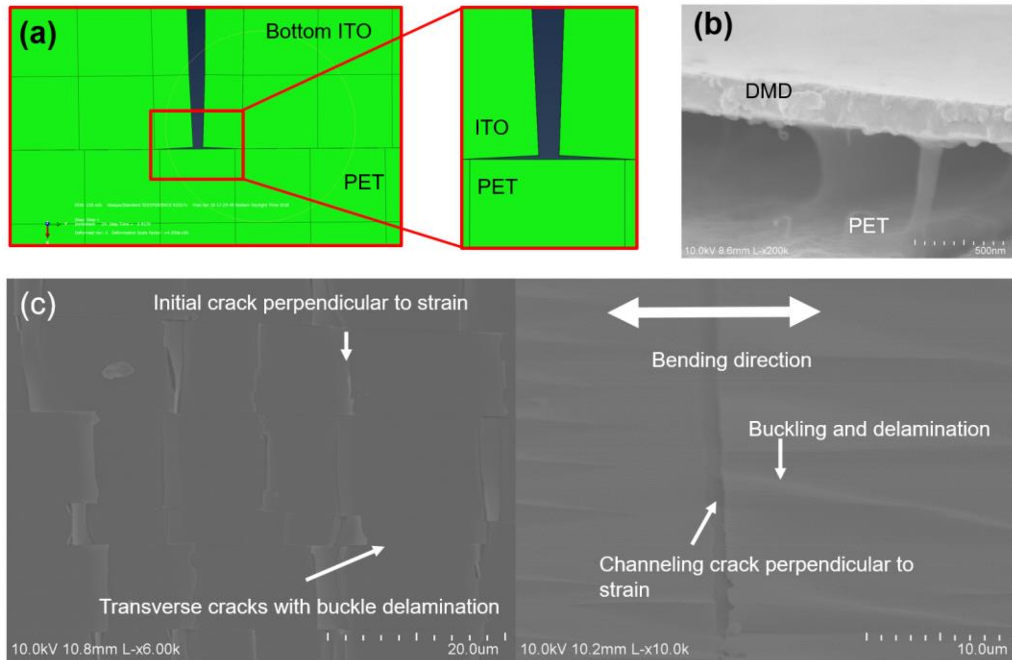

Figure 2.25. Debonding failure occurs between PET and ITO interlayer. (a) FEA simulation results of interfacial failure between ITO and PET layer. When crack impinging on a bi-material interface, and it will penetrate through the interface as well as the bottom ITO layer or deflect along with metal layer. Due to the low adhesion energy 0.1 $J{\cdot}m^{-2}$ between ITO and PET layer, then delamination failure will be happened along with ITO/PET interface under severe bending stress.

Conclusion

In summary, we investigated a unique crack deflecting effect and the resulting fracture toughness of thin film materials by using thin metallic layer as our representative material. Ductile brittle combination strategy provided us with both increased transmittance and toughness of a thin metal film. This structural material, although constructed using an intrinsically brittle ITO constituent, showed highly elastic and superior fracture resistance. CuAg thin metal layer is ductile compared to ITO layer, and it played a crucial role because it makes the crack propagation more difficult. Experimental and numerical modeling results indicated that the thin metallic layer deposition between ITO layers can partially absorb the bending deformation energy by shear deformation of metal layer. Thus, the thin metallic layer in between can be a

promising candidate for non-ITO conductive materials for modifying and improving the crack resistance mechanical properties. The enhanced fracture resistance performance of the current DMD multilayer is another great evidence. We successfully investigated the crack deflection of DMD layer and thoroughly reviewed the results both numerically and analytically. The method and analysis we presented on fracture toughness and crack prediction can open up new paths for evaluating future optoelectronic devices.

This chapter discussed mechanical explanations of the root causes of premature transparent conductive electrode failure during bending. We demonstrated how metallic layer changes the crack direction and explained ways in which a change in mechanical properties can improve the electrode fracture resistance. In addition, we presented failure analysis, which may serve as a guideline to the optimization of future conductive electrode material development to increase the material ductility and suppress the high surface stress. Our results certainly inspire ideas and suggests potential strategies for overcoming the relatively low fracture toughness of brittle materials through hierarchical brittle ductile hybrid multilayer.

CHAPTER III

Fatigue of Flexible Electrode

Introduction

Repeated deformation and cumulative mechanical stress due to cyclic bending and folding operations present significant reliability issues. Continuous and cumulative mechanical damage on the flexible electronics is directly related to the performance of the device. Multiple cracks will eventually degrade its optoelectronic performance and function. Conventional electronic devices have been designed and produced mostly on the basis of mechanically static operations like no repeated back and forth movements and impacts. In the past, studies on flexible devices focused mainly on materials development to improve their functionality and flexibility under static bending [41]. To test reliability issues, they only performed bending tests such as fixed bending radius and constant bending speed, and demonstrated the flexibility of flexible electronic devices without a thorough mechanical investigation. In these days, researchers and many companies strive to develop robust flexible electronics, but there is no deep understanding of fatigue failure of electrodes. Some recent studies show various test methodologies and discusses operational limitations of flexible electronics, but there are still no clear direction on how to assess fatigue damage and a guideline for fatigue failure evaluation.

In order to design highly reliable flexible devices, comprehensive studies must be carried out to understand the effects of various mechanical deformations. Fatigue failure occurs when small deformations are repeatedly applied well below the fracture strain level, and this is a major issue closely related to a long-term reliability.

Bending Test Setup and Strain Rate Calculation

In a typical bending process, the two sides of a bent sheet experience different types of strain. Tensile strain is present on the convex side, while the concave side experiences compressive strain.

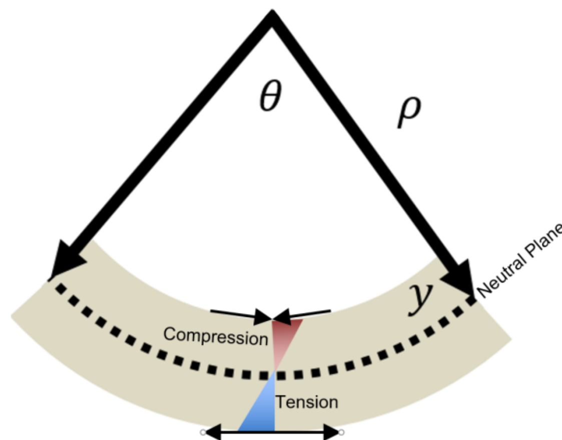

Figure 3.1 Schematic illustration of multilayer. Linear elastic deformation is governed by Euler and Bernoulli equation, which states inner layer has compressive stress whereas outer layer has tensile stress when subjected to bending. In the middle layer (black dashed line), there is a neutral plane.

These strain states (shown in Figure. 3.1) may lead to different failure modes. Cracking of a film or channeling crack will occur when tensile stresses develop; buckling-driven delamination can occur if stresses are compressive. Interfaces are intrinsic to these systems, and

they are susceptible to interface debonding or delamination. Isolated surface cracks can propagate and channel across the film. If the substrate is brittle, the crack may penetrate into the substrate even though it is essentially unstressed. The interface may debond, or a debond crack may dive into the substrate producing delamination through cracking, parallel to the interface in the substrate. Combined film cracking and interface debonding can also take place if the combination of film toughness and interface toughness lies within certain limits [43].

In a homogeneous structure, these peak strains can be calculated using a simple equation, ($\varepsilon = t / R$), or with more accurate formulae that invoke fewer simplifying assumptions. From these expressions, it is easy to note that thinner substrates experience lower strain at a given bending radius, and thus components mounted on these thinner substrates tend to tolerate smaller bending radii before failing. Moreover, through the bulk of a bent substrate, the strain varies between the compressive and tensile extremes on either surface. The variation is linear in a homogeneous film and it may be more complex in a layered structure, but regardless, a mechanically neutral plane exists in the sample where neither tensile nor compressive strain is present. Positioning fragile materials along this neutral plane maximizes the overall flexibility of the system.

We created a folding plate test setup to evaluate fatigue behavior under cyclic operation. The electrical resistance can be measured in real time using Keithley 196 multimeter combined with Labview program. The sample is located at the center and is set to repeatedly fold and flatten over time. The electrical properties are measured in real time with various strain rates.

Based on conventional beam theory, strain rates are easily calculated by travel time measurement:

$$\Delta\varepsilon = \varepsilon_f - \varepsilon_0, and\ \dot{\varepsilon} = \frac{\Delta\varepsilon}{Time} = Strain\ rate \tag{3.1}$$

In our bending system setup, the strain difference ($\Delta\varepsilon$) was 0.375% at the bending radius R=5mm, and the travel time varied from 0.2 s to 20 s. Therefore, we calculated the strain rate range from 0.01%/s to 2%. As a part of fatigue evaluation, we applied different strain rates within this range to see how it affects electrodes over time.

While one time bending as a function of radius exhibits slightly improved optoelectronic performance, the performance of DMD structures after multiple cycles of bending showed more improvement in dramatic fatigue resistance than ITO sample. The resistance data for samples bent to a radius of 5mm as a function of the number of cycles are shown in Figure 3.2. It shows the resistance R as a ratio with the starting value R_0. It is evident that all samples with DMD multilayer showed dramatic improvements in cycling performance. Specifically, the value of $\Delta R/R_0$ for the ITO sample failed completely after few cycles while the values remained very stable even after 10,000 cycles for the DMD multilayer. This phenomenal response suggests that the ductility of the CuAg layer provides effective electrical conductivity even after the ITO was beyond its failure strains. They show excellent performance in conductivity and bending. DMD multilayer also provided significantly reduced sheet resistance in comparison to ITO, and showed improvements in bending properties. The use of DMD structures as a transparent conductor in flexible electronics is very promising.

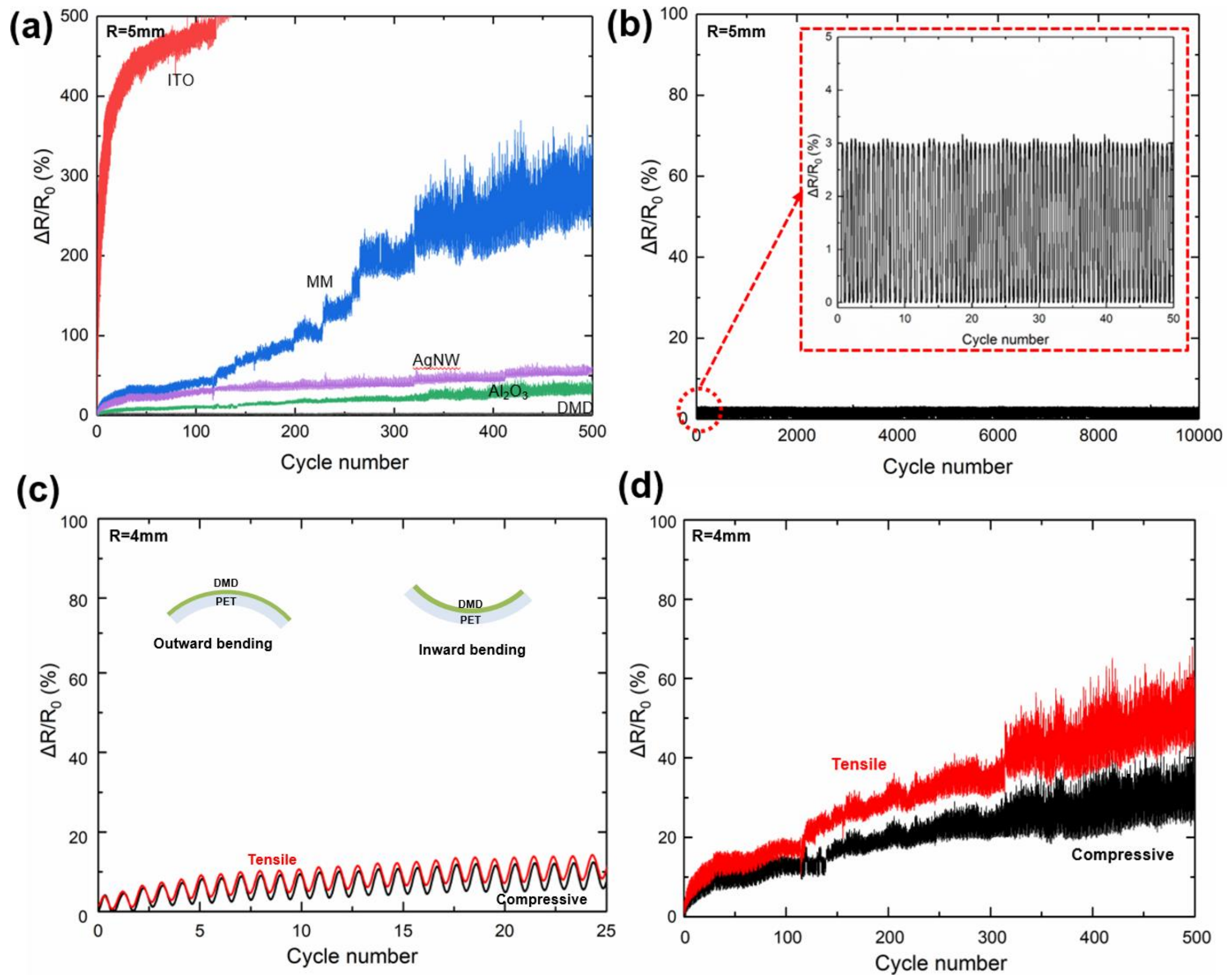

Figure 3.2. It shows the dynamic outer bending fatigue test results of the optimized DMD multilayer with increasing bending cycles at a fixed outer bending radius of 5 mm. (a) Comparison of flexible electrode cyclic performance results (b) DMD multilayered structure resistance versus repeated oscillating bending events (at R=5 mm radius). Inset: a zoomed-in fragment of the main curve showing perfectly repeatable and stable sheet resistance oscillations, DMD exhibits very stable resistance value even after over ten thousand bending cycle number. (c, d) Fatigue comparison results between tensile and compressive at bending radius 4mm. Compression shows better cyclic performance compared to that of tensile stress case.

Figure 3.2 (c, d) shows the change in resistance in response to inward (compressive stress) or outward (tensile stress) bending as a function of the cycle number at bending radius 4mm. Inward bending refers to the case where the electrodes are placed on the underside of the substrate. Tensile stress is generally associated with film cracking whereas compressive stresses result in buckling or wrinkling of thin films over compliant substrates. Based on fatigue experiments, DMD films on the flexible PET substrate exhibit substantial differences in the

value of $\Delta R/R_0$ between the inward and outward bending. Specifically, tensile stress promotes early failure. This inconsistency is fully attributed to different fracture mechanisms. Under the tensile strain generated in the outward bending test, as schematically illustrated in Figure 3.3 (a), is fractured by directly causing film rupture and forming channel cracks. While under compressive strain induced by inward bending (see Figure 3.3 (b)), the film may first delaminate from the PET substrate and then buckle before the crack initiates. The applied strain energy was released through the formation of delamination, buckling and cracks in the inward bending test. The failure mechanism of the DMD film under tensile strain is directly related to cracking resulting in rapid electrical disconnect, while that of the DMD film under compressive strain experiences delamination, channel cracking sequentially, resulting in delayed failure.

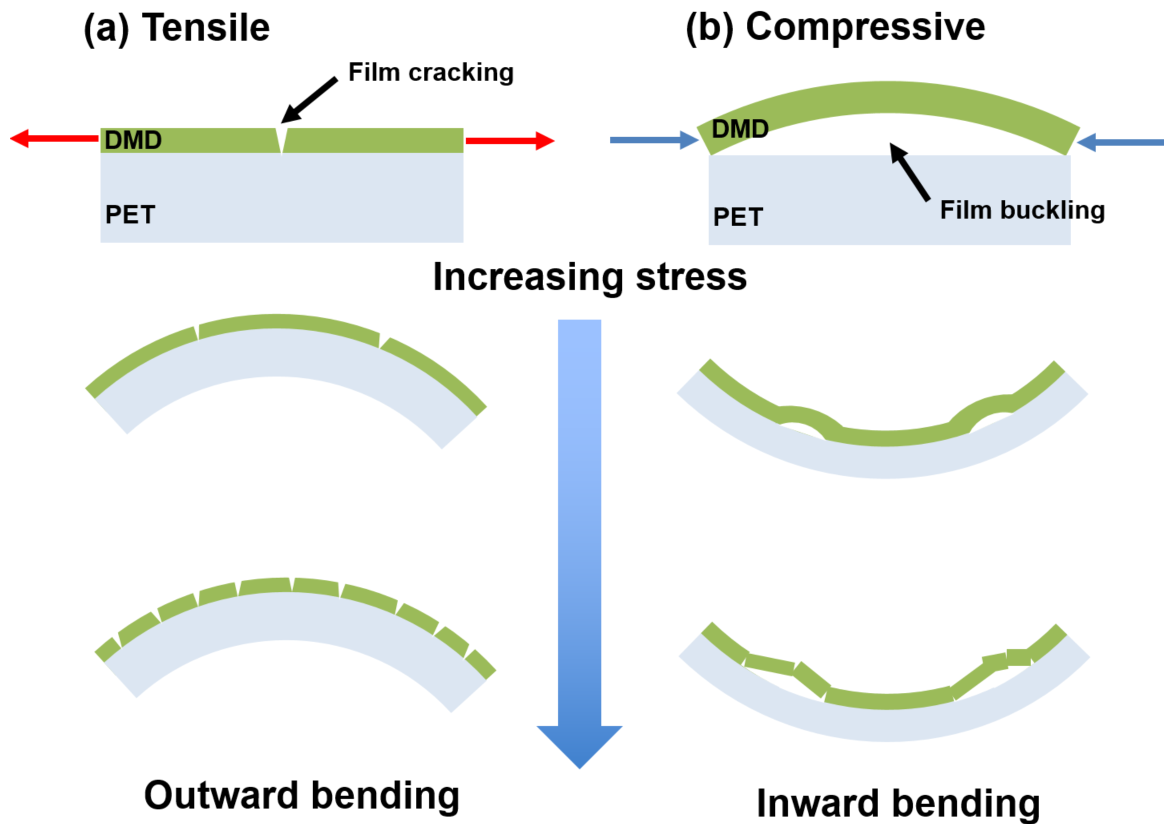

Figure 3.3. Schematic illustration of failure mechanisms of the DMD film subjected to (a) outward bending and (b) inward bending. (a) Cracks induced by tensile stress causing rupture of the DMD film. Figure (b) illustrates the formation of buckles due to mitigation of in-plane compressive stress when subjected to inward bending.

Comparison of Cyclic Performance Results

Durability and failure investigations of electrodes are of high interest when determining the risk of failure in engineering applications. ITO remains the mainstream transparent conductive electrode and it is widely used on transparent conductors for many conventional electronic components, such as touch panels and displays. This fully mature technology will likely dominate the electronic sector for many more years. But it also comes with some well-known drawbacks like brittleness and low fatigue resistance. Many researchers tried to overcome these mechanical issues and develop a wide range of ITO-replacements [10, 14], for example, metal mesh, silver nanowire (AgNW) [10], graphene, carbon nanotube (CNT), conductive polymer, graphene and other transparent conductor technologies [32]. Each transparent conductive material has its own strengths and weaknesses, and there are many parameters to consider when choosing one [33]. Sheet resistance, transmittance, haze, optical clearance, and cost are among that list. ITO-replacements could provide higher optoelectronic value as well as enhanced mechanical performance. Various emerging materials have been reported as transparent conductive electrodes in optoelectronic devices, though not all of them show better properties than ITO.

Conductive transparent polymers have emerged as low-cost electrodes over the last 10 years due to its solution compatibility and large-scale processibility, but it suffers from poor electrical properties and environmental stability. Nanomaterials, such as CNTs, graphenes, and metal nanowires, have emerged as an attractive non-ITO transparent conductive electrode materials. Although CNTs and graphenes have been studied extensively, they are still far away from commercial applications as transparent conductive electrodes because of their low film conductivities and limited large-scale process techniques. Metal nanowire is another top

candidate with its promising optoelectronic properties and good compatibility with most solution-based processes even though several issues remain to be solved. The high surface roughness and poor electrical and environmental stability impede their application in devices with ultrathin layers. Moreover, some metal nanowire, especially, AgNW or CuNW can be corroded through chemical reactions, like oxidation, which also causes the degradation of metal NWs and their related devices [10].

The long-term reliability of various non-ITO conductors during bending fatigue was investigated, as shown in Figure 3.2. As previously described, the electrical resistance of an electrode increases from fatigue damage formation during cyclic bending deformations, except for DMD multilayer. To determine the effect of repeated bending of each transparent conductive electrode, strain rate of 0.1%/s was applied. The durability of the flexibility of the coatings according to the number of bending cycles was investigated by measuring $(R - R_0)/R_0$. The experimental results showed that material selection significantly affected the performance of the flexible conductive electrode. Our candidates included: ITO, metal mesh, AgNW, DMD with ITO/CuAg/ITO structure, and DMD with Al_2O_3/CuAg/Al_2O_3.

Each electrode exhibited different electromechanical trends during the cyclic bending process. Again, DMD materials showed marked flexibility in recoverability and reproducibility. They showed perfectly repeating and stable sheet resistance oscillations after over ten thousand bending cycles. And it continued to show outstanding results with no fatigue degradation. This flexibility can be attributed to the highly ductile behavior of the metallic CuAg interlayer between the ITO layers. In Figure 3.2 (b)), clearly very stable repeated oscillations was observed. This oscillation ($\Delta R/R_0 = 3\%$) is slightly higher than mechanical strain (1%) and this result can be explained by piezoresistive effect. The piezoresistive effect is a change in the electrical

resistivity of a metal when mechanical strain is applied. The piezoresistive effect causes a change in electrical resistance [53]. Gauge factor (GF) is the ratio of relative change in electrical resistance *R*, to the mechanical strain ε. It determines the amplification factor between strain and resistance change. The gauge factor is defined as:

$$G = \frac{\Delta R/R_0 \ (Resistance\ change)}{\Delta l/l \ (strain)} \tag{3.2}$$

In general, Gauge factor for metal is about 2-5 [54, 55]. According to the cyclic bending test results, $\Delta R/R_0$ is 3% and strain is 1%. So our gauge factor is approximately 3.

It is apparent that the degree of electrical resistance gets higher when the degree of micro-cracks increases, and $\Delta R/R_0$ gets higher when bending curvature decreases or fatigue cycles increase. The fatigue response for AgNW, metal grid, and DMD with Al_2O_3/CuAg/Al_2O_3 are found to be significantly worse than that of the DMD structure. The failure behavior under cyclic bending-mode deformations can be explained in various terms. In case of AgNW, orientation, diameter, length, concentration, and adhesion between nanowires and substrate are critical issues. The change in resistance of the electrodes on substrate under bending strain is closely related to the failure of nanowires. It indicates that AgNWs on the substrate are randomly aligned to the bending direction. The maximum bending force is applied to the parallel direction of bending, and for tilted nanowires, the applied bending force can be simplified by a proportional cosine relationship between the nanowire orientation and bending direction.

Metal grid is also a promising candidate due to the superior optoelectronic property [11, 12], however it is prone to fatigue damage. It has network transparent conductive electrode, and as depicted in Figure 3.4, a detrimental impact on the operation of devices may occur through its

narrow conductive path. And stress will be concentrated in this narrow path during cycling loading, making it difficult to resist any necking of conductive line.

DMD with Al_2O_3/CuAg/Al_2O_3 multilayer resembles the original DMD architecture, but the elastic modulus of Al_2O_3 (200 GPa) is higher than that of ITO structure (150 GPa). This higher number results in an earlier failure than DMD multilayer.

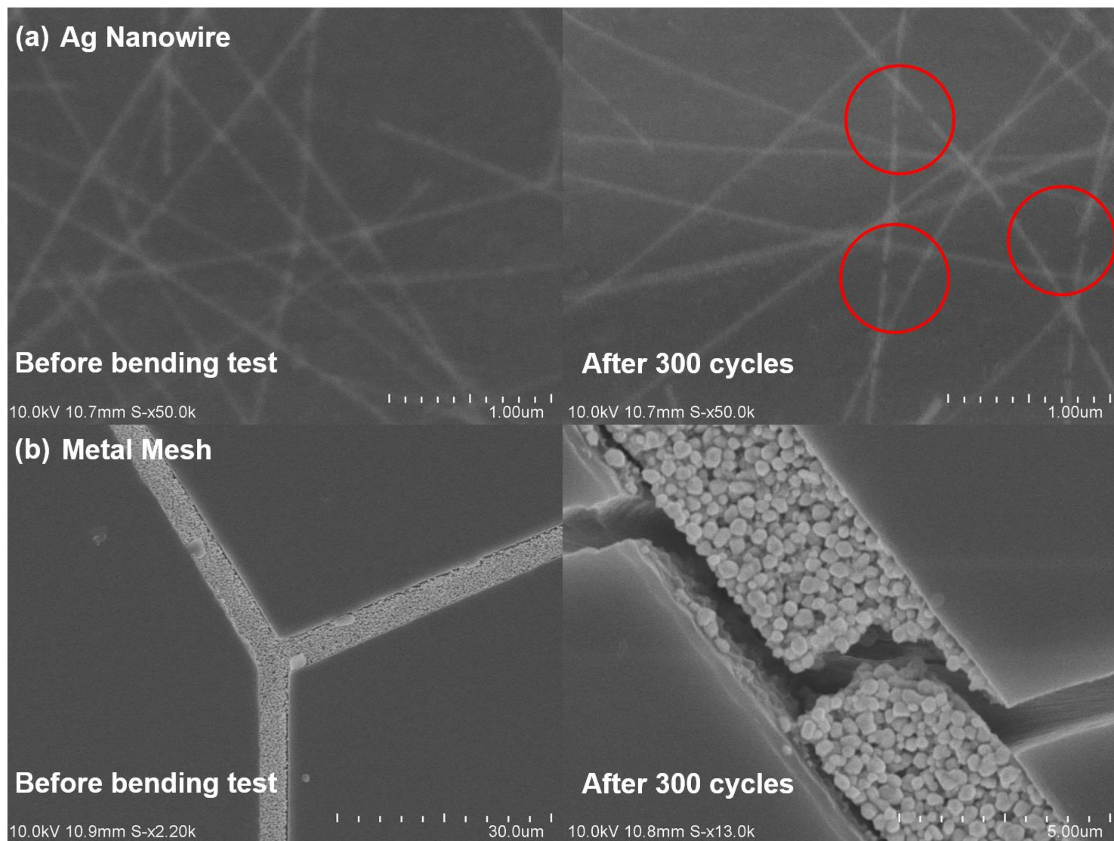

Figure 3.4. Based on our bending test results, (a) AgNW and (b) Metal mesh sample (with Ag nanoparticle) failed rapidly comparing to DMD sample. These promising electrode exhibits brittle fracture due to the localized necking, and leading to the abrupt increase of electrical resistance in flexible electrodes.

Effects of Strain Rate

If failure is considered as deterioration in desired performance, including facing limitations and inability to go back to the original state, then failure can occur by many different mechanisms.

In general, the response of electrodes during bending tests can be categorized into two ways: reversible (elastic deformation) or irreversible (plastic deformation and leading to failure). This response to the load could be immediate or could occur over a period of time. In some cases (creep and fatigue), the damage may accumulate over a period of time before electrodes fail. In elastic domain, the electrode recovers its original shape and performance even after the removal of applied load, thus we can claim that elastic deformation is reversible. However, in plastic domain, permanent deformation occurs in electrode and it is impossible to recover its shape after the load is removed, making it an irreversible process. We performed bending tests by controlling the bending speed (strain rate) and bending radius (strain), and our results showed a unique resistance behavior of strain rate dependence. The resistance response can be distinguished into two different regimes. When bending radius is higher than 5mm, it is a reversible process because the electrode deformed in elastic regime. However, when the bending radius was less than 4mm, the electrode experienced plastic deformation and resulted in fracture, so it becomes an irreversible process. At larger strain, plasticity may take over elastic deformation.

In elastic region—at bending radius 5mm or higher—all resistance curve reached an equilibrium state, although it showed time delay response due to the slow bending speed. Since the change in resistance was proportional to the strain, all results adhered to the conventional Euler–Bernoulli beam theory, ($\varepsilon = t / R$). Surprisingly though, when we further decreased the

bending radius to less than R=4mm and conducted the test again, there was a discrepancy in the resistance value after a certain time. It is a counter intuitive phenomenon because resistance is normally fully dependent on strain.

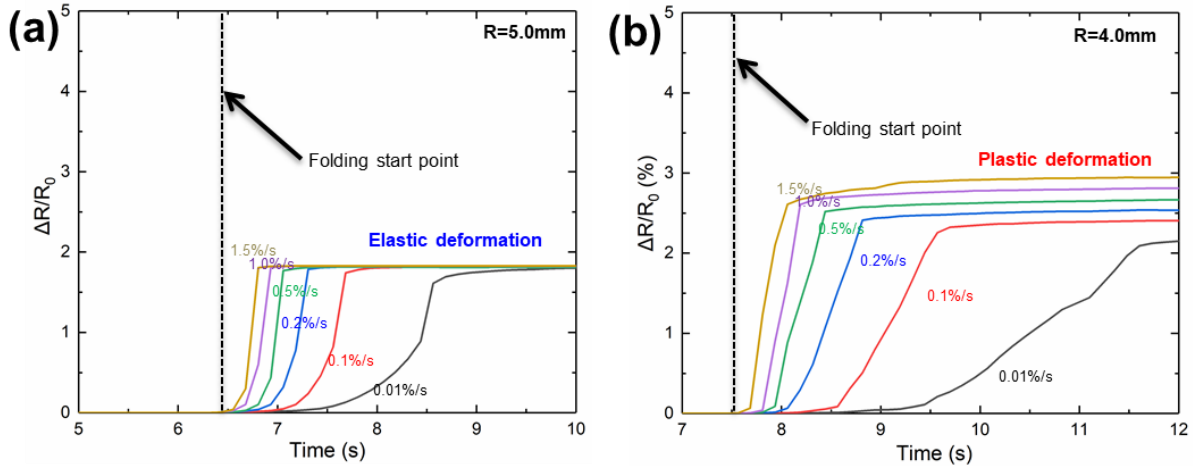

Figure 3.5. Comparison between (a) elastic (higher than R = 5mm) and (b) plastic deformation (less than R= 4mm). In elastic deformation, resistance is fully dependent on strain, however, in plastic deformation, resistance varies each other despite of applying same strain.

This result means that same strain does not provide same delta resistance value due to the different strain rate. Therefore, in plastic region, it does not follow the conventional beam theory ($\varepsilon \neq t / R$); the beam bending theory is not adequate to describe this phenomenon due to its unique dislocation behavior.

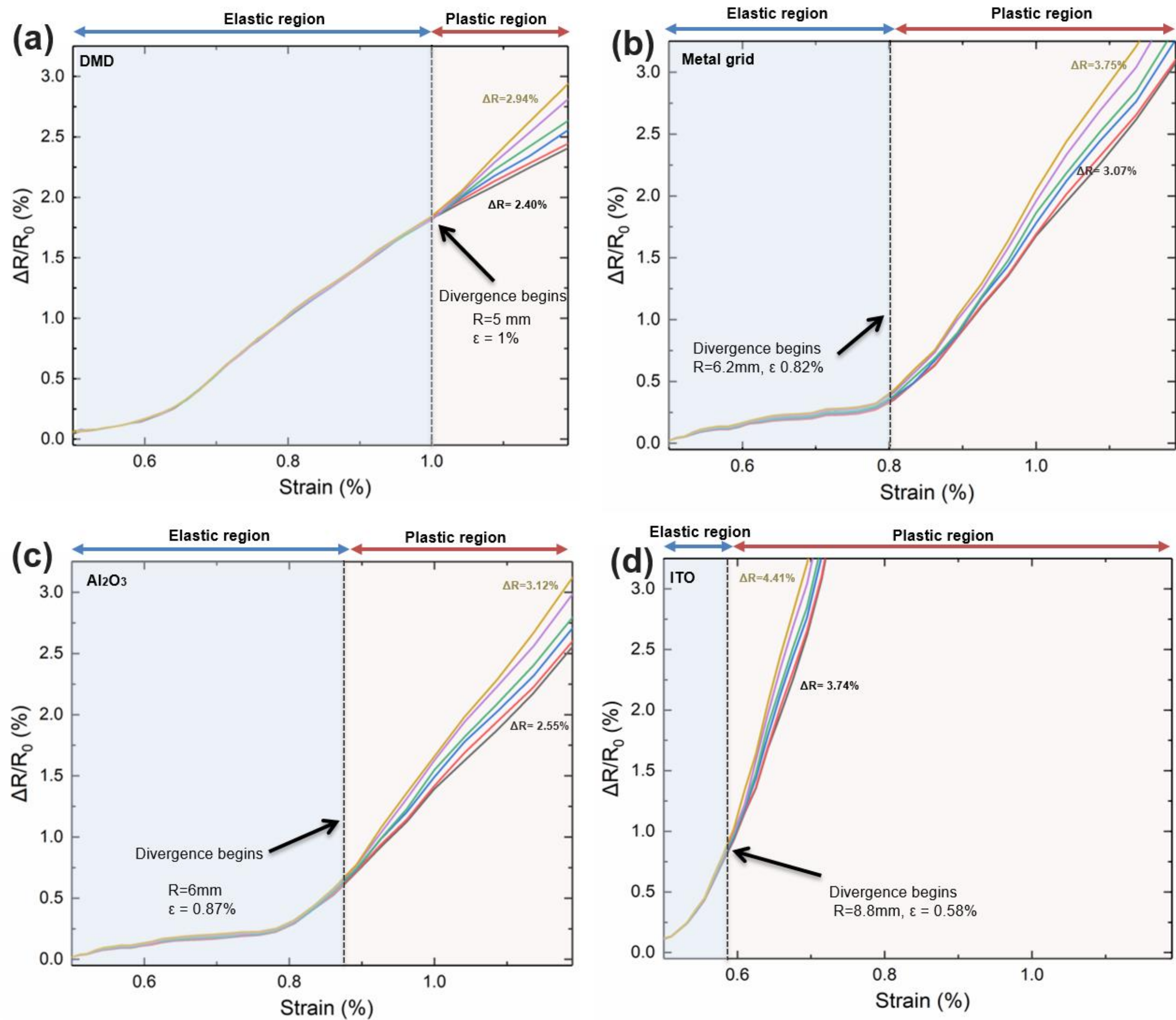

Figure 3.6. Several electrode's electrical performance parameters can be plotted against mechanical strain and strain rate. Interestingly, all electrodes exhibit hysteresis and begin to diverge after elastic deformation. The higher strain rate provide stiff increase of resistance. These materials are sensitive to the strain rate.

In plastic region, electrical resistance increases due to the increase in dislocation density. The dislocations in metallic layer from the local deformation leads to non-uniform deformation of the electrode. In Figure 3.6, a resistance variance graph have been plotted against mechanical properties (strain to failure). This is similar to other conductive electrodes, which show a ductile behavior in low strain rate and exhibit a brittle behavior under high strain rate. In fatigue test, as shown in Figure 3.7, DMD film showed better cycle performance in low strain rate with sheet

resistance of 10 Ω/sq after 300 cycles. In case of higher strain rate (1%/s), electrode failed earlier because resistance value reached more than 20 Ω/sq in plastic region at bending radius R=4mm. It is possible that the plastic deformation process may not have developed properly due to insufficient time given in higher strain rate. There was not enough time for thermal activation to be effective. The increase in the electrical resistance also implies that there was an increase in the scattering sources in electrodes (dislocation density), which was due to the local deformation. The non-uniform deformation of the metal may change the distribution of the electric current flowing through the metal. Also, it is important to note that deformation develops only locally until necking, resulting in a brittle-like fracture.

Lower strain rate allows more time to accomplish the course of destruction and reconstruction of conductive paths. There is enough time to reach an equilibrium state, and more allowed time permits thermally activated reactions to occur, which will lead to uniformly distributed deformation.

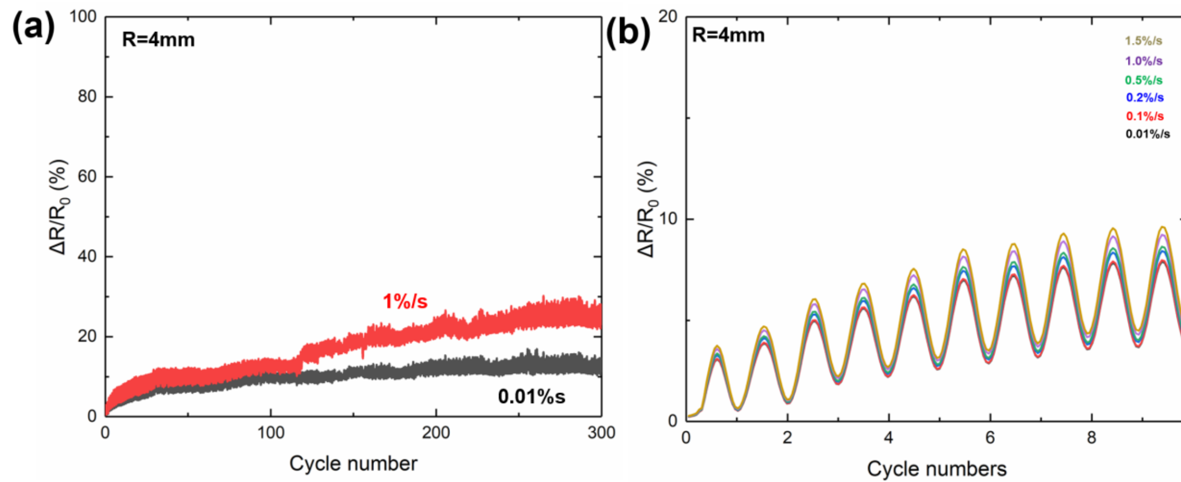

Figure 3.7. DMD resistance versus cycle number depending on the strain rate. In plastic region, at bending radius 4mm, DMD electrode fails earlier in case of higher strain rate. (b) If we look closely, depending on the strain rate, there is a hysteresis between each strain rate.

Ductile To Brittle Transitions

Just like how an ironsmith changes the shape of metal after heating it, we can easily deform metal with heat. At low temperatures, metal is brittle, but they become ductile at high temperatures. This can be explained by the fact that the atomic mobility can be assisted by thermal energy. A high mobility can be thermally activated to cross the potential barrier 'Q' to the neighboring metastable position [44]:

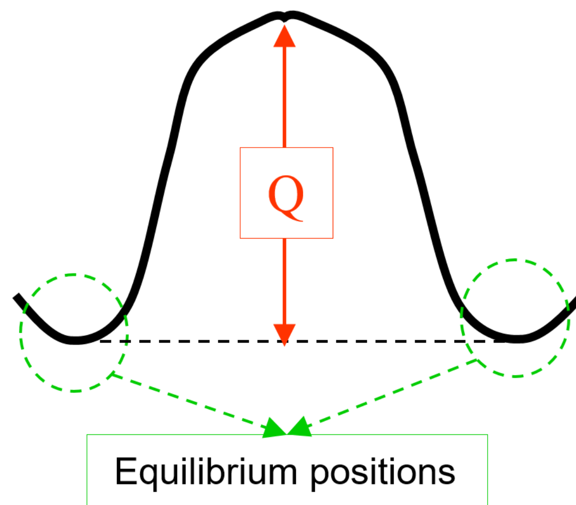

Figure 3.8. Thermally fluctuation enables to climb over the activation barrier to glide to the next valley.

This thermal activation reduces the yield stress, so materials which are brittle at room temperature may also become ductile at high temperatures. It is also known that high strain rate loading increases strength, but reduces ductility. Materials that are brittle at high strain rate may become ductile at low strain rate. Strength decreases and ductility increases when strain rate is decreased and temperature is increased [44].

Various experiments indicate that solids are brittle at very low temperatures, and their toughness become much higher at higher temperatures. Besides temperature, strain rate

influences the fracture toughness [47]. A faster strain rate will likely induce brittle fracture [48]. With other conditions fixed, a slower loading rate leads to ductile fracture [46, 47]. Ductile fracture is always a preferred mechanism, because it can prevent catastrophic failure, and it is important to study the ductile to brittle transition in order to understand the fracture process.

The resemblance between the effects of temperature and strain rate is not coincidental. Temperature supports the mobility of atoms to change their configurations; solids are more capable of accommodating a deformation field in higher mobility [41, 45]. The strain rate, alternatively, contributes to suppress the deformation process of the material. Their competition leads to the above-mentioned property of material toughness.

According to Eyring's equation (3.2), yield stress (σ_y) is proportional to strain rate and it is inversely proportional to temperature [44, 45]:

$$\sigma_y = \frac{R}{V}\left(\frac{\Delta U}{RT} + ln\frac{2\dot{\varepsilon}}{\dot{\varepsilon}_0}\right) \tag{3.2}$$

Higher strain will increase the yield stress and the material will become more brittle. Yield stress (σ_y) has a rapid increase with increasing strain rate. This phenomenon can also be verified by measuring elastic modulus with applying different tensile strain rates. As the strain rate increases, the elastic modulus increases accordingly. As shown in Figure 3.9, Young's modulus is 120.14 GPa at the high strain rate (1.0%/s) when it is 82.18 GPa at the low strain rate (0.01%/s).

Ductility can be defined as the ability to undergo significant plastic deformation before fracture, but it can also be expressed as elongation ratio or the area under the stress strain curve. Ductility can be quantified by the failure strain, which is the engineering strain at which a test

specimen fractures during tensile test. Our experiments proved that higher strain rate produces higher elastic modulus. The loss in plasticity as the strain rate increased also indicated that structural mechanisms promoting inelastic deformation change with the strain rate. Lastly, there was a decrease in failure strain (from 18.5% to 14.9%) as the strain rate increased, once again implying that the material strengthens as the strain rate increases, making it more brittle.

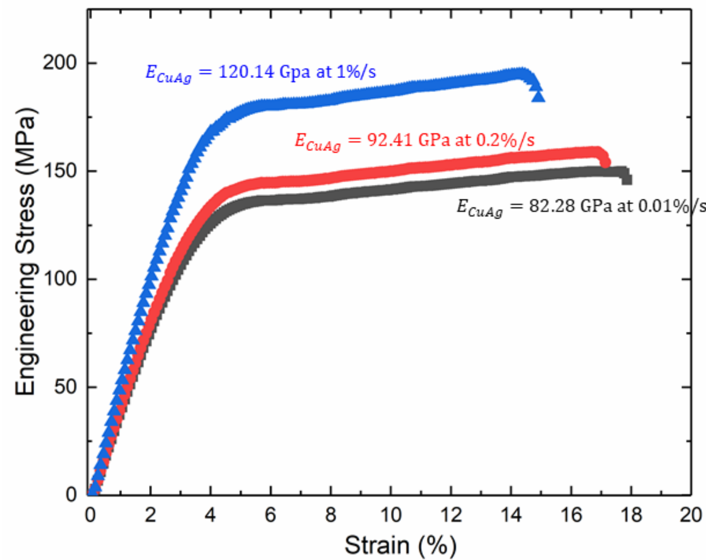

Figure 3.9. Depending on the strain rate, elastic modulus is changed accordingly. At the high strain rate (1.0%/s), Young's modulus shows 120.14 GPa, whereas at the low strain rate (0.01%/s), it shows moderate elastic modulus 82.28 GPa.

Crack Deflection and Penetration Competition Due to the Strain Rate

As discussed in the previous chapter, crack impinging from normal direction may advance by either penetrating through the interface or deflecting into the interface. The energy release rate for the deflected crack is compared to the maximum energy release rate for a penetrating crack. The results can be used to determine the range of interface toughness. We verified that the strain rate plays an important role in determining crack deflection or penetration.

As shown in Figure 3.10, we can see that there is penetrated crack even with the addition of a ductile middle layer when the strain rate of bending setup is increased (0.01%/s to 1%/s). This is because CuAg layer becomes brittle when the strain becomes too high. At a high strain rate, elastic modulus of CuAg layer (120 GPa) is close to that of ITO layer (150 GPa).

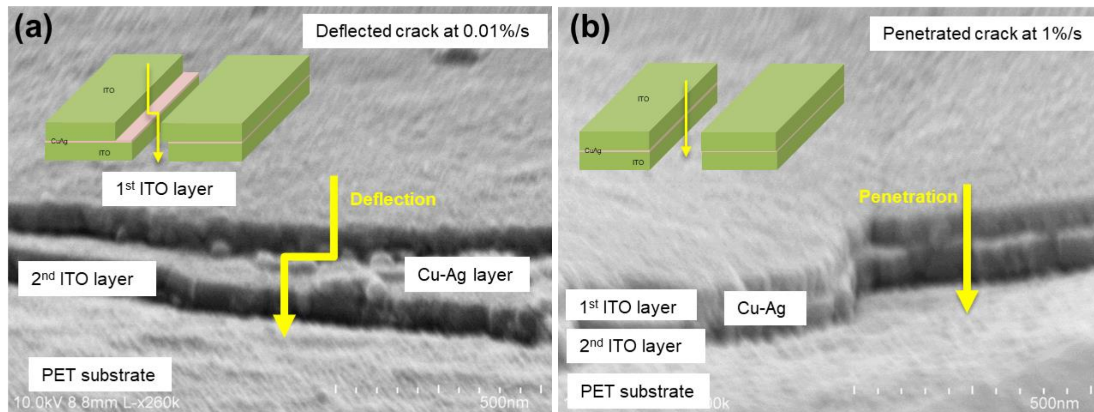

Figure 3.10. SEM images of (a) deflected crack at low strain rate (0.01%/s) (b) penetrated crack at high strain rate (1%/s).

The elastic modulus of metallic layer changes depending on the strain rate. The curve mark in Figure 3.11 explains the relationship between systems where cracks are likely to penetrate the interface at a higher speed (at 1.0%/s, above the curve, blue square dot) or deflect at the CuAg interface (at 0.01%/s below the curve, red square dot). At a low strain rate, plastic deformation will occur across the sample, and this will result in significantly decelerating crack growth while enhancing the fracture resistance, just as we've seen in the step-like crack phenomenon. We believe that these findings will suggest clear direction about ways to evaluate fatigue damage over the long cycle since different strain rates will yield significantly opposing crack formation.

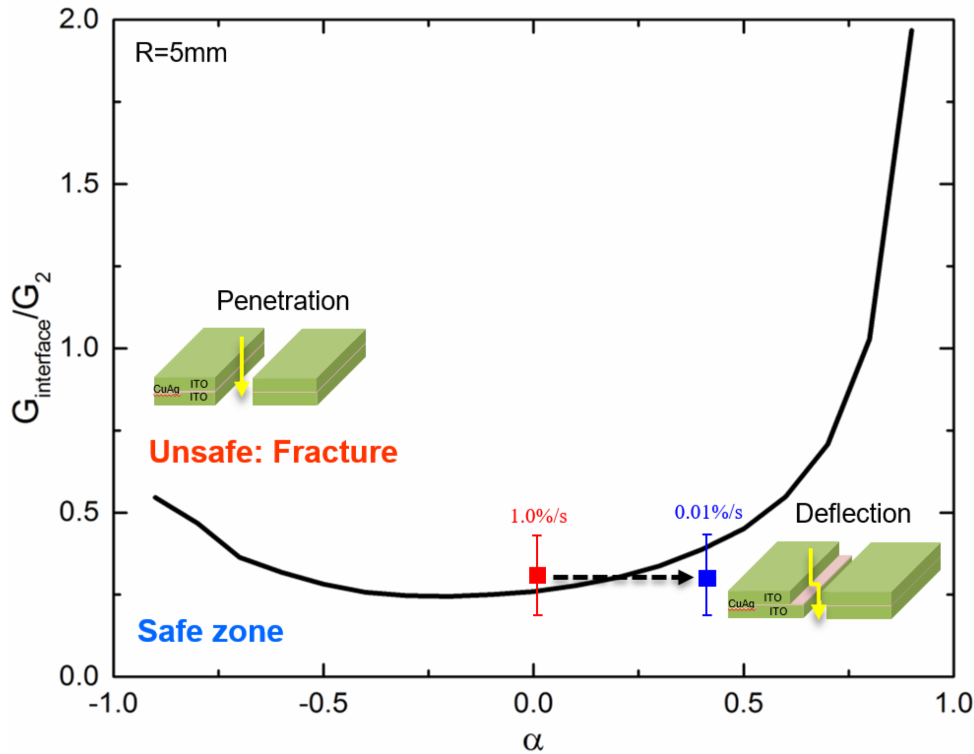

Figure 3.11. Mechanics solution by He and Hutchinson's approach. The curve marks the boundary between systems in which cracks are likely to penetrate the interface (above the curve, red square dot, at high speed) or deflect along the CuAg interface (below the curve, blue square dot) at low strain rate.

We examined a total of one hundred impinging cracks for statistical analysis (Figure 3.12). We found that more than 83.6% of the cracks actually deflected along with the CuAg layer and less than 16.4% of the cracks penetrated into the bottom ITO layer at a low strain rate. Even though the strain rate was low, there were still penetrated cracks, and we reason that this is because the energy may not have transported uniformly through the entire sample and also due to its close proximity to the curve. In contrary, most cracks were penetrated without any deflection at a high strain rate. All of these findings, once again, make He and Hutchinson's approach valid.

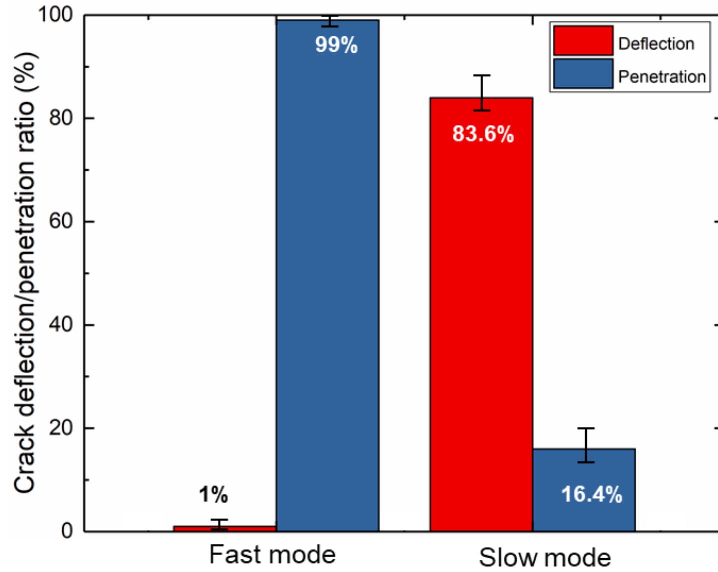

Figure 3.12. Statistical analysis of crack deflection and penetration in DMD multilayer structure.

Interestingly, fracture and fatigue step-like failure is also observed in a low strain rate. As shown in Figure 3.13, the metallic layer dissipates strain energy through plastic deformation, thereby significantly decelerating the crack growth in fracture, as well as fatigue.

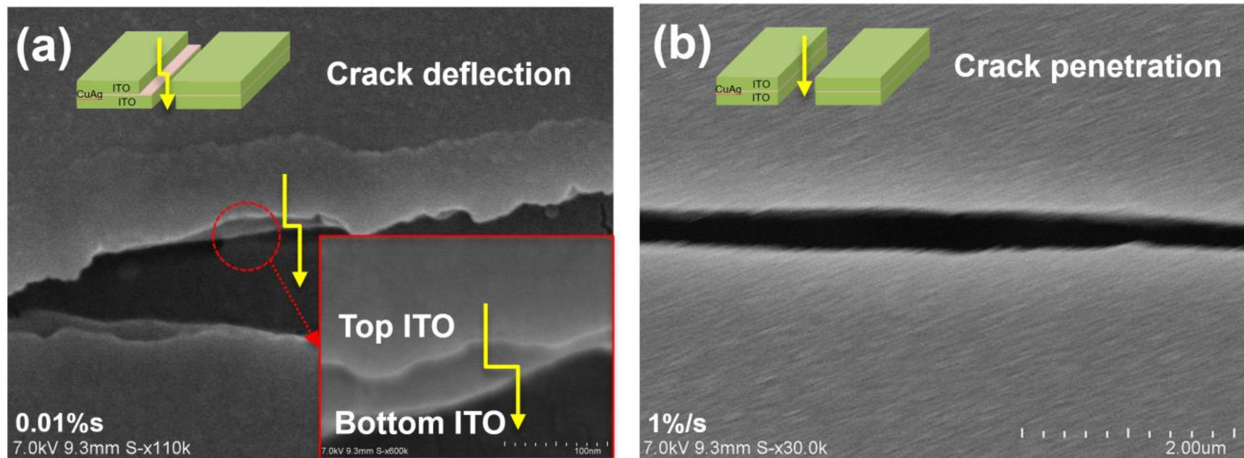

Figure 3.13. Top view of SEM image of DMD sample after 100 cycles at R = 4mm. It can be clearly seen that outer bending for 100 cycles in plastic region lead to the formation of cracks normal to the bending direction. In low strain rate, deflected crack was still observed, while in high strain rate, penetrated crack was detected.

In fatigue loading, the accumulation of slips between planes create uneven and rough surfaces. And even more, oscillatory loading leads to extrusions and intrusions of surfaces. Points of extrusions and intrusions play a crucial role because stress can be concentrated at these spots and they could serve as a stress amplifier to induce a full blown crack.

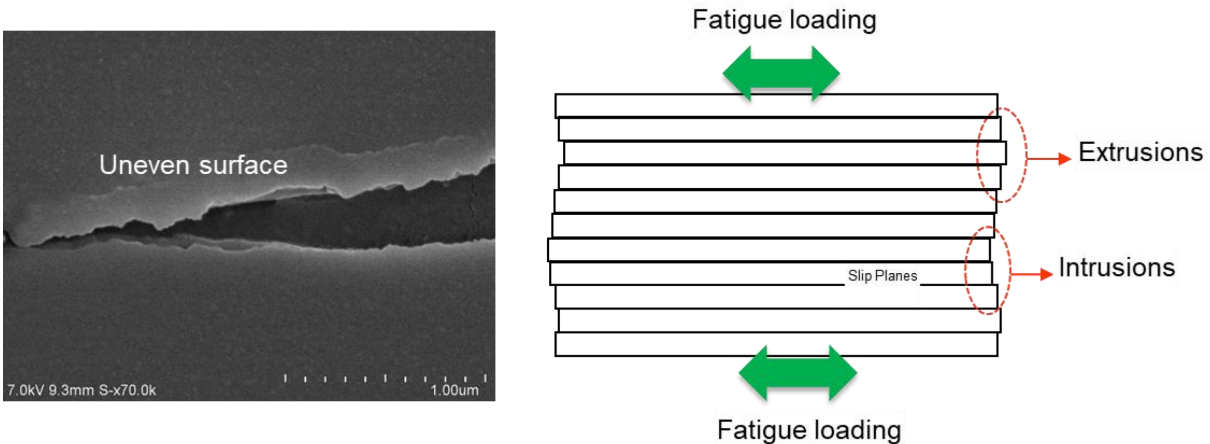

Figure 3.14. Uneven surface was created due to the fatigue loading. The accumulation of slips between planes create uneven and rough surfaces.

Conclusion

In this chapter, we thoroughly investigated fatigue failure during cyclic bending process for various non-ITO conductive materials and we found out that DMD layer shows superior fatigue resistant performance. This superior flexibility can be attributed to the highly ductile behavior of the metallic interlayer between the ITO layers.

We also extensively demonstrated the effect of the strain rate by controlling the bending speed. The electrical and mechanical properties changed dramatically depending on strain rates. At a high strain rate, there was not enough time to trigger thermal activation so the deformation developed only locally until fracture occurred, resulting in catastrophic failure.

Conversely, in a low strain rate, there was enough time to reach an equilibrium state, and this allowed thermally activated reactions to occur. The increased atomic mobility led to smooth and well distributed deformation, and this resulted in ductile fracture.

It is inevitable that the strain rate plays an important role in transforming the electrical and mechanical properties. Currently, there is no clear direction on fatigue evaluation, but these findings of strain effectiveness will trigger a new research topic. More studies on fatigue degradation will help us assess the fatigue failure more in depth and improve bending performances.

CHAPTER IV

Multiple Neutral Plane to Mitigate Bending Stress

Introduction

In mechanics, neutral plane or neutral surface is a conceptual plane within a beam or cantilever. When loaded by a bending force, the beam bends so that the inner surface is compressed and the outer surface is in tension. The neutral plane is the surface within the structure between these zones, where the material of the beam is not under any stress [51, 52]. To protect brittle electrode in flexible electronics, the mechanical neutral plane strategy can be adopted by placing the brittle thin film layers close to the neutral axis. This will minimize strain exerted on devices when the electrode is subjected to bending.

However, past researches on soft adhesives have been not only significantly limited in number but no sufficient findings and information were introduced [49, 50]. In this study, we investigated various low elastic modulus materials, characterized the mechanical property of each material, and finally utilized these compliant materials to create multiple neutral plane structures. After developing neutral plane structures, we tested the bending performance (cycle and static test) to protect the DMD layer by inserting each elastic modulus into a multilayer stackup. And lastly, we performed mechanical simulations, as well as analytical solutions, to present dependable guidelines for structural multilayer design when employing multiple neutral planes.

Recently, multiple neutral planes designs have been introduced as an effective tool to mitigate bending stress. By integrating extremely compliant materials, we can avoid the rapid failure of future flexible electronic devices. However, the strain distribution decoupled by the multiple neutral planes is not yet valid because it has not been verified clearly experimentally and analytically. Therefore, bending experiments should be the focus to find out the effectiveness of the multiple neutral planes approach.

It is important to understand the underlying principles of multiple neutral planes since highly contrasting materials are being subjected to bending. However, we cannot use the classical beam theory to analyze their behavior because the theory is based on the single neutral plane. Bending cross section of the beam must remain planar, but multilayer structure create shear deformation as seen in Figure 4.1.

We generated multiple neutral planes using various low elastic modulus layers and they were controlled through systematic analyses in order to improve the flexibility of DMD multilayer structure. This chapter will establish a concise and correct analytic model for the multilayer structure with dissimilar elastic properties and make it conclusive by FEA simulation and experimental results.

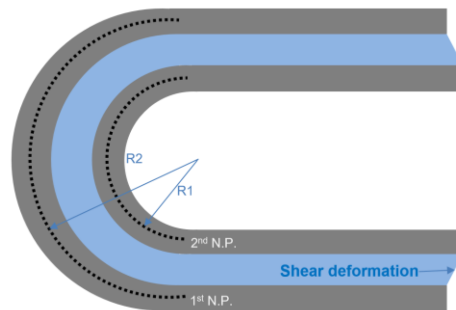

Figure 4.1. Schematic illustration of multiple neutral plane concepts. The middle layer is much softer than the other layers, both PET layers will bend independently. The soft adhesive largely deformed transferring the shear stress. Maximum bending strain of outer layer will be reduced with increased compliance of the structure compared to the structure with the hard adhesive. So if we increase the shear strain, it benefits the transfer of strain energy to the middle layer such that the strains in the outer layers diminish.

Sample Fabrication for Multiple Neutral Plane

Schematic diagrams of sample fabrication process are depicted in Figure 4.2.

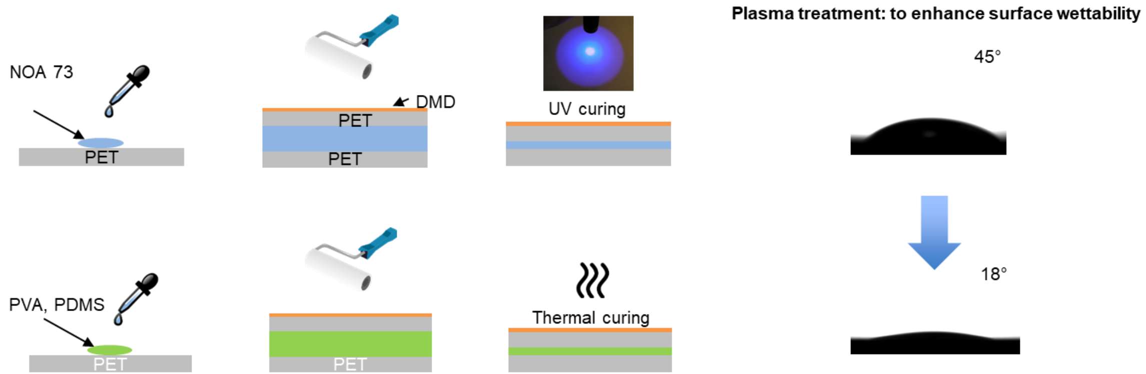

Figure. 4.2. Sample preparation process. In order to solidify each soft material, we used both UV and thermal curing process. In addition, for better adhesion, oxygen plasma treatment was applied to bare PET substrate. According to the contact angle measurement, surface wettability was enhanced and become hydrophilic surface after oxygen plasma treatment.

In order to achieve structural stability and flexibility of DMD stackup, it is necessary to increase the stretchability of the middle layer and the adhesion force between the layers must be strong. First of all, DMD was deposited on PET films (DMD/PET). Then, various soft adhesive solution was coated on top of PET layer to sandwich them in the order of DMD/compliant layer/PET, as shown in the figure above. Oxygen plasma treatment was performed afterwards to increase surface wettability.

The working pressure of the O_2 plasma was 200 mTorr with a constant oxygen gas flow of 40 sccm. After laminating each layer, both ends of the DMD film were painted with conductive silver paste to create electrical contact pads. As a part of elastic sample preparation, PVA was used with plasticizer. Polyvinyl alcohol (PVA, Sigma-Aldrich, Mw~ 98,000 g/mol) was dissolved in deionized water and was stirred vigorously for one hour to make an aqueous solution with a concentration of 10 wt%. Then ethylene glycol (Sigma Aldrich, ≥ 99%, Mw

~62.1 g/mol)), with a concentration of 10 vol%, was added to the PVA solution as a plasticizer. An additional hour of stirring was performed. The thin film of plasticized PVA was fabricated on glass substrate by a solution casting followed by drying at room temperature for 12 hours. Plasticizers are low molecular weight compounds, which, when blended with polymers, will increase the free volume of the material or the macro-molecular mobility of the polymer, and consequently the polymeric network becomes less dense due to the decrease in intermolecular forces. A number of plasticizers have been employed since this will improve and increase the flexibility and extensibility of flexible substrate. In order to compare the effects of plasticizers, we prepared pure PVA film without any plasticizers, and the result showed relatively higher elastic modulus. In other words, plasticizers work by embedding themselves between the chains of polymers, spacing them apart, increasing the free volume, and thus significantly lowering the glass transition temperature for the plastic and making it softer. Polydimethylsiloxane (PDMS) samples with different mixing ratios were prepared using a simple coating and curing process. A silicone elastomer PDMS (Sylgard 184, Dow Corning Co.) and its curing agent were mixed at 6:1, 10:1 and 30:1 weight ratio. The purpose of cross-linkers was to cure the PDMS, and a small amount of cross-linkers provided the low elastic modulus characteristics. The mixture was kept at 60°C for 4 hours. Depending on the mixing ratio, there were large differences in the elastic modulus.

To make a comparatively hard middle layer, various UV curable polymers were used. Specifically for this research, a solvent-free UV curable polymer (NOA73, Norland Products Inc., Cranbury, NJ) was selected as an example curable polymer. A calculated amount of UV curable resin was then poured onto the bare PET sample. UV curable polyurethane acrylate (PUA) resin was also used to compare elastic modulus of each material. After vacuum treatment,

excessive resin was scraped off using a clean razor blade. These UV curable resin were exposed under a mercury lamp for 300 s. To control the thickness of the middle layer, rubber covered roller was used for the post process. The sample was pressed, and the rotation of the roller pushed the sample forward. The number of rolling times fully depended on the modulus of each material. Overall, the thickness of each middle layer was approximately 25μm (± 1μm), and the total thickness of the stackup was 50μm (± 1μm).

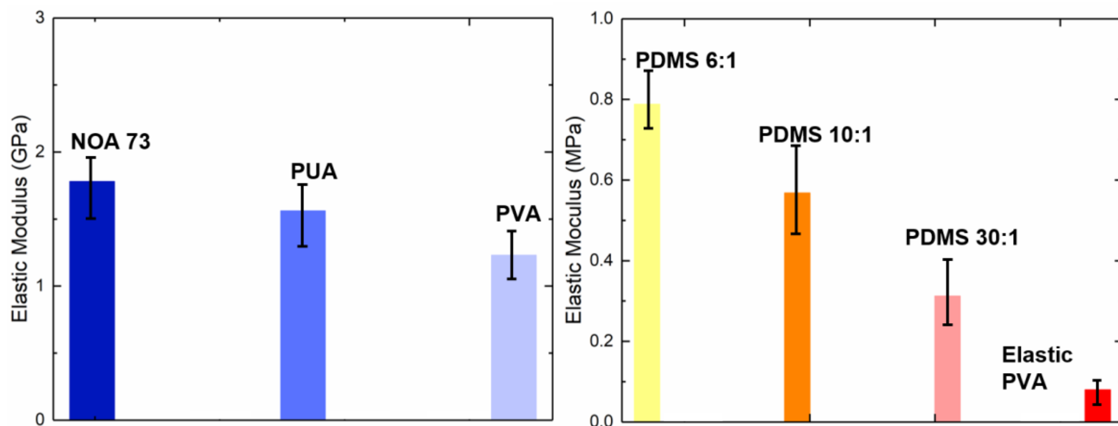

Figure. 4.3. It shows the elastic modulus of middle layer with different mechanical property. Various mixing ratios of the base polymer and curing agent was evaluated. There are two different types of middle layer on the table. (a) For hard middle layer: NOA73 (1.8 GPa), PUA (1.5 GPa), PVA (1.2 GPa), (b) For soft middle layer: PDMS 6:1 (0.8 MPa), PDMS 10:1 (0.6 MPa), PDMS 30:1 (0.4 MPa), and elastic PVA (0.1 MPa).

Bending Tests

DMD thin films on PET substrates were utilized to verify whether or not the multiple neutral planes actually exist and to check if they can endure severe bending stress and surpass the limitations. Static and cyclic bending tests were conducted to evaluate the electromechanical performance of multilayer structure through in situ electrical resistance measurement during bending. Electrical contact was made by the clamps and resistance was monitored with Keithley 196 multimeter to find the dynamic measurement of electrical resistance (two-point method) variance.

As depicted in Figure 4.4, electrical resistance of multiple samples were measured in situ during bending. In Figure 4.4 (a), DMD on 13μm PET sample showed superior flexibility compared to DMD on 50μm PET sample. This complies with the conventional beam theory, because the thinner stackup will achieve better flexibility. But interestingly, the multilayer stackup exhibited different $\Delta R/R_0$ value depending on the middle layer mechanical property. This can be seen in Figure 4.4 (b). Even though these multilayer structures are identical in thickness, they showed marked difference in bending performance. When the middle layer's elastic modulus was higher than bare PET film (E_{PET}=1.2 GPa), it deteriorated the bending performance. In our case, NOA73, PUA and normal PVA showed either higher or similar elastic modulus to that of bare PET.

As expected, better bending performance was observed with soft middle layer (PDMS and elastic PVA case). Due to the softer nature of the middle layer, both PET layers bent more independently. The compliant middle layer deformed largely, and as a result, bending stress transferred to the shear stress successfully. Maximum bending strain of the outer layer was decreased with increased compliance of the middle layer. So if we increase the shear strain, it

helps with the transfer of strain energy to the middle layer which will accordingly diminish strains in the outer layers. Among many soft middle layers, elastic PVA contained multilayer stackup and it exhibited excellent bending performance. When plasticizers are blended with polymers, it will increase the free volume of the material, and the polymeric network will sequentially become less dense due to the decrease in intermolecular forces. In result, stretchability is improved.

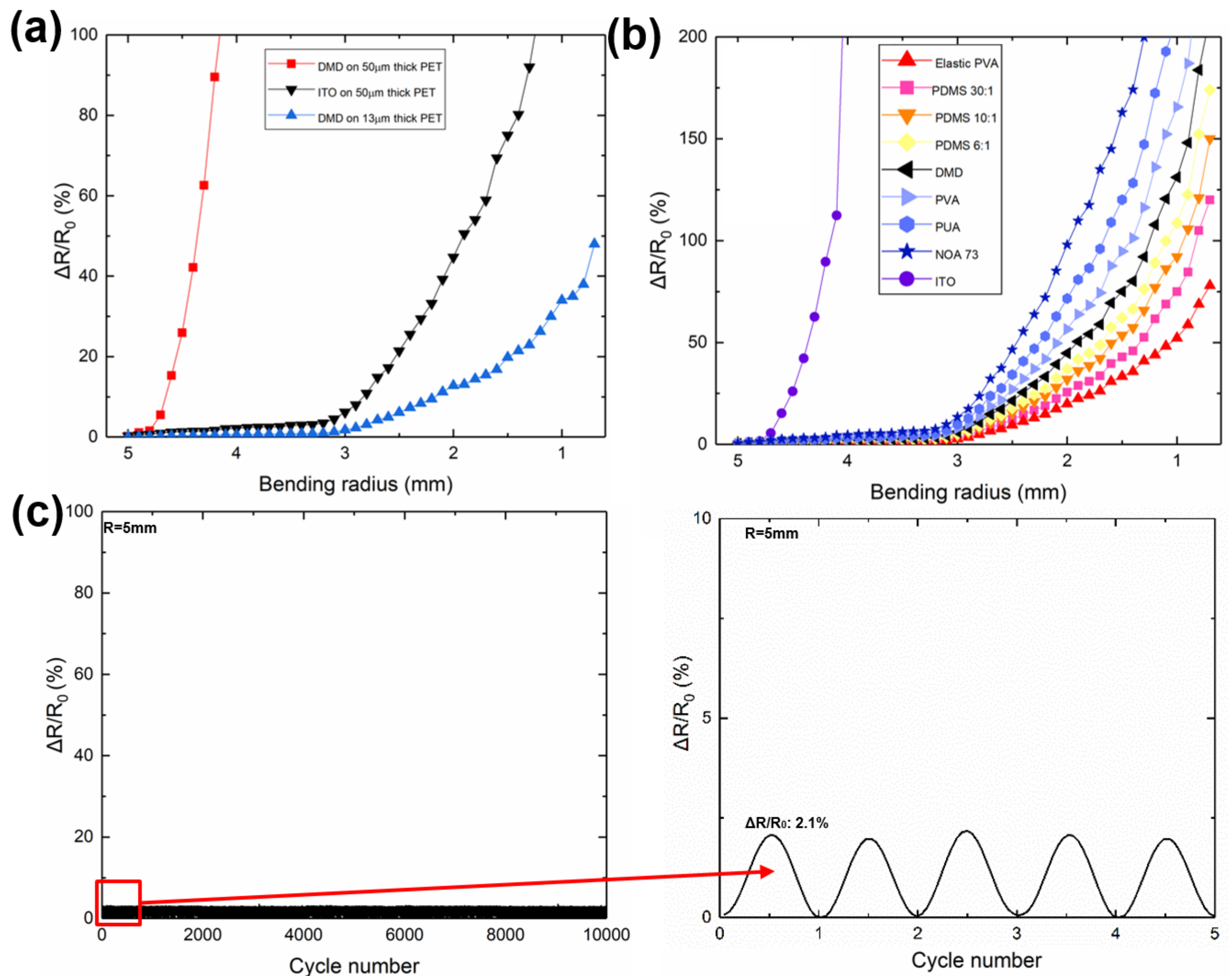

Figure. 4.4. Electrical resistance results of multiple samples during bending (a) Based on conventional beam theory, DMD on 13µm PET sample shows superior flexibility compared to DMD on 50µm PET sample. (b) Depending on the middle layer mechanical property, it exhibits different $\Delta R/R_0$ value. Even though these multilayer structures have identically same thick structures, they show significantly different electromechanical results. (c) Cyclic bending results of DMD multilayer combined with elastic PVA middle layer. The main curve showing perfectly repeatable sheet resistance oscillations, even after over ten thousand bending.

In addition, DMD multilayer combined with elastic PVA middle layer showed stable bending performance even after 10,000 cycles. This can be seen in Figure 4.4 (c). During bending and flattening, $\Delta R/R_0$ value was only 2.1%, which is considerably lower than that of the bare PET sample. This particular structure provides the direction in creating a multiple neutral plane that will endure severe bending stress.

FEA Simulations

The FEA simulations were conducted using ABAQUS. Our experimental method was similar to the FEA boundary conditions. The bending simulation was modeled using two steps: first, the boundary conditions were imposed at the plates in order to bend the specimen, and then the axial displacement boundary conditions were imposed at the plates in order to reduce the bending radius. The elastic modulus used in the FEA was extracted from experimental data. The sequence of each samples' elastic modulus, from rigid to soft, was: NOA73 (1.8 GPa), PUA (1.5 GPa), PVA (1.2 GPa), PDMS 6:1 (0.8 MPa), PDMS 10:1 (0.6 MPa), PDMS 30:1 (0.4 MPa), and elastic PVA (0.1 MPa).

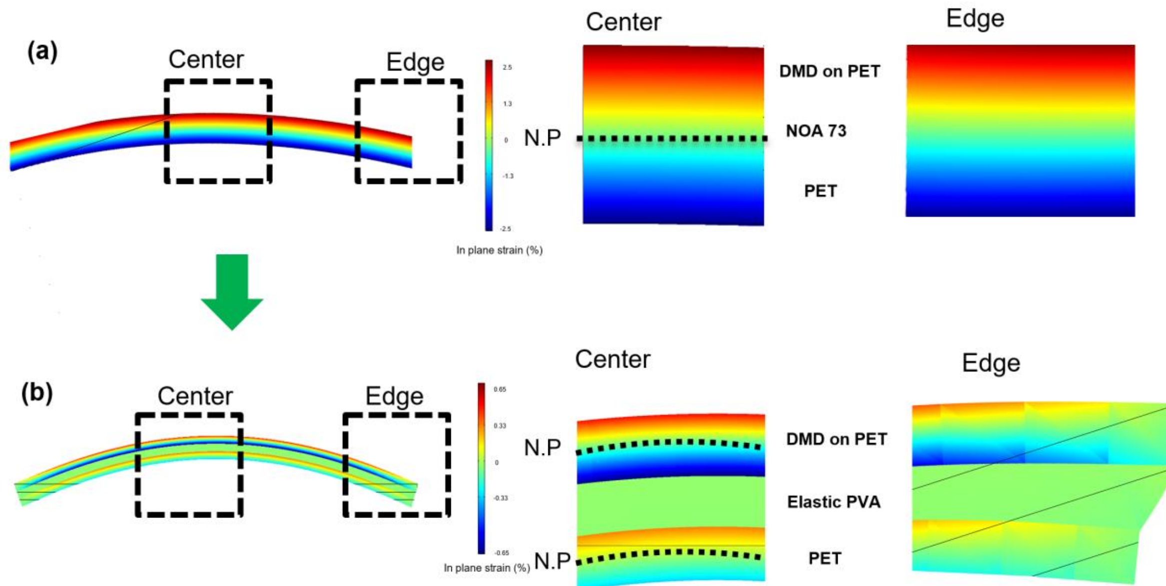

Figure 4.5. It presents the FEA results of bending two different multilayer structures with specific adhesive layers when multiple neutral planes appear in the structure. Even though these structures have identically same thick structures with PET 13µm/adhesive 24µm/ PET 13µm, it possesses significantly different strain level: one was a hard adhesive (E_{NOA73}=1.8GPa), (a) and the other was a soft adhesive ($E_{elastic\ PVA}$=0.1MPa), (b).

When the structure with the hard adhesive was subject to bending, the PET/adhesive/PET bent together with a single neutral plane as depicted in Figure 4.5 (a). The shearing stress of the adhesive layer is negligible, thus the plane section of the entire stack remained planar without any shear distortion or deformation. In this case, only single neutral plane was generated and the outer layer showed higher strain level compared to that of multiple neutral plane. If the material is comprised of homogenous properties, then the strain is proportional to the thickness.

In contrast, multiple neutral planes approach was applied by inserting a compliant middle layer in between the stiff PET layers, and the PET layers during bending are not coupled rigidly because the transverse sectional plane of the soft adhesive largely deformed the transfer of bending stress to shear stress. This can be seen in Figure 4.5 (b). Multiple neutral planes are more likely to tolerate severe bending conditions since their structure is more mechanically

flexible. Our analytical model in the following discussion will also support this finite element analysis.

Analytical Modelling Accounting for Multiple Neutral Axes in the Multilayer Stackup

In order to establish a concise but accurate analytical model for multilayered structures with completely different elastic properties, two important governing equations are introduced: (i) the force equilibrium between bending and shear stress, and (ii) continuity equation at each layer [50, 52].

As mentioned briefly before, the classical beam theory cannot be used to analyze the behavior or multiple neutral planes. The cross section of the layer must remain planar after bending in the laminated structure, but the soft layer undergoes shear deformation. The large modulus difference in each layer does not allow us to use this conventional theory and we have to create a new analytical model that will take into account the multiple neutral axes in a multilayer stackup.

The elastic modulus of the elastic PVA interlayer is three orders of magnitude smaller than that of the PET substrate. When this sandwiched multilayer structure is bent, the soft middle layer undergoes large shear deformation, which essentially decouples the deformation of the top and the bottom stiff layers. This response is similar to the strain decoupling effect discussed in the tension case. As a result, each stiff layer has its own neutral axis, and the multilayer stack thus creates multiple neutral axes. We validated this postulate using an analytical multi-neutral axis theory, and this is discussed below. Because of the soft PVA interlayer, the location of the neutral axis is shifted away from the center of the multilayer stack. To accurately predict the

strain distribution in each layer, we assumed that the cross-sectional planes in PET layers will remain planar during bending. Therefore, linear relation between strain and curvature is still valid (ε = t / R) for the top and the bottom PET layers:

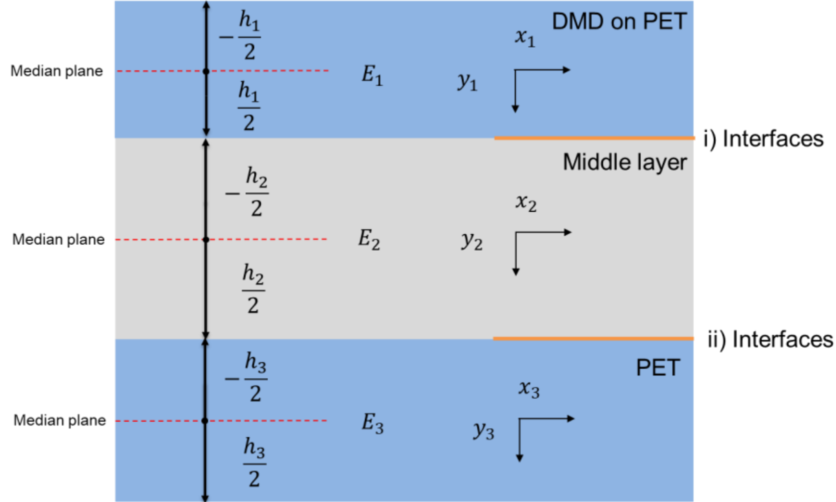

Figure 4.6. Notations used in the analytical modelling. Top and bottom layer has same elastic modulus and middle layer possesses very compliant layer in comparison to PET layer. The outer layer bending stress and middle layer shear stress should be equivalent. In addition, continuity equation at each layer interfaces is still valid.

Table 4.1. Notations used in the mechanical modelling for multiple neutral plane

Layer	Elastic Modulus	Thickness	Strain distribution	Distance from neutral plane to bending center
Top PET	E_1	h_1	ε_1	ρ_1
Middle layer	E_2	h_2	ε_2	n/a
Bottom PET	E_3	h_3	ε_3	ρ_3

As DMD layer thickness is only a few nanometer scale, the strain in DMD on PET can be written using the local coordinate systems:

$$\varepsilon_1(y_1) = \frac{y_1}{\rho_1}\left(-\frac{h_1}{2}<y_1<\frac{h_1}{2}\right) \quad (4.1)$$

Similarly, the strain in the bottom PET layer is:

$$\varepsilon_3(y_3) = \frac{y_3}{\rho_3} \left(-\frac{h_3}{2}<y_3<\frac{h_3}{2}\right) \quad (4.2)$$

Considering the continuity at each layer, we can assume that the strain in soft adhesive is a linear function of y_2:

$$\varepsilon_2(y_2) = ay_2 + b \left(-\frac{h_2}{2}<y_2<\frac{h_2}{2}\right) \quad (4.3)$$

a and *b* are the coefficients that will determine the continuity conditions at the top PET and middle layer interface, and the bottom PET and the middle layer interface. The continuity at layer interface introduces:

$$\varepsilon_2\left(-\frac{h_2}{2}\right) = \varepsilon_1\left(\frac{h_1}{2}\right), \varepsilon_2\left(\frac{h_2}{2}\right) = \varepsilon_3\left(-\frac{h_3}{2}\right) \quad (4.4)$$

Force equilibrium in x direction imposes:

$$E_1 \int_{-\frac{h_1}{2}}^{\frac{h_1}{2}} \frac{y_1}{\rho_1} dy_1 + E_3 \int_{-\frac{h_3}{2}}^{\frac{h_3}{2}} \frac{y_3}{\rho_3} dy_3 + E_2 \int_{-\frac{h_2}{2}}^{\frac{h_2}{2}} (ay_2 + b) dy_2 = 0 \quad (4.5)$$

This equation satisfies the following extreme case: when all layers are made up of the same materials, one single neutral plane will exist as we have predicted. Making a rough assumption that the top PET layer and the bottom PET layer have the same original length and bending angle, the bending radius from each layer's neutral axis to its bending center should also be the same:

$$\rho_1 = \rho_3 \quad (4.6)$$

In this equation, ρ represents the average radius of the multilayer and it yields:

$$2(E_1h_1 + E_3h_3) = E_2h_2(\left(\frac{h_1}{2}\right) - (\frac{h_3}{2})) \tag{4.7}$$

Once the neutral axis are determined, strain distribution across the stack thickness is given by:

$$\varepsilon = \begin{cases} \frac{y_1}{\rho}\ (-\frac{h_1}{2}<y_1<\frac{h_1}{2}) \\ \frac{\left(\frac{h_2}{2} - y_1\right)\left(\frac{h_1}{2}\right) - \left(\frac{h_2}{2} + y_1\right)\left(\frac{h_3}{2}\right)}{\rho}(-\frac{h_2}{2}<y_2<\frac{h_2}{2}) \\ \frac{y_3}{\rho}\ (-\frac{h_3}{2}<y_3<\frac{h_3}{2}\ ) \end{cases} \tag{4.8}$$

Taking into account the equations above, we can demonstrate strain distribution. In Figure 4.7, different colored lines were used to explain our analysis. The red line is the strain distribution which was derived by using the multiple neutral plane theory. The blue line is the strain distribution which was derived by using the conventional beam theory, so there is only one neutral plane (single orange color line). Double neutral planes was generated in case of the multiple neutral-axes theory (double orange color line). Multiple neutral planes was verified by using the continuity at layer interfaces and force equilibrium theory. If we insert compliant layer that can make enough shear deformation, the outer layer strain is accordingly decreased (From 2.5% to 0.65%). This value is similar to our FEA results. In conclusion, adding a soft middle layer formulate additional neutral plane and it minimizes the strains occurred at the outer layers during bending.

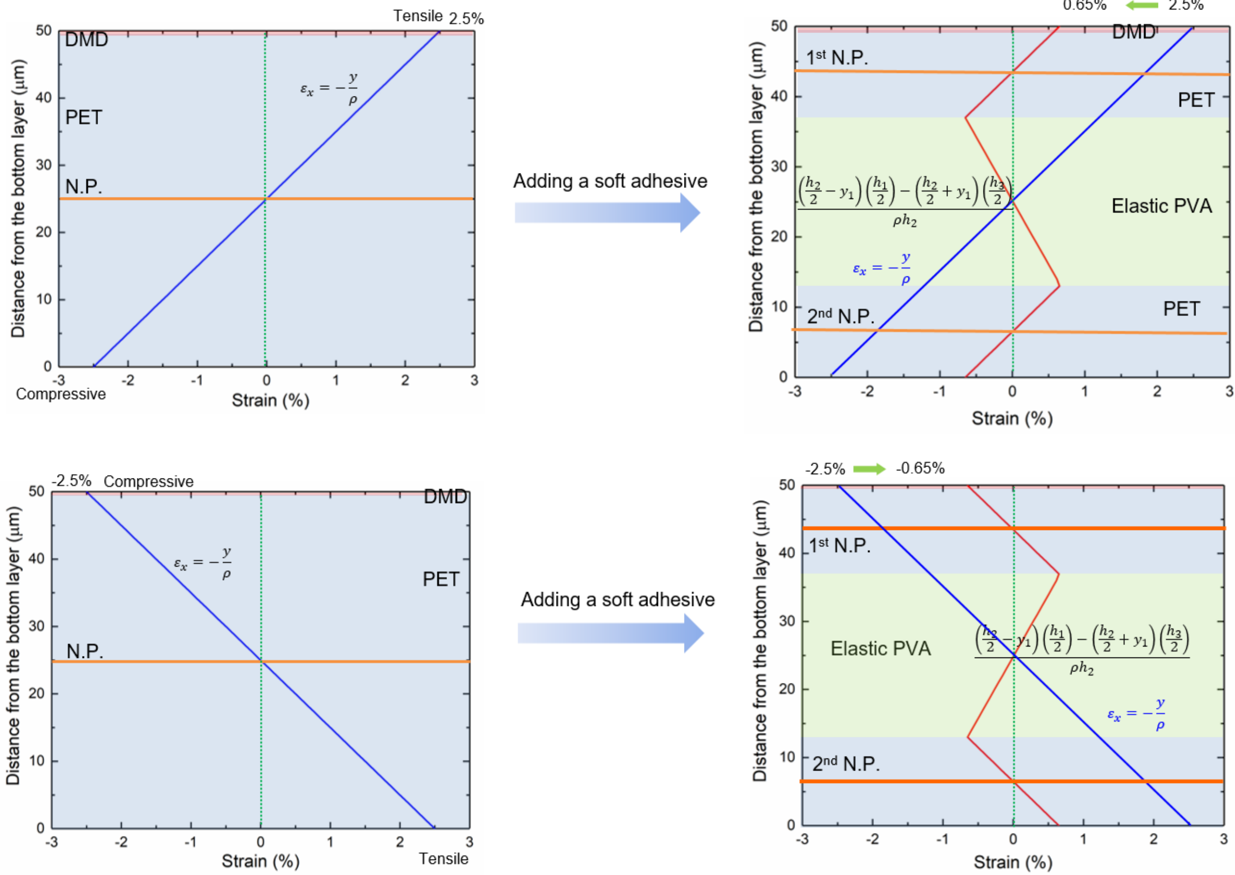

Figure 4.7. Through-stack strain distribution in the flexible conductor with a PET layer thickness of 50 µm bent to a radius of 1 mm. The blue line represents results calculated using the conventional theory, the red line is derived by using the multiple neutral-axes theory. Adding a soft adhesive create additional neutral plane, and minimizes their strains during bending. The neutral mechanical plane is split into multiple ones. (a) Figure demonstrates when DMD structure is subjected to tensile stress (Outward bending) and (b) is under compressive stress (Inward bending).

Conclusion

To exceed the limitations of the current DMD multilayered structure, the mechanical neutral plane strategy was adopted by inserting the compliant layer to minimize the strain applied on the electrode when it is bent. Even with identical thickness, different electro-mechanical performances resulted depending on the elastic behavior of the middle layer. When there was a similar elastic modulus material for the whole stack, it behaved like a homogenous material and bending-induced tensile strain was calculated analytically using the classical beam bending theory. However, with the addition of a compliant and stretchable middle layer, i.e. elastic PVA,

the maximum bending strain was significantly reduced with increased compliance of the middle layer. Ideally, the strain distribution on each layer will be fully separated if we decouple each layer completely. However, this is very difficult to achieve in multilayer stackup. Instead, we can focus on increasing the shear deformation to relieve the stress on the outer layers. Stretchable middle layer reduces the bending strain in PET layers and act as a defining tool to split the neutral mechanical plane and avoid premature failure of the device as a whole.

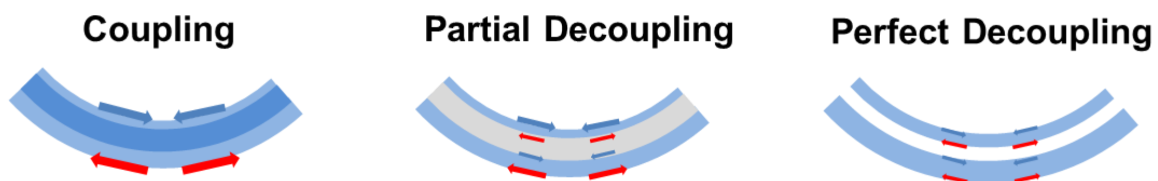

Figure 4.8. Maximize decoupling of each layer: Increase shear stress is key component to relieve outer layer bending stress.

CHAPTER V

Concluding Remarks and Suggestions for Future Work

Concluding Remarks

First and foremost, we analyzed the fracture behavior of thin film structures during bending process and proposed a theoretical framework to identify the underlying principles of robustness for DMD multilayered structures. In addition, we presented a very unique crack propagating phenomenon, which showed how the crack can deflect along with the metallic layer and create a step-like fracture. It was explained that this metallic layer was inserted in the middle of a multilayer structure to increase the fracture toughness in thin film materials. This ductile brittle combination strategy showed increased toughness because the thin metallic layer in between ITO layers can absorb the bending energy through shear deformation. Moreover, crack tip was blunted by plastic deformation in the vicinity, suggesting that the strain energy was spent in plastic deformation to prevent rapid crack propagation. We closely studied the crack deflection behavior of DMD layer and supported our argument with numerical and analytical assessments of our experiments.

Secondly, we investigated fatigue failure for various conductive materials. In cyclic bending deformations, DMD layer exhibits superior cycle performance, and the reason for subsequent degradation of electrical properties was explained. Through our experiments, we

learned that DMD is also superior in flexibility. It showed very low sheet resistance even after repeated cyclic operation. This flexibility can be attributed to the highly ductile behavior of the metallic interlayer. Furthermore, we investigated the effect of strain rate by controlling the bending speed. Strain rate suppressed mobility of atoms, resulting in difficulty changing its configurations, and in turn, yield strength became higher and brittle fracture occurred.

Lastly, to achieve even better flexibility of DMD samples, multiple neutral plane was created and it was employed by inserting stretchable layer to minimize the strain exerted on the electrode during bending. With the addition of a compliant and stretchable middle layer, i.e. elastic PVA, the maximum bending strain was significantly decreased with increased shear strain of the middle layer. We established a concise and accurate analytical model for this multilayer structure with dissimilar elastic properties and made it conclusive with FEA simulation and experimental results.

Suggestions for Future Work

Ductile brittle hybrid structure

Our studies successfully proved the advantages of metallic layer in DMD structures. For example, we showed how the addition of the metallic layer prevented crack propagation by plastic deformation and decreased bending stress with its shear deformation. From our findings, it is clear that metallic layer is effective, and more researches should be done to enhance the stability of future conductive electrodes. We suggest that more studies could focus on achieving better flexibility of the metallic layer. This could be done by testing different metallic materials like copper or alloy. In addition, we could continue to test its capability by designing a different

structure. Perhaps a thicker structure could be made by adding more layers, e.g. DMDMD. The increased thickness might be associated with an increase in shear strain. Finally, it might be helpful to investigate grain size effect by controlling the deposition rate of thin film since the grain size is the key parameter when determining the fatigue life.

Atomistic Simulation

We demonstrated how the strain rate affects the electrical and mechanical properties. At a high strain rate, there was not enough time for thermal activation to be effective and deformation developed only locally, resulting in a brittle-like fracture. The dislocations in metallic layer due to the local deformation across the sample led to non-uniform deformation of the electrode, and the dislocation density increased electrical resistance. We believe and propose that it is important to evaluate all of these properties more precisely and accurately in atomic scale through performing atomistic simulations in order to identify other underlying mechanisms that are affected by the changing strain rates.

REFERENCES

[1] Siya Huang, Yuan Liu, Chuan Fei Guo, Zhifeng Ren, "A Highly Stretchable and Fatigue-Free Transparent Electrode Based on an In-Plane Buckled Au Nanotrough Network, Advanced Electronic Materials (2017) 3, 1600534

[2] Cheng Peng, Zheng Jia, Henry Neilson, Teng Li, "In Situ Electro-Mechanical Experiments and Mechanics Modeling of Fracture in Indium Tin Oxide-Based Multilayer Electrodes" Advanced Engineering Materials (2013)15, No. 4

[3] Chang-Lae Kim, Chan-Won Jung, Young-Jei Oh and Dae-Eun Kim, "A highly flexible transparent conductive electrode based on nanomaterials" NPG Asia Materials (2017) 9, 00567

[4] J. Linnet, A. R. Walther, C. Wolff, O. Albreksten, N. A. Mortensen, J. Kjelstrup-Hansen. "Transparent and conductive electrodes by large-scale nano-structuring of noble metal thin-films," *Opt. Mater. Express* (2018) 1733-1746

[5] M Lagrange, T Sannicolo, D Muñoz-Rojas, B Guillo Lohan, A Khan "Understanding the mechanisms leading to failure in metallic nanowire-based transparent heaters, and solution for stability enhancement" Nanotechnology (2017) 28 055709

[6] Sung-Min Lee, Jeong Hyun Kwon, Seonil Kwon, and Kyung Cheol Choi,"A Review of Flexible OLEDs Toward Highly Durable Unusual Displays" IEEE TRANSACTIONS ON ELECTRON DEVICES, (2017) 67, 1733-1740

[7] Qian Dong, Yukihiro Hara, Kristina T. Vrouwenvelder, Kai T. Shin, Jared A. Compiano, Mohtashim Saif, Rene Lopez "Super flexibility of ITO Electrodes via Submicron Patterning" *ACS Appl. Mater. Interfaces* (2018) 10, 10339−10346

[8] Yuan Liu, Jianming Zhang, Heng Gao Yan Wang, Qingxian Liu, Siya Huang, Chuan Fei Guo, Zhifeng Ren "Capillary-Force-Induced Cold Welding in Silver-Nanowire-Based Flexible Transparent Electrodes" *Nano Lett.* (2017) 17, 1090−1096

[9] Ji-Hyun Lee, Doo-Young Youn, Ji Young Moon, Seon-Jin Choi, Chanhoon Kim, and Il-Doo Kim "Cu Micro belt Network Embedded in Colorless Polyimide Substrate: Flexible Heater Platform with High Optical Transparency and Superior Mechanical Stability" *ACS Appl. Mater. Interfaces* (2017) 9, 45, 39650-39656

[10] B. Bari, J.-H. Lee, T. Jang, P. Won, S. H. Ko, K. Alamgir, M. Arshad and L. J. Guo, "Simple hydrothermal synthesis of very-long and thin silver nanowires and their application in high quality transparent electrodes," *J. Mater. Chem. A*, (2016) 4, 11365-11371

[11] A. Khan, S. Lee, T. Jang, Z. Xiong, C. Zhang, T. Tang, L. J. Guo, and W.-D. Li “High Performance Flexible Transparent Electrode with an Embedded Metal Mesh Fabricated by Cost-effective Solution-process” Small (2016) 12(8), 3021–3030

[12] M. K. Kwak, J. G. Ok, J. Y. Lee, and L. J. Guo, "Continuous phase shift lithography by roll type mask and application to transparent conductor fabrication," *Nanotech.* (2012) 23, 344408

[13] M.-G. Kang, H. J. Park, S.-H. Ahn and L. J. Guo, "Transparent Cu nanowire mesh electrode on a flexible substrate fabricated by simple transfer printing and its application in organic solar cell," Solar Energy Materials & Solar Cells (2010) 94, 11791184,

[14] M. G. Kang, H. J. Park, S.-H. Ahn, T. Xu, and L. J. Guo, "Towards Low-Cost, High Efficiency, and Scalable Organic Solar Cells with Transparent Metal Electrode and Improved Domain Morphology," *IEEE J. Sel. Top. Quantum Electron.* (2010) 1094−1096

[15] Eun-Hye Ko, Hyo-Joong Kim, Sang-Jin Lee, Jae-Heung Lee and Han-Ki Kim “Nano-sized Ag inserted into ITO films prepared by continuous roll-to-roll sputtering for high performance, flexible, transparent film heaters” *RSC Adv.,* (2016) 6, 46634–46642

[16] Tae-Ho Kim, Sung-Hyun Park, Doo-Hee Kim, Yoon-Chae Nah, Han-Ki Kim “Roll-to-roll sputtered ITO/Ag/ITO multilayers for highly transparent and flexible electrochromic applications” Solar Energy Materials and Solar Cells, (2017) 160, 6634

[17] Jian-ChangLi, Bo Chen, Yu Qian, “Effect of fatigue fracture on the resistive switching of TiO2-CuO film/ITO flexible memory device” Current Applied Physics (2018)18, 1649

[18] Yang C W, Park J W. The cohesive crack and buckle delamination resistances of indium tin oxide (ITO) films on polymeric substrates with ductile metal interlayers. Surface and Coatings Technology, (2010), 204.

[19] H.K.Lina, S.M.Chiub, T.P.Chob, J.C.Huang “Improved bending fatigue behavior of flexible PET/ITO film with thin metallic glass interlayer” Materials Letters (2013) 113, 15

[20] Changhong Cao, Sankha Mukherjee, Jane Y. Howe, Doug D. Perovic, Yu Sun, Chandra Veer Singh and Tobin Fillete. "Nonlinear fracture toughness measurement and crack propagation resistance of functionalized graphene multilayers" Science Advances (2018) 4, 1826

[21] Takahiro Shimada, Kenji Ouchi, Yuu Chihara, Takayuki Kitamura. "Breakdown of Continuum Fracture Mechanics at the Nanoscale" Scientific Reports, (2015) 5, 8596

[22] Bongkyun Jang, Byungwoon Kim,, Jae-Hyun Kim, Hak-Joo Lee, Takashi Sumigawaa and Takayuki Kitamura “Asynchronous cracking with dissimilar paths in multilayer graphene” Nanoscale, (2017) 9, 17325–17333

[23] Nrup Balar and Brendan T. O’Connor “Correlating Crack Onset Strain and Cohesive Fracture Energy in Polymer Semiconductor Films” Macromolecules (2017) 50, 8611-8618

[24] R. T. Qu, Z. J. Zhang, P. Zhang, Z. Q. Liu & Z. F. Zhang “Generalized energy failure criterion” Scientific Reports, (2016) 6, 4951

[25] T.L. Anderson FRACTURE MECHANICS, CRC Press I, LLC (2017) 4th Edition, pages 368−380

[26] Mohammad A. Alkhadra, Samuel E. Root, Kristan M. Hilby, Daniel Rodriquez, Fumitaka Sugiyama, and Darren J. Lipomi "Quantifying the Fracture Behavior of Brittle and Ductile Thin Films of Semiconducting Polymers, *Chem. Mater.* (2017) *29*, 10139–10149

[27] Thomas Sannicolo, Nicolas Charvin, Lionel Flandin, Silas Kraus, Dorina T. Papanastasiou, "Electrical Mapping of Silver Nanowire Networks: A Versatile Tool for Imaging Network Homogeneity and Degradation Dynamics during Failure" ACS Nano (2018), 12, 4648−4659

[28] Chuan Fei Guoa, Qihan Liub, Guohui Wang, Yecheng Wang, Zhengzheng Shic, Zhifeng Rena "Fatigue-free, superstretchable, transparent, and biocompatible metal electrodes" *PNAS* (2015) 12332–12337

[29] Tse-Chang Li, Jen-Fin Lin "Fatigue life study of ITO/PET specimens in cyclic bending tests" *J Mater Sci: Mater Electron* (2015) 26, 250–261

[30] Giorgio Sernicola, Tommaso Giovannini, Punit Patel, James R. Kermode, Daniel S. Balint, T. Ben Britton & Finn Giuliani "In situ stable crack growth at the micron scale Reliability" Nature Communications (2017)108, 2751

[31] M. Mirkhalaf, A. Khayer Dastjerdi & F. Barthela "Overcoming the brittleness of glass through bio-inspiration and micro-architecture" Nature Communications, (2014) 5, 3166

[32] Seol-Min Yi, In-Suk Choi, Byoung-Joon Kim,Young-Chang Joo, "Reliability Issues and Solutions in Flexible Electronics Under Mechanical Fatigue" Electronic Materials Letters (2018) 14:387–404

[33] Byoung-Joon Kim, Thomas Haas, Andreas Friederich, Ji-Hoon Lee, Dae-Hyun Nam, Joachim R Binder, Werner Bauer, In-Suk Choi, Young-Chang Joo, Patric A Gruber and Oliver Kraft, "Improving mechanical fatigue resistance by optimizing the nanoporous structure of inkjet-printed Ag electrodes for flexible devices", Nanotechnology 25 (2014) 125706

[34] Donggyun Kim, Sung-Hoon Kim, Jong Hak Kim, Jae-Chul Lee, Jae-PyoungAhn, SangWoo Kim, "Failure criterion of silver nanowire electrodes on a polymer substrate for highly flexible devices" Scientific Reports (2017) 45903

[35] Florian Bouville, Eric Maire, Sylvain Meille, Bertrand Van de Moortèle, Adam J. Stevenson, Sylvain Deville "Hierachical structure inspired from nature Strong, tough and stiff bioinspired ceramics from brittle constituents" Nature Materials (2014) 13, 508–514

[36] V. IMBENI, J. J. KRUZIC, G. W. MARSHALL, S. J. MARSHALL, R. O. RITCHIE "The dentin–enamel junction and the fracture of human teeth" Nature Materials (2005), 4246

[37] Robert O. Ritchie "Armoured oyster shells" Nature Materials (2014) 13, 435–437

[38] Ming Yuan He, Anthony G. Evans, John W. Hutchinson "Crack deflection at an interface between dissimilar elastic materials: Role of residual stresses" International Journal of Solids and Structures, (1994) 31, 24

[39] Ming-Yuan He, John W. Hutchinson "Crack deflection at an interface between dissimilar elastic materials" International Journal of Solids and Structures, (1989) 25, 9

[40] Yan Li, Min Zhou "Prediction of fracture toughness of ceramic composites as function of microstructure: II. analytical model" Journal of the Mechanics and Physics of Solids 61 (2013) 489–503

[41] Yue Fan, Yuri N. Osetskiy, Sidney Yip, and Bilge Yildiz "Mapping strain rate dependence of dislocation-defect interactions by atomistic simulations" *PNAS* (2013) 110 (44)

[42] Zhitong Bai and Yue Fan "Abnormal Strain Rate Sensitivity Driven by a Unit Dislocation-Obstacle Interaction in bcc Fe" *Phys. Rev. Lett*. (2018) 120, 125504

[43] Yue Fan, Yuri N. Osetsky, Sidney Yip, and Bilge Yildiz "Onset Mechanism of Strain-Rate-Induced Flow Stress Upturn" *Phys. Rev. Lett*. (2012) 109, 135503

[44] H. Eyring, "Viscosity, plasticity, and diffusion as examples of absolute reaction rates," The Journal of Chemical Physics (1936) 4. 283–291

[45] T. Ree and H. Eyring, "The relaxation theory of transport phenomena," in Rheology: Theory and Applications, F. R. Eirich, Ed., (1958) vol. 2, chapter 3, Academic Press, New York, NY, USA,

[46] J. Richeton, S. Ahzi, K. S. Vecchio, F. C. Jiang, and R. R. Adharapurapu, "Influence of temperature and strain rate on the mechanical behavior of three amorphous polymers: characterization and modeling of the compressive yield stress," International Journal of Solids and Structures (2006) 43, 2318–2335

[47] Z. El-Qoubaa and R. Othman, "Tensile behavior of polyetheretherketone over a wide range of strain rates," International Journal of Polymer Science (2015) 275937, 9.

[48] W. Moćko, J. A. Rodríguez-Martínez, Z. L. Kowalewski, and A. Rusinek, "Compressive viscoplastic response of 6082-T6 and 7075-T6 aluminium alloys under wide range of strain rate at room temperature: experiments and modelling," Strain (2012) 498–509

[49] Lan Li, Hongtao Lin1, Shutao Qiao, Yi Zou, Sylvain Danto3, Kathleen Richardson, J. David Musgraves, Nanshu Lu, Juejun Hu "Integrated flexible chalcogenide glass photonic devices" Nature Photonics (2014) 8, 12

[50] Yan Shi, Yonggang Huang "Multiple Neutral Axes in Bending of a Multiple-Layer Beam With Extremely Different Elastic Properties" Journal of Applied Mechanics (2014) 114501-1

[51] Yewang Su, Shuang Li, Rui Li, Canan Dagdeviren "Splitting of neutral mechanical plane of conformal, multilayer piezoelectric mechanical energy harvester" *Appl. Phys. Lett.* (2015) 107, 041905

[52] Wansun Kim, Inhwa Lee, Dong Yoon Kim,Youn-Yeol Yu, Hae-Yoon Jung, Taek-Soo Kim "Controlled multiple neutral planes by low elastic modulus adhesive for flexible organic photovoltaics" Nanotechnology (2017) 28, 194002

[53] Window A.L. Strain Gauge Technology. Elsevier Applied Science; London, UK: (1992)

[54] Shixuan Yang, Nanshu Lu "Gauge Factor and Stretchability of Silicon-on-Polymer Strain Gauges" Sensors (2013) 13(7), 8577–8594

[55] Michela Borghetti, Mauro Serpelloni, Emilio Sardini, Stefano Pandini "Mechanical behavior of strain sensors based on PEDOT:PSS and silver nanoparticles inks deposited on polymer substrate by inkjet printing" Sensors and Actuators A (2016) 243, 71–80

[56] J. C. Fan and F. J. Bachner, “Transparent heat mirrors for solar-energy applications,” *Appl. Opt.* (1976) 15(4), 1012–1017

[57] G. Leftheriotis, P. Yianoulis, and D. Patrikios, “Deposition and optical properties of optimized ZnS/Ag/ZnS thin films for energy saving applications,” Thin Solid Films (1997) 306, 92–99

[58] Westergaard, H.M., "Bearing Pressures and Cracks," Journal of Applied Mechanics, (1939) Vol. 6, pp. A49-53

[59] Inglis, C.E., "Stresses in Plates Due to the Presence of Cracks and Sharp Corners," Transactions of the Institute of Naval Architects, (1913) Vol. 55, pp. 219-241

[60] Rice, 1. R. “Elastic fracture mechanics concepts for interfacial cracks” *J. Appl. Mech*. (1988) 55 (1),98-103.

[61] Zak, A. R. and William, M. L. “Crack point singularities at a bimaterial interface”. *J. Appl. Mech.* (1963) 30 (I), 142-1436

[62] C.T. Sun, Z.-H. Jin “Fracture Mechanics: Chapter 3 - The Elastic Stress Field around a Crack Tip” (2012) Academic Press. Page 25-36, https://doi.org/10.1016/C2009-0-63512-1

[63] G.R. Irwin, “Fracture dynamics,” Trans. Am. Soc. Met. 40A, (1948) pp. 147–166.

[64] G.R. Irwin, “Analysis of stresses and strains near the end of a crack traversing in a plate,” *J. Appl. Mech.* 24, (1957) pp. 361–364.

[65] M.L. Williams, J. Appl. Mech. 24, 109 (1957)